Universidad del País Vasco
Euskal Herriko Unibertsitatea

Elektrizitatea eta Elektronika Saila
Departamento de Electricidad y Electrónica

Stability analysis of RF power amplifiers through MIMO pole-zero identification techniques

by

Libe Mori Carrascal

Supervised by Aitziber Anakabe Iturriaga & Juan Mari Collantes Metola

Dissertation submitted to the Department of Electricity and Electronics of the University of the Basque Country (UPV/EHU) as partial fulfilment of the requirements for the PhD degree in Engineering Physics

Nire familiari

Acknowledgments

First and foremost, I would like to express my gratitude to all the people who in one way or another have contributed to this work.

This dissertation would not have been possible without the guidance and support of my advisors Juan Mari Collantes and Aitziber Anakabe. I much appreciate all the time and effort you have put into this thesis and, most importantly, into me. But, rest assured, this will not be the last time you hear from me!

I also take this opportunity to express my gratitude to the Radio Frequency and Microwave Investigation Research Group of the University of the Basque Country, for making me feel at home. Special thanks to Nerea Otegi and Joaquin Portilla for their support and readiness to help me.

I am also much obliged to Ibone Lizarraga for her valuable contributions and for helping me understand the discussed concepts on control automatics and the mathematics behind them.

I also thank Joana Pelaz for helping me dip my toe into the experimental world of microwave electronics. And I must not forget to thank my fellow lab-mates Javi, Asier and Popi for their contributions, but most importantly for having endured all those long hours in the laboratory with me. Lankide on eta lagun alai bat alboan izateak asko lagundu dit hiru urte hauetan zehar, mila esker Popi!

Je remercie aussi vivement tout le service DSO/RF/HNO du Centre National d'Études Spatiales (CNES) pour m'avoir accuelli. Les 5 mois de mon séjour à Toulouse sont très bien passés et je suis contente d'avoir eu la chance de vous connaitre et de travailler avec vous. Spécialement, je tiens à remercier Vincent Armengaud et Geoffroy Soubercaze-Pun, avec son aide j'ai appris les bases de la conception des amplificateurs MMIC et j'ai pu concevoir un amplificateur Doherty. Je suis sûre que toute la connaissance et les compétences que j'ai acquises au CNES m'aideront dans le futur.

In addition, acknowledgments to all the other doctorate students, researchers and professors of the Electricity and Electronic Department for enlivening my lunch, fruit, coffee... breaks and for listening to me constantly moan over window-less laboratories.

I also would like to thank my closest friends for all those endless talks and laughs over coffee and *braviolis*, discussing everything and nothing, that helped me disconnect and recharge the batteries to carry on working. *Lana ez baita hain gogorra irribarreak baditugu ahoan!*

Last but not least, I would like to thank my family, the origin of many happy memories and my constant source of inspiration. Ama eta Aita, milesker une gogorretan laguntza eta lasaitasuna sentiarazteagatik, une alaietan beti ospatzeko prest egoteagatik eta finean niregatik egin duzuen guztiagatik. Usue, Jon eta Iraia, familiako txikiaren lekukoa gustu handiz pasatu diot Iraiari, abentura berria hasi da, disfruta dezagun beraz bidaiaz!

Mila Esker Danoi!

"I was just excited to have challenging work to do and smart people to work with."

Katherine Johnsons

Introduction

The appearance of undesired spurious oscillations in high-frequency power amplifiers is a common issue faced by microwave designers. A power amplifier designed without carrying out rigorous stability analyses might be unstable and could generate spurious oscillations that hinder its correct functioning and could even lead to its destruction.

The correct detection of instabilities is even more critical in Monolithic Microwave Integrated Circuit (MMIC) amplifiers since, due to the integrated nature of this technology, no latter modifications can be applied to the design. Therefore, precise stability analysis methods and tools are essential to avoid never-ending and costly design cycles.

Spurious oscillations often show-up in high-frequency multistage power amplifiers since they contain multiple active devices and many feedback loops that can easily satisfy the oscillation conditions at a given spurious frequency. Thus, the detection of instabilities and the exact location of the unstable feedback loops through simulation is essential to provide appropriate solutions for eliminating them with minimum impact over the performance of the circuit.

Most standard algorithms for designing and simulating microwave active circuits in Computer Aided Design (CAD) tools are unable to predict instabilities. These algorithms, that mainly work in the frequency domain or the tempo-frequency domain, calculate the steady state solutions of the circuit without solving the transient state of the circuit. Thus, they may converge to non-physically observable mathematical solutions that do not include the oscillatory behavior.

Consequently, a variety of specific stability analysis methods for microwave circuits have been developed that combined with conventional CAD simulation tools can predict instabilities. One of the most powerful and popular techniques is based on frequency domain linear pole-zero identification. The commercial tool that makes use of this technique, the STAN tool, is a pole-zero stability analysis technique for linear and non-linear microwave active circuits based on obtaining a closed-loop Single-Input Single-Output (SISO) transfer function of the circuit linearized about a given DC or periodic large-signal steady state.

SISO pole-zero identification has widely demonstrated its value in the detection of undesired spurious oscillations in power amplifiers. However this technique still suffers from two main drawbacks. On the one hand, SISO identification is linked to losses of controllability and observability, since not all resonances are always detected clearly on all of the nodes or branches of the circuit. On the other hand, a problem general to any identification process is that the order of the transfer function to be fitted is *a priori* unknown. If the selected order is too small, the detection of an instability could be missed. But if the selected order is excessively high, mathematical pole-zero quasi-compensations resulting from overmodeling might appear and this could lead to erroneous conclusions regarding stability.

One of the main goals of this thesis is to overcome the previously mentioned limitations of the SISO pole-zero identification technique. A Multiple-Input Multiple-Output (MIMO) pole-zero identification methodology is proposed as the solution to minimize the mentioned drawbacks of the SISO pole-zero identification technique. Thanks to the generation of a MIMO stability analysis methodology and tool, a new strategy to ensure stability of multistage power amplifiers has been designed and a new systematic approach for the stabilization of large-signal instabilities has been formulated.

This thesis is structured as follows.

The state of art in stability analysis techniques for microwave circuits is reviewed in the first chapter. That is, the concept of stability in microwave circuits and the existing methodologies and commercial CAD tools for stability analysis are discussed at length. Special emphasis is placed in describing the pole-zero stability analysis methodology and in the pole control and placement technique for stabilization of small-signal oscillations.

The second chapter describes in detail the MIMO stability analysis methodology and tool that has been designed within the framework of this thesis. In addition, other benefits of MIMO pole-zero identification are described, such as the possibility to detect the location of the inner loops that create spurious oscillations in complex multistage amplifiers. This can provide invaluable information on where and how to act in the circuit in order to eliminate unstable behavior with minimum impact on its performance. Additional strategies to detect overmodeling have also been created and are illustrated in this chapter.

In the third chapter, the design process and extensive stability analysis of a X-band MMIC Doherty amplifier is detailed. Additionally, the potential of the MIMO stability analysis technique described in the second chapter is demonstrated in this chapter. Thanks to the mentioned tool, two small-signal instabilities are detected and stabilized, and the origin of a pair of very resonant stable poles at the fundamental frequency is determined.

The fourth chapter extends, to the large-signal regime, the systematic stabilization approach for small-signal instabilities introduced in the first chapter. That is, by respecting the MIMO nature of Periodic Linear Time Variant (PLTV) systems and applying basic control theory, the series or shunt stabilization networks to stabilize large-signal instabilities can be determined with the new technique described in this chapter.

Eventually, the final conclusions and future work are summarized.

Contents

1 Stability in Microwave and RF Circuits

1.1 Introduction

The appearance of instabilities on power amplifiers is a common issue faced by microwave and RF designers. These circuits often contain multiple active devices and many feedback loops that can easily reach the oscillation conditions when a parameter of the circuit is varied, such as, bias, loading conditions, temperature or the RF input power [1]–[5].

Detecting these instabilities during the design phase is essential to reduce the design cycles and costs of high frequency amplifiers, specially in Monolithic Microwave Integrated Circuits (MMIC) since subsequent adjustments are impossible [6]–[9].

Unfortunately, the circuit analysis strategies and tools designed for low-frequency applications are not valid for high-frequency circuits. The presence of Scattering parameter blocks (described in the frequency domain), the difficulty of modeling the distributed components in the time domain and the excessively long transients compared to the periods of the high frequency signals make for very time-consuming time-domain analyses of microwave and RF circuits.

Consequently, frequency domain or tempo-frequency domain analyses are usually carried out to analyze high-frequency circuits [10]–[12].

However, frequency domain or tempo-frequency domain algorithms, such as the harmonic balance algorithm [13], [14], do not simulate the transitory solutions. Hence, the stability of the calculated steady state solutions is not guaranteed. That is, many mathematical solutions exists, but only some of those solutions are physically observable. Therefore, stability analysis methods and Computer Aided Design (CAD) tools to analyze the stability of the obtained solutions are indispensable for designing stable high-frequency circuits.

This chapter revises some of the existing frequency domain stability analysis methods and CAD tools, which are essential for designing stable microwave and RF circuits.

1.2 Main Methods for Stability Analysis of Microwave Circuits

A nonlinear system can be represented as a system of differential nonlinear equations [4]:

$$\dot{\overline{x}} = f(\overline{x}) \tag{1.1}$$

where $\overline{x} = [x_1, ..., x_n]^T$ represents the state vector and f is a continuous and infinitely derivable function.

Unlike linear systems, nonlinear systems do not have a sole possible solution. Many possible solutions coexist for nonlinear systems, such as, the equilibrium point solutions, the periodic solutions, the quasi-periodic solutions and the chaotic solutions.

In order to determine the local stability of any of the mentioned solutions of the nonlinear system in (1.1), one can analyze the effects that small perturbations, such as vibrations and noise, have on the solutions of the system. That is, one can analyze whether if a small

perturbation moves the system away from the (unstable) solution or if the perturbed system returns exponentially in time back to the initial (stable) solution.

Nonetheless, a locally stable solution of a nonlinear system does not imply global stability, since a large perturbation can force the system to abandon a locally stable solution and reallocate on another locally stable solution that is nearby.

Throughout this section, the most commonly used, rigorous and even commercially implemented methods for DC and large-signal stability analyses are briefly described.

1.2.1 Stability Analysis of a DC Solution

An equilibrium point is defined as a fixed point solution that cancels the f function in (1.1). For example, the DC solutions ($\overline{x}_{DC}$) of an electronic circuit with no external input signal are known as the equilibrium solutions of (1.1).

$$f(\overline{x}_{DC}) = 0 \tag{1.2}$$

In order to analyze the variations on a system caused by small perturbations, we define $\overline{\xi}(t)$, a small perturbation around the DC solution. Taking the small perturbation into account, the resulting $\overline{x}$ state vector is defined as follows:

$$\overline{x} = \overline{x}_{DC} + \overline{\xi}(t) \tag{1.3}$$

Introducing the state vector (1.3) to the nonlinear equation in (1.1), the equation in (1.4) is obtained.

$$\dot{\overline{x}}_{DC} + \dot{\overline{\xi}}(t) = f(\overline{x}_{DC} + \overline{\xi}(t)) \tag{1.4}$$

Since the introduced perturbation $\overline{\xi}(t)$ is small, the $f(\overline{x}_{DC} + \overline{\xi}(t))$ term in (1.4) can be substituted by the two significant terms of its Taylor expansion. This substitution simplifies the state-space representation in (1.4) as follows:

$$\dot{\overline{x}}_{DC} + \dot{\overline{\xi}}(t) = f(\overline{x}_{DC}) + Jf(\overline{x}_{DC})\overline{\xi}(t) \tag{1.5}$$

where $Jf(\overline{x}_{DC})$ is the Jacobian matrix of the system evaluated at the DC solution $\overline{x}_{DC}$:

$$Jf(\overline{x}_{DC}) = \left.\frac{\partial f(\overline{x})}{\partial \overline{x}}\right|_{\overline{x}_{DC}} = \begin{bmatrix} \left.\frac{\partial f_1}{\partial x_1}\right|_{\overline{x}_{DC}} & \cdots & \left.\frac{\partial f_1}{\partial x_n}\right|_{\overline{x}_{DC}} \\ \vdots & \ddots & \vdots \\ \left.\frac{\partial f_n}{\partial x_1}\right|_{\overline{x}_{DC}} & \cdots & \left.\frac{\partial f_n}{\partial x_n}\right|_{\overline{x}_{DC}} \end{bmatrix} \tag{1.6}$$

Given that $\overline{x}_{DC}$ is a possible solution of many co-existing system solutions (1.2), the perturbed system can be approximated by the linear system in (1.7).

$$\dot{\overline{\xi}}(t) = \mathbb{G}(t)\ \overline{\xi}(t) \tag{1.7}$$

where $\mathbb{G}(t)$ is the $Jf(\overline{x}_{DC})$ Jacobian matrix of the system evaluated at the DC solution $\overline{x}_{DC}$.

In other words, the qualitative properties of the nonlinear system in (1.4) around a given equilibrium solution can be approximated through a linearization of the system around the equilibrium solution, granted that said linearization does not include eigenvalues on the $j\omega$ axis [15].

Consequently, by analyzing the eigenvalues of the $Jf(\overline{x}_{DC})$ Jacobian matrix or the roots of the characteristic equation (1.8), one can determine the stability of a DC solution.

$$det[\lambda I - Jf(\overline{x}_{DC})] = 0 \tag{1.8}$$

That is, the DC solution $\overline{x}_{DC}$ will be locally stable if the $\overline{\xi}(t)$ perturbation tends to zero as t increases, or correspondingly, if the eigenvalues of the Jacobian matrix all have negative real parts.

Many methods to determine the stability a DC solution can be found in the literature [16]–[30]. In this subsection the most common methodologies are summarized.

The Rollet Stability Factor

In 1962 J. M. Rollet introduced a criteria for determining the unconditional stability of a two-port network based on its $[Z]$, $[Y]$, $[G]$ or $[H]$ parameters [16].

J. M. Rollet stated that a two-port network is unconditionally stable if no combination of passive input and output impedances leads to spurious oscillations, granted that the Rollet condition is met. The mentioned condition, also known as the Rollet proviso [17],[18], states that the poles of the two-port network for ideal terminations (open circuit and short circuit) must remain on the left-hand side of the complex plane.

Since small-signal RF and microwave amplifiers are often described by the Scattering parameters [31], the representation of the unconditional stability criteria introduced by J. M. Rollet was soon modified to include the Scattering parameters [19].

As discussed in [19], many incomplete or unnecessarily complex criteria were proposed and discussed until an equivalent criteria to [16] represented in Scattering parameters was found: provided that the Rollet proviso is met *a priori*, a two-port network is unconditionally stable if the condition in (1.9) is met for all the frequencies at which the amplifier has gain,

$$K = \frac{1 - |S_{11}|^2 - |S_{22}|^2 + |\Delta|^2}{2\,|S_{12}S_{21}|} > 1 \tag{1.9}$$

and one of the following six auxiliary conditions is also fulfilled.

$$\begin{aligned} |\Delta| &= |S_{11}S_{22} - S_{12}S_{21}| < 1 \\ B_1 &= 1 + |S_{11}|^2 - |S_{22}|^2 - |\Delta|^2 > 0 \\ B_2 &= 1 - |S_{11}|^2 + |S_{22}|^2 - |\Delta|^2 > 0 \\ 1 &- |S_{11}|^2 > |S_{12}S_{21}| \\ 1 &- |S_{22}|^2 > |S_{12}S_{21}| \end{aligned} \tag{1.10}$$

Checking the conditions in (1.9) and (1.10) is equivalent to evaluating whether the negative resistance condition is met, or to checking the magnitude of a single stability parameter (1.11) for all the frequencies at which the amplifier has gain [23].

$$\mu = \frac{1 - |S_{11}|^2}{|S_{22} - S_{11}^*\Delta| + |S_{21}S_{12}|} > 1 \tag{1.11}$$

If the conditions in (1.9) and (1.10) or (1.11) are not met for all the frequencies under analysis, the input and output stability circles can be plotted to determine the values of the input and output loading conditions that might potentially lead to instabilities.

Despite the effectiveness of this method for determining the input and output loads that may potentially destabilize the system, its main limitation is the Rollet proviso [17], [18]. Before checking the stability factors in (1.9) and (1.10) or (1.11), one must first guarantee that the

uncharged system has no inner unstable loops, which is quite common in multistage amplifiers. In [20] multiple examples are shown where the Rollet stability analysis carried out without previously checking the Rollet proviso leads to incorrect conclusions. Therefore, additional stability analysis tools are required to check the Rollet proviso.

The Normalized Determinant Function Technique

Platzker et al. [20], [21] established the difficulty of checking the Rollet Proviso and, as a solution, introduced the *Normalized Determinant Function* (NDF) technique that serves to assure the stability of a network prior to applying the Rollet criteria.

This technique consists of analyzing the diagram on the complex plane of the *Normalized Determinant Function*, in order to check whether the full network determinant contains zeros on the right-hand side of the s plane.

Unfortunately, applying the NDF technique can be very time consuming for complex circuits and it requires access to many intrinsic nodes of the models of the transistors, which are not always available. Whilst simplified NDF methods do exist, they do not guarantee the detection of all the possible oscillations.

The *Stability Envelope Method* introduced in [22] consists of visualizing the NDF function for all possible passive terminations. If the stability envelope encloses the origin, the circuit is not unconditionally stable. That is, there might be zeros of the determinant of the system on the right-hand side of the s plane for a given source or load value.

The Small-Signal Oscillation Test

Instead of analyzing the unconditional stability of a two-port network, often its stability for a set of source and load conditions is analyzed.

The *small-signal oscillation test* consists of analyzing the stability of a given charged network by analyzing it as an oscillator and verifying if the start-up condition of the oscillation is met [26]–[28].

In [29] Ohtomo generalized the *small-signal oscillation test* to rigorously analyze the stability of DC solutions of multistage circuits. Despite its effectiveness to detect odd and even mode instabilities, the practical application of the methodology can be quite tedious for circuits with many active components.

It should also be noted that the technique proposed in [29] assumes that the active sub-circuit is inherently stable, which might not always be a valid assumption.

However, new techniques to check the inherent-stability proviso on field-effect transistors have been recently proposed in [30], [32]. These techniques are based on applying the Nyquist criterion to a network determinant curve to graphically check whether a simple inequality condition is met. However, in order to apply these techniques, the intrinsic portion of the active devices must be accessible and they should be similar (or equivalent) to a proposed topology that is said to be shared by all active devices.

Stability Analysis from Transfer Function Analysis

All information regarding the stability of a nonlinear system around its DC solution can also be determined from any of the closed-loop transfer functions that represents the system under analysis.

In order to obtain a closed-loop transfer function of the system a small input signal $\overline{u}(t)$ is introduced to the linearized system in (1.7), and the output signal $\overline{y}(t)$ is defined as a linear combination of the state vector as follows:

$$\begin{aligned} \dot{\overline{\xi}}(t) &= \mathbb{G}\overline{\xi}(t) + \mathbb{B}\overline{u}(t) \\ \overline{y}(t) &= \mathbb{C}\overline{\xi}(t) + \mathbb{D}\overline{u}(t) \end{aligned} \tag{1.12}$$

The resulting $H(s)$ transfer function is defined as the function that

relates the input signal $\overline{u}(t)$ and the output signal $\overline{y}(t)$ in the frequency domain (1.13).

$$\overline{Y}(s) = H(s)\overline{U}(s) \tag{1.13}$$

The $H(s)$ transfer function in (1.13) can be expressed as a ratio of two polynomials $N(s)$ and $D(s)$ as follows:

$$H(s) = \frac{N(s)}{D(s)} = \frac{(s - z_1)(s - z_2)...(s - z_N)}{(s - p_1)(s - p_2)...(s - p_N)} \tag{1.14}$$

where the z_i elements (or the roots of the $N(s)$ polynomial) are known as the zeros of $H(s)$, the p_j elements, (or the roots of the $D(s)$ polynomial) are the poles of $H(s)$ and N is the order of $H(s)$.

Since the poles of a transfer function that represents a system are equal to the zeros of the characteristic equation of the system (1.8), an equivalent stability condition can be defined for the transfer function analysis:

$$Re(p_j) < 0 \qquad (j = 1, ..., N) \tag{1.15}$$

That is, the DC solution will be locally stable if all the p_j poles of the $H(s)$ transfer function have negative real parts.

All the transfer functions that represent the same system share the same denominator (also known as the characteristic equation of the system), that is, the same set of poles [33]. Hence, in principle, the stability of a DC solution can be assessed from a single closed-loop transfer function that represents the system.

Nonetheless, differences on the denominator might appear due to exact pole-zero cancellations caused by losses of controllability and observability from the analyzed observation ports.

1.2.2 Stability Analysis of a Periodic Solution

Let us consider the nonlinear system in (1.1), pumped by a large-signal input drive with period $T = 1/f_0$.

We then define a periodic solution $\overline{x}_0(t)$ with period T (1.16) and $\overline{\xi}(t)$, a small perturbation signal around the periodic solution $\overline{x}_0(t)$ (1.17).

$$\overline{x}_0(t) = \overline{x}_0(t+T) \tag{1.16}$$

$$\overline{x}(t) = \overline{x}_0(t) + \overline{\xi}(t) \tag{1.17}$$

In order for the periodic solution $\overline{x}_0(t)$ to be stable, $\overline{\xi}(t)$ must tend to zero for increasing values of t.

Introducing $\overline{x}(t)$ to (1.1) and linearizing the system around the periodic solution $\overline{x}_0(t)$, the following expression for the Periodic Linear Time-Varying (PLTV) system is obtained:

$$\dot{\overline{\xi}}(t) = \mathbb{G}(t)\ \overline{\xi}(t) \tag{1.18}$$

where $\mathbb{G}(t) = Jf(\overline{x}_0(t))$ is the Jacobian matrix evaluated around the periodic solution $\overline{x}_0(t)$ and its coefficients vary in time with period T.

The stability of a periodic large-signal solution can then be determined from the Floquet exponents (1.19) of the $\mathbb{G}(t)$ periodic Jacobian matrix of the linearized system in (1.18) as described in [1].

$$\lambda_i \pm jk\omega_0 \qquad i = 1, ..., n;\ k = -\infty, ..., \infty \tag{1.19}$$

Whilst many methods for the DC stability analysis of microwave circuits are included in commercial microwave circuit simulators, they

do not include reliable tools or methodologies for a systematic stability analysis of periodic solutions.

Some of the solutions, external to the commercial circuit simulation tools, are included in the literature [34]–[58]. The most popular methodologies have been summarized in the following paragraphs.

Nyquist Analysis of the Characteristic Determinant

In [34] Rizzolli et al. presented novel methodologies to determine the large-signal stability of periodic solutions.

Firstly, the analytical calculus of the linearization of the circuit is obtained from introducing small periodic perturbations, $e^{(\sigma+j\omega)t}$, to a large-signal steady state solution. Where $\sigma > 0$, and no relation exists between ω and the fundamental frequency ω_0.

Next, from an harmonic balance analysis the characteristic matrix of the perturbed system must be calculated. This matrix contains the information of the dynamics of all the variables of the linearized circuit, and all of the poles of its determinant (also known as the characteristic determinant, $\Delta(\sigma + j\omega)$) are on the left-hand side of the s plane.

The stability of the steady state periodic solution can be determined through a Nyquist analysis [35] of the characteristic determinant $\Delta(\sigma + j\omega)$.

The main drawback of this methodology is that the characteristic determinant is not available in commercial harmonic balance simulators and its computation cost is high.

In [39], Suárez et al. generalized the methodology presented in [34] to analyze the stability of quasi-periodic solutions obtained from harmonic balance via the introduction of auxiliary generators [36]–[38].

Nonlinear Normalized Determinant Function (NDF)

Since access to the characteristic determinant is restricted in commercial harmonic balance simulators, in [40] Mons et al. introduced the nonlinear *Normalized Determinant Function* (NDF). This work consists of the generalization to the large-signal regime of the method for stability of DC regimes introduced by Platzker et al. in [20].

From a nodal analysis, the NDF function can be simulated with commercial harmonic balance simulators. This function contains all the information regarding the dynamics of the system linearized around the large-signal periodic solution and has no right-hand side poles. Thus, by applying the Nyquist criterion [35], its large-signal stability can be assessed.

Stability under Mismatch Effects

Recently novel methodologies for the large-signal stability analysis have been proposed to analyze the stability under output mismatch effects [46]–[51].

The proposed methodologies tackle the multidimensional problem of generalizing the Rollet stability criteria to the periodic large-signal regime. This is achieved by checking the negative resistance condition at a variable frequency f_s, taking into account not only the load termination at frequency f_s, but also the load terminations at the $kf_0 \pm f_s$ frequencies. Where f_0 is the fundamental frequency and k is the number of relevant sidebands.

Eventually, the large-signal load termination stability boundaries are determined by applying the bifurcation theory and conversion matrix approach.

Stability Analysis from Transfer Function Analysis

The Floquet exponents can also be calculated from the closed-loop PLTV transfer function obtained trough the linearization of a system around its periodic solution as follows [54].

Similar as for the DC solution, a small input signal $\overline{u}(t)$ is introduced to the linearized system in (1.18) and the $\overline{y}(t)$ output signal is defined as a linear combination of the state vector as follows:

$$\begin{aligned} \dot{\overline{\xi}}(t) &= \mathbb{G}(t)\overline{\xi}(t) + \mathbb{B}(t)\ \overline{u}(t) \\ \overline{y}(t) &= \mathbb{C}(t)\overline{\xi}(t) + \mathbb{D}(t)\overline{u}(t) \end{aligned} \tag{1.20}$$

Analogously, all information regarding the stability of a nonlinear system around its periodic large-signal solution can also be determined from the poles of any of the closed-loop transfer functions that represents the system under analysis (1.21).

$$\overline{Y}(s) = \boldsymbol{H(s)}\overline{U}(s) \tag{1.21}$$

On account of the PLTV nature of the system in (1.18) resulting from the linearization of the periodic large-signal regime, the large-signal transfer function $\boldsymbol{H(s)}$ is no longer a Single-Input Single-Output (SISO) transfer function but a Multiple-Input Multiple-Output (MIMO) transfer function matrix that relates the multiple sidebands of the output signal with the input signal. Further information on the matrix nature of the PLTV transfer function and how to analyze its stability is described in the following section and in Chapter 4.

In any case, the periodic large-signal solution will be locally stable if all the poles of any of the transfer functions in $\boldsymbol{H(s)}$ have negative real parts.

1.3 Stability Analysis Through Pole-Zero Identification

Stability analysis through pole-zero identification consists of the frequency domain identification of a closed-loop frequency response as-

sociated to the linearization of a circuit around its DC or periodic large-signal solution. The stability or instability is then determined by checking if any of the poles of the identified transfer function are located in the right-hand side of the s plane [53]–[55].

The three main steps for stability analysis through pole-zero identification, for either the small-signal or periodic large-signal regimes, are the following.

Firstly, one must start by obtaining a closed-loop frequency response that represents the linearization of the circuit around its DC or periodic large-signal solution. As discussed in the previous section, the closed-loop frequency response is defined as the output of a system in response to an input frequency-varying small-signal stimulus. Simulations can be carried out on various CAD programs [59], [60], but obviously, different simulation engines will be used for the small-signal regime (AC analysis) and the periodic large-signal regime (mixer-mode harmonic balance analysis). Anyhow, valid simulation models that represent the components of the analyzed circuit with precision are required.

Secondly, frequency domain linear identification techniques are applied to obtain rational polynomial transfer functions from the closed-loop frequency responses obtained in the previous step. It should be noted that, unlike the first step, this second step is the same for frequency responses obtained in the DC regime and in the periodic large-signal regime.

Lastly, the poles and zeros of the identified transfer function are processed and plotted. As described in the previous section, by analyzing the poles of the identified transfer function and verifying if unstable poles (poles on the right-hand side of the s plane) have been identified, the stability or instability of the analyzed DC or periodic large-signal solution can be determined. Furthermore, additional information regarding the origin of the spurious oscillations can be inferred [61].

The STAN tool [62], created by the RF and Microwave Research Group of the Department of Electricity and Electronics of the *University of the Basque Country (UPV/EHU)* in collaboration with *Centre National d'Études Spatiales* (CNES) [63] and distributed by *AMCAD Engineering* [64], offers a stability analysis technique for the small-signal and periodic large-signal regimes.

A stability analysis carried out with the STAN tool consists of detecting and determining the nature of oscillations from SISO or parametric SISO frequency responses. Further reading on this technique and tool can be found in [65]–[72].

1.3.1 Obtaining Frequency Responses

The first step for analyzing the stability through pole-zero identification consists of obtaining a closed-loop frequency response that represents the system under analysis. The closed-loop frequency responses can either be obtained in simulation or measurement [73]–[76].

Frequency responses of a system can be obtained in simulation by introducing small-signal current or voltage probes on one or multiple nodes and branches of a circuit, granted that the insertion of the probes does not modify the steady state of the circuit under analysis.

As described in [53], small-signal current sources should be inserted in parallel (impedance analysis) and small-signal voltage sources should be introduced in series (admittance analysis).

That is, the frequency response of the linearized circuit can be obtained as the impedance $Z^n(j\omega)$ (1.22) seen by a small-signal current source i_{in} connected in parallel at a given node n (Figure 1.1a).

$$Z^n(j\omega) = \frac{v^n(j\omega)}{i_{in}(j\omega)} \tag{1.22}$$

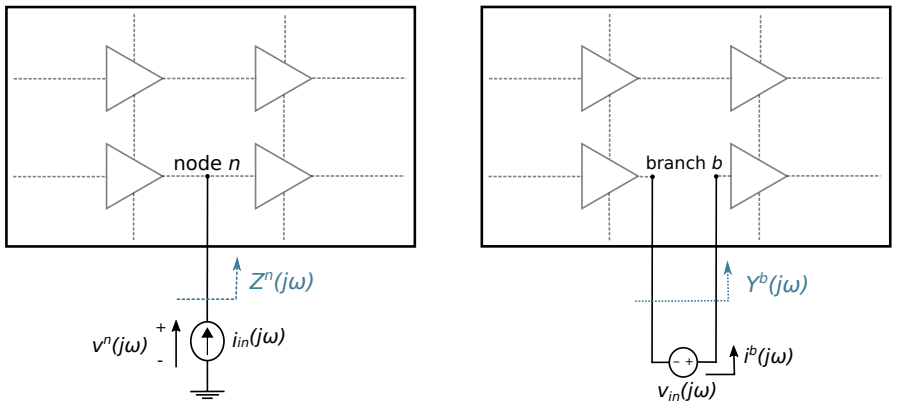

(a) (b)

Figure 1.1: Illustration of methods for obtaining SISO frequency responses. (a) Introduction of a small-signal current source in parallel at node n of a circuit (impedance analysis). (b) Introduction of a small-signal voltage source in series at branch b of a circuit (admittance analysis).

Or as the admittance $Y^b(j\omega)$ (1.23) seen by a small-signal voltage source v_{in} connected in series at a particular branch b (Figure 1.1b).

$$Y^b(j\omega) = \frac{i^b(j\omega)}{v_{in}(j\omega)} \tag{1.23}$$

Obviously, the simulation engines required for probing the circuit differ for the small-signal and periodic-large-signal regime. An AC analysis must be carried out to obtain a closed-loop frequency response for the small-signal regime and a mixer-mode harmonic balance analysis must be carried out to obtain a closed-loop frequency response for the periodic large-signal regime.

DC Regime

For a stability analysis of a DC solution of a circuit, a small-signal probe that does not vary the DC steady state must be introduced at

any given observation port of the circuit. Additionally, no input power is introduced to the circuit, only the DC bias.

The frequency response is obtained through a linear analysis that calculates the impedance or admittance at a given observation port of the analyzed circuit, depending on the type of small-signal probe that is introduced, for a given frequency band ($[f_{min},\ f_{max}]$). In order to do so, the f_s frequency of the small-signal probe must be swept from f_{min} to f_{max}, specifying the number of data points. Choosing the whole frequency range at which the active devices present gain is advised for a precise small-signal stability analysis.

Periodic Large-Signal Regime

For a periodic large-signal pole-zero stability analysis, a small-signal probe at frequency f_s that does not vary the periodic steady state under analysis must be introduced at any given observation port of the analyzed circuit. The impedance or admittance closed-loop frequency responses are then obtained by performing a mixer-mode harmonic balance simulation where the input drive at f_0 plays the role of the oscillator and the f_s frequency of the small-signal probe represents the RF signal [77].

In order to obtain the frequency responses for the periodic large-signal stability analysis, the f_s frequency value of the small-signal probe is varied throughout a fixed frequency band ($[f_{min},\ f_{max}]$).

Given that the linearization of the large-signal periodic steady state results in a PLTV system, the small-signal input signal $u(s)$ (a current or voltage signal depending on the introduced probe) consists of a single frequency component at f_s. But the output signal $y(s)$ will consist of multiple frequency components at the frequency values in (1.24):

$$kf_0 \pm f_s \qquad k = -NH, ..., 0, ..., NH \tag{1.24}$$

where NH is the number of significant harmonics of the fundamental frequency f_0.

Consequently, PLTV systems can not be represented by a single Linear Time Invariant (LTI) SISO transfer function. Instead, $2NH+1$ frequency responses, $H_k(j\omega_s)$ for $\forall k \in [0, NH]$, that relate the output signal at the different sidebands with the input signal at f_0 can be defined (Figure 1.2).

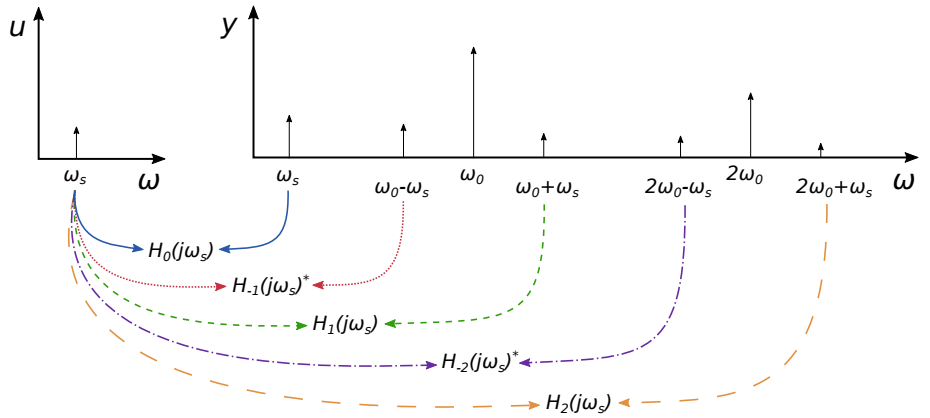

Figure 1.2: Transfer functions $H_k(j\omega_s)$ for $NH = 2$, $-2 \leq k \leq 2$.

For example, in the case of the introduction of a small-signal current source (impedance analysis) at node n, the $H_k^n(j\omega_s)$ transfer functions for $\forall k \in [0, NH]$ are defined as in (1.25).

$$
\begin{aligned}
H_0^n(j\omega_s) &= Z_0^n(j\omega_s) = \frac{v^n(\omega_s)}{i_{in}(\omega_s)} \\
H_k^n(j\omega_s) &= Z_k^n(j\omega_s) = \frac{v^n(k\omega_0 + \omega_s)}{i_{in}(\omega_s)} \\
H_{-k}^n(j\omega_s) &= Z_{-k}^n(j\omega_s) = \left[\frac{v^n(k\omega_0 - \omega_s)}{i_{in}(\omega_s)}\right]^*
\end{aligned}
\tag{1.25}
$$

It should be noted that all the $H_k^n(j\omega_s)$ frequency responses share the same denominator, that is, the same set of poles, except for exact pole-zero cancellations. Consequently, in principle, the same stability information can be obtained from any of the $H_k^n(j\omega_s)$ frequency responses.

The poles of the $H_k^n(j\omega_s)$ transfer functions are also known as the Floquet exponents of the system [54]–[56] and they appear repeated periodically throughout the frequency response. Consequently, for a periodic large-signal stability analysis, by analyzing only the frequency band $[0,\ f_0/2]$ all the possible unstable poles or their Floquet exponents should be detected in principle, unless the unstable dynamics are not observable from the detected observation ports.

Selecting the Observation Port

The stability analysis that consists of analyzing SISO frequency responses obtained at a particular observation port is often linked to problems of loss of controllability and observability.

From a theoretical point of view, all of the nodes and branches of a circuit provide the same stability information. Nevertheless, depending on the isolation between the unstable feedback loop and the selected observation port, the unstable poles might be correctly detected or missed. This is due to the fact that resonances are detected clearly on the observation ports that are within the feedback loops responsible for the critical resonance, but not always on the nodes or branches that are electrically isolated from the feedback loops [78].

For example, the pole-zero diagrams in Figure 1.4 represent the identification results of three frequency responses obtained at the input nodes of the three stages of the multistage amplifier in Figure 1.3. The unstable feedback loop being on the third stage, the unstable poles are not detected from the frequency response obtained at the first stage. But the unstable poles are detected quasi-compensated by zeros, that is, with low observability, at the second stage. Lastly, the unstable

poles are detected clearly for the frequency response obtained at the third stage.

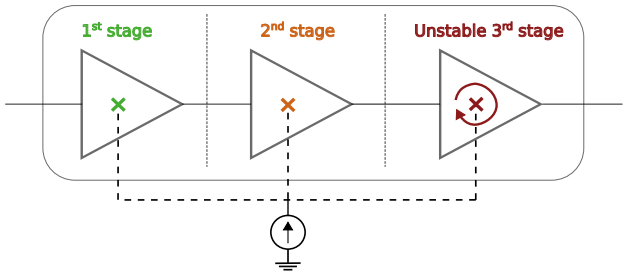

Figure 1.3: Diagram of an unstable three-stage circuit, where the nodes selected for stability analysis are indicated. The unstable feedback loop is located on the third stage, thus, the unstable dynamics cannot be detected at the first stage and it is detected with low sensitivity at the second stage.

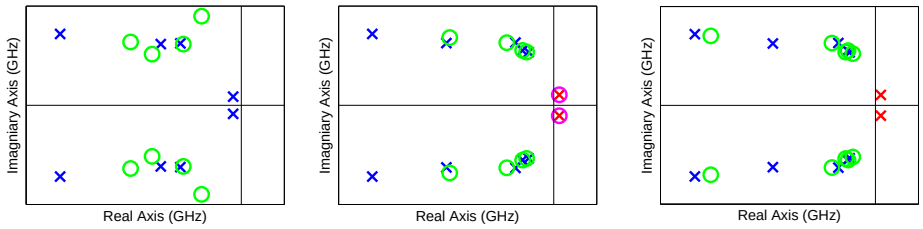

(a) (b) (c)

Figure 1.4: (a) Pole-zero map obtained at the first stage, no observability and controlability. (b) Pole-zero map obtained at the second stage, low observability and controlability. (c) Pole-zero map obtained at the third stage, high observability and controlability.

A sensitivity enhancement technique that focuses on analyzing single nodes (SISO) with dual current-voltage probes is proposed in [79]. This probe can be used to introduce a small-signal current probe (in parallel) and a small-signal voltage probe (in series), sequentially at a given observation port of the circuit. This way, two frequency responses are obtained from a single simulation (with a double sweep), increasing the sensibility of SISO stability analysis.

1.3.2 Transfer Function Identification

There are many algorithms that solve the difficult problem of formulating a continuous transfer function from a measured or simulated frequency response [80], [81]. One must analyze the convergence of each algorithm and the validity of the obtained transfer functions (for noisy frequency responses, for example) in order to determine which algorithm best suits each application.

In particular, the Least Square algorithm is the frequency domain identification algorithm used by pole-zero stability analysis tools, such as STAN [62].

Undermodeling and Overmodeling

The order of a transfer function required to fit a closed-loop frequency response that represents the linearization of a microwave circuit around its DC or periodic large-signal solution is *a priori* unknown [66],[72]. Thus, when identifying transfer functions for microwave and RF circuits, the required order must be approximated either manually or automatically via numerical approximations.

Despite the reliability of existing automatic order selection methods, designers might encounter unwanted undermodeling or overmodeling effects which often complicate the understanding of the obtained pole-zero diagrams and might lead to incorrect conclusions on the stability of the circuit [66].

Undermodeling occurs when the fitting order is too low and the transfer function identification results in a poorly fitted response.

Overmodeling occurs when the fitting is carried out with an excessively high order. The transfer functions identified with unnecessarily high orders will be precise at the expense of the appearance of mathematical quasi-cancellations that, principally if unstable, complicate the interpretation of the results.

The set of magnitude, phase and pole-zero diagrams in Figure 1.5 serve to illustrate the importance of the correct selection of the order for fitting transfer functions.

The effects of undermodeling can be perceived in the curves identified with order 2 shown in Figure 1.5a. No poles are identified in the frequency band under analysis and the inaccuracy of the fitting can be determined by sight from the magnitude and phase curves.

Sufficient precision is achieved with the fitting carried out with order 6, as can be verified by sight from the magnitude and phase curves in Figure 1.5b. A pair of physical unstable complex conjugate poles quasi-compensated by zeros are detected.

Finally, the identification results for order 10 show high precision, as in the case of $N = 6$, but additional unstable mathematical pole-zero quasi-cancellations are identified as shown in Figure 1.5c.

For large frequency band analyses, selecting the order manually and distinguishing physical and mathematical quasi-compensations can be challenging and could lead to erroneous conclusions. Instead of focusing on physical poles, the user might waste time trying to stabilize a mathematical unstable pole that is in reality product of overmodeling.

1.3.3 Pole-Zero Diagram Analysis

For a correct detection of possible spurious oscillations one must analyze the identified transfer functions. This can be done by analyzing and preferably plotting the identified poles and zeros.

As discussed previously, if poles with positive real parts are detected, the system will be unstable and an oscillation will start-up at the frequency given by the imaginary part of the identified unstable poles.

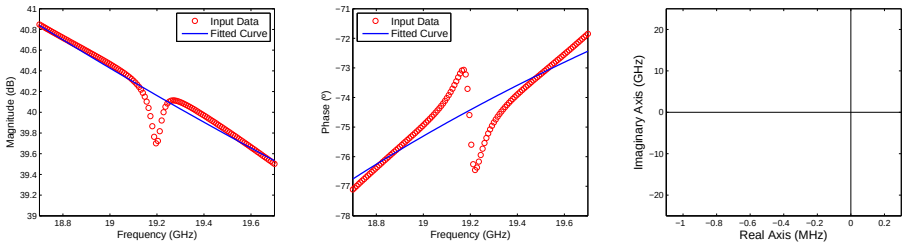

(a) Identification order N=2. Example of undermodeling.

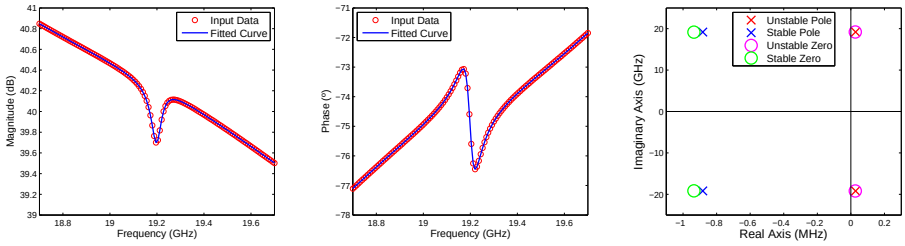

(b) Identification order N=6. Example of correct selection of the order.

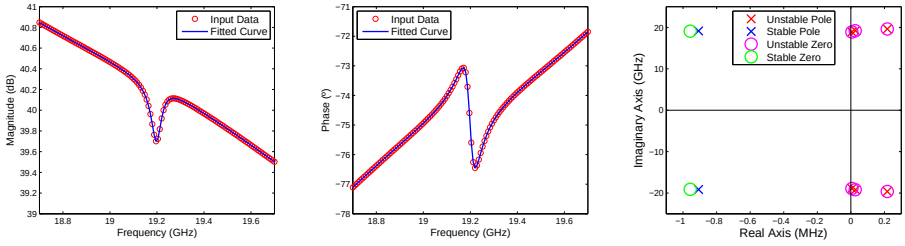

(c) Identification order N=10. Example of overmodeling.

Figure 1.5: Illustration of the importance of a correct selection of the order for the fitting of the transfer function.

One can also analyze the system and its instability in depth from the additional information provided by the poles and zeros identified from the frequency responses obtained at different observation ports of the circuit, in order to eliminate spurious oscillations as discussed in the following section 1.4.

1.4 Stabilization from Pole-Zero Identifications

In [61], a systematic stabilization methodology of multi-transistor circuits was introduced. This methodology can be applied to determine the location and value of the series or shunt stabilization networks required to stabilize an instability at the DC or small-signal regime. Applying standard linear control theory techniques to a SISO closed-loop transfer function, obtained at a given node or branch of the circuit, the position of the poles versus the stabilization parameter can be determined.

As stated in [61], given an impedance or admittance transfer function $H(s)$, it should be possible to apply standard techniques of linear control theory (Figure 1.6) to determine whether the inclusion of a negative feedback can provide a stable closed-loop system.

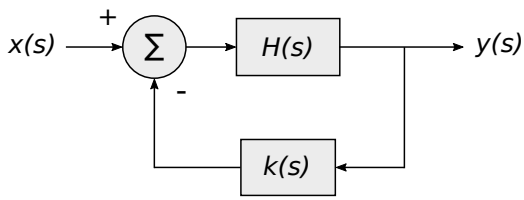

Figure 1.6: Block diagram of a closed-loop control system.

The closed loop transfer function $H_{cl}(s)$ can be expressed as in equation (1.26), where $N(s)$ and $D(s)$ are the numerator and denominator, respectively, of $H(s)$.

$$H_{cl}(s) = \frac{H(s)}{1 + k(s)H(s)} = \frac{N(s)}{D(s) + k(s)N(s)} \tag{1.26}$$

The evolution of the poles of the closed-loop transfer function for variations of the feedback transfer function $k(s)$ in Figure 1.6 is known as the root-loci [82],[83].

For a purely proportional action, that is, the series or parallel inclusion of a stabilization resistor, the feedback term is a constant factor k. Other alternatives include the series or parallel inclusion of a reactive element, such as an capacitance or inductance, for a derivative or integral control action.

For the particular case of stabilization of microwave circuits, the closed-loop transfer functions generated when introducing series or shunt stabilization networks, $Z^n_{cl}(s)$ (1.27) and $Y^b_{cl}(s)$ (1.28) respectively, are the following (Figure 1.7).

The parallel connection of a stabilization network $Z_{stab}(s)$ at node n (Figure 1.7a) generates a closed-loop impedance transfer function $Z^n_{cl}(s)$ (1.27). From (1.27) it is determined that the inclusion in parallel of the stabilization network $Z_{stab}(s)$ performs a negative feedback $1/Z_{stab}(s)$ on the linear system $Z^n(s)$.

$$Z^n_{cl}(s) = \frac{v^n(s)}{i_{in}(s)} = \frac{Z^n(s)Z_{stab}(s)}{Z^n(s) + Z_{stab}(s)} = \frac{Z^n(s)}{1 + \frac{Z^n(s)}{Z_{stab}(s)}} \tag{1.27}$$

Similarly, the series connection of a stabilization network $Y_{stab}(s)$ at branch b (Figure 1.7b) generates a closed-loop admittance transfer function $Y^b_{cl}(s)$ (1.28). From (1.28) it is determined that the inclusion in series of the stabilization network $Y_{stab}(s)$ performs a negative feedback $1/Y_{stab}(s)$ on the linear system $Y^b(s)$.

$$Y_{cl}^{b}(s) = \frac{i^{b}(s)}{v_{in}(s)} = \frac{Y^{b}(s)Y_{stab}(s)}{Y^{b}(s) + Y_{stab}(s)} = \frac{Y^{b}(s)}{1 + \frac{Y^{b}(s)}{Y_{stab}(s)}} \tag{1.28}$$

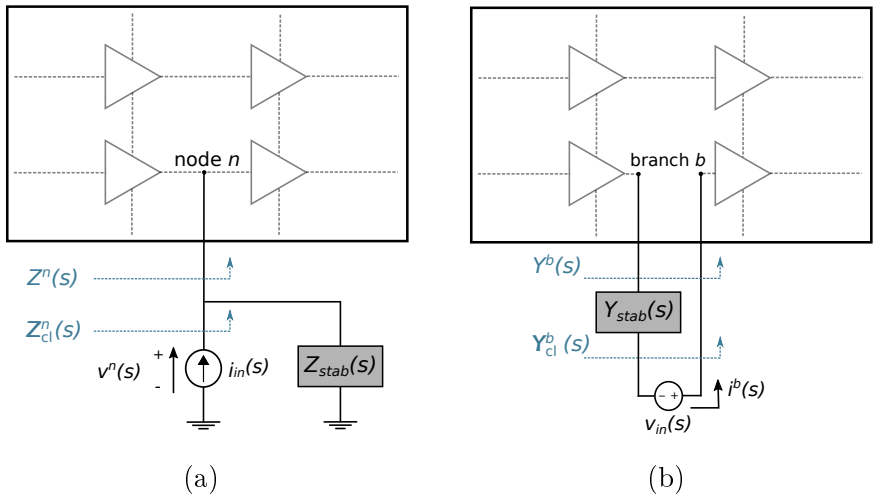

(a) (b)

Figure 1.7: (a) Parallel connection of a stabilization network within impedance stability analysis. (b) Series connection of a stabilization network within admittance stability analysis.

Therefore, introducing a R_{stab} resistor in series at a given branch is equivalent to applying a proportional control $k = 1/Y_{stab}$ to $H(s) = Y^{b}(s)$ (1.26), where $Y_{stab} = 1/R_{stab}$. Whilst introducing a R_{stab} resistor in parallel at a given node is equivalent to applying a proportional control $k = 1/Z_{stab}$ to $H(s) = Z^{n}(s)$ (1.26), where $Z_{stab} = R_{stab}$.

However, in order for the stabilization methodology in [61] to be applicable, one must first ensure that the introduced stabilization network does not alter the DC steady state solution.

As a final note, the nodes or branches of the circuit at which the unstable complex conjugate poles appear isolated should be selected

for the small or large-signal stabilization introduced in [61]. In other words, the detection of unstable zeros near unstable poles for a frequency response obtained at a given observation port of the circuit indicates low controlability of the unstable dynamics from that observation port. Thus, the observation ports with low controlability of the unstable dynamics should be discarded for stabilization.

1.5 Conclusions

In this chapter, the main frequency domain stability methods for small and large-signal operation have been introduced. These stability analysis methods are essential for the design of stable microwave amplifiers since the most popular CAD tools for designing and simulating microwave active circuits [59], [60] do not predict instabilities.

Special emphasis has been placed on the pole-zero stability analysis method that consists of fitting transfer functions associated to the frequency responses obtained from introducing small-signal current or voltage probes to the circuit and analyzing its poles and zeros. The main advantage of this method is its simple application and that it can be applied for small-signal and periodic large-signal stability analyses.

Finally, the systematic stabilization methodology for small-signal instabilities introduced in [61] has been briefly described. By applying this method one can determine the values of series or shunt stabilization networks required to stabilize an unstable design.

2 Stability Analysis of Multistage Power Amplifiers Using Multiple-Input Multiple-Output Identification

2.1 Introduction

Single-Input Single-Output (SISO) pole-zero identification has widely demonstrated its value for the detection of undesired oscillations in power amplifiers. However this technique suffers from two main drawbacks.

On the one hand, SISO pole-zero identification is linked to potential losses of controllability and observability. In principle, all the closed-loop transfer functions of a same system share the same poles, that is, the same characteristic equation. However, due to the lack of observability at some observation ports, discrepancies may arise in the poles obtained from different frequency responses that represent the same system. Consequently, the detection of possible instabilities can be missed if the observation port is not selected wisely [55], [61], [79].

On the other hand, a problem general to any identification process is that the order of the transfer function to be fitted is *a priori*

unknown. Thus, designers can encounter unwanted overmodeling and undermodeling effects when analyzing the identification results [66]. When identifying a frequency response with an excessively high fitting order, also known as overmodeling, mathematical unstable pole-zero quasi-compensations might appear that can easily be mistaken with physical oscillations. Undermodeling can also lead to erroneous conclusions, since an identification carried out with a fitting order that is too low might miss the detection of a physical instability.

With the intent of overcoming the mentioned limitations and adding new features to improve user experience, a new pole-zero stability analysis tool that also includes Multiple-Input Multiple-Output (MIMO) pole-zero identification has been designed in *Matlab* [84].

The Vector Fitting algorithm [85]–[88] has been selected for the frequency domain identification of the poles and zeros of the transfer function mainly because it favors the implementation of MIMO identifications.

Additionally, new strategies for reducing the effects of overmodeling have been included, such as, an improved representation of the identified poles and zeros, the creation of an automatic order selection algorithm and a quantitative factor (ρ) capable of determining the location of the unstable feedback loops of a multistage power amplifier. The applicability and efficiency of the ρ factor for detecting the critical nodes of a multistage amplifier is demonstrated via the stability analysis and stabilization of a three-stage L-band power amplifier prototype designed *ad hoc* for this thesis. Moreover, the mentioned ρ factor can be applied to detect mathematical pole-zero quasi-compensations resulting from overmodeling.

2.2 Vector Fitting

Vector Fitting [85]–[88] is a general methodology for the fitting of frequency domain responses with rational function approximations. It

was developed by B. Gustaven and A. Semlyen in 1996 and was made available two years later as a public *Matlab* routine [84], [89].

Due to its capacity to fit multiple frequency responses with the same set of poles, Vector Fitting is ideal for precise MIMO stability analyses that avoid discrepancies in the poles obtained from different transfer functions of a same system.

When fitting a frequency response $H(j\omega)$ in (2.1), the Vector Fitting algorithm estimates the p_k system poles, the r_k residues and the real direct gain d of the transfer function $H(s)$, expressed as a rational function approximation and with order N.

$$H(s) = \sum_{k=1}^{N} \frac{r_k}{s - p_k} + d \tag{2.1}$$

The fitting is achieved by iteratively relocating a set of initial poles whilst reducing the quadratic error of the fitting. In order to do so, the user must externally choose the order N of the transfer function to be fitted, and he or she must also define the set of initial poles.

Vector Fitting solves the nonlinear equation in (2.1) as a linear problem in two steps [85], [86]. These two steps are repeated, setting the final poles determined on the previous iteration as the initial poles for the next iteration, until a given number of iterations have been executed.

1^{st} step: Pole Identification

As a first step, two auxiliary functions $\sigma(s)$ and $x(s)$ are defined:

$$\sigma(s) = \sum_{k=1}^{N} \frac{\widetilde{r}_k}{s - \overline{p}_k} + 1 \tag{2.2}$$

$$x(s) = \sum_{k=1}^{N} \frac{\hat{r_k}}{s - \overline{p}_k} + \hat{d} \tag{2.3}$$

where $\overline{p}_k$ are the poles of both functions, $\hat{r_k}$ and $\widetilde{r}_k$ are the residues of the $x(s)$ and $\sigma(s)$ functions respectively and $\hat{d}$ is the real direct gain of $x(s)$.

As shown in (2.2) and (2.3), both functions share the same set of $\overline{p}_k$ poles. It should be noted that the $\overline{p}_k$ poles are the set of initial poles that are defined externally by the user.

Additionally and by definition, the auxiliary functions $\sigma(s)$ and $x(s)$ in (2.2) and (2.3) are related to the objective fitted transfer function H(s) in (2.1) as follows:

$$x(s) = \sigma(s)H(s) \tag{2.4}$$

Evaluating (2.4) for several frequency points gives the overdetermined linear problem in (2.5), which can be solved as a Least Squares problem, leading to the determination of the $\widetilde{r}_k$, $\hat{r_k}$ and $\hat{d}$ unknowns.

$$\left(\sum_{k=1}^{N} \frac{\hat{r_k}}{s - \overline{p}_k} + \hat{d} \right) = \left(\sum_{k=1}^{N} \frac{\widetilde{r}_k}{s - \overline{p}_k} + 1 \right) H(s) \tag{2.5}$$

A rational approximation for $H(s)$ can be obtained by rewriting the equation in (2.5) as a ratio of two polynomials:

$$x(s) = \frac{\prod_{k=1}^{N} (s - \hat{z_k})}{\prod_{k=1}^{N} (s - \overline{p}_k)} \qquad \sigma(s) = \frac{\prod_{k=1}^{N} (s - \widetilde{z}_k)}{\prod_{k=1}^{N} (s - \overline{p}_k)} \tag{2.6}$$

where $\overline{p}_k$ are the poles and $\hat{z}_k$ and $\widetilde{z}_k$ are the zeros of the $x(s)$ and $\sigma(s)$ functions respectively.

From equations (2.4) and (2.6), one realizes that the poles of $H(s)$ are equal to the $\widetilde{z}_k$ zeros of $\sigma(s)$. As a consequence, the initial poles are eliminated from the problem. This realization gives way to a simple method to fit the poles for the $H(s)$ transfer function in (2.1), that consists of determining the $\widetilde{z}_k$ zeros of $\sigma(s)$.

$$H(s) = \frac{x(s)}{\sigma(s)} = \frac{\prod_{k=1}^{N}(s - \hat{z}_k)}{\prod_{k=1}^{N}(s - \widetilde{z}_k)} \tag{2.7}$$

Since the residues of $\sigma(s)$ have been calculated previously and its poles are the chosen starting poles, all the unknowns of the sum of partial functions of $\sigma(s)$ in (2.2) are known. Consequently, the zeros of $\sigma(s)$, or equivalently, the poles of $H(s)$, can be calculated easily by rewriting the function as a ratio of two polynomials, as in (2.6). This potentially complex calculation is simplified as described in appendix A and B of [85].

2^{nd} step: Residue Identification

The r_k residues of $H(s)$ can be calculated solving the equation in (2.1), given that the p_k poles are the zeros of $\sigma(s)$ that have been determined previously. Therefore, as a final step, the new overdetermined linear problem must be solved to determine the r_k and d unknowns in (2.1).

Additional Advantages of Using Vector Fitting

The Vector Fitting algorithm was selected as the frequency domain fitting algorithm mainly due to its capacity to calculate multiple continuous transfer functions with the same denominator from a given set of frequency responses.

Nonetheless, when comparing Vector Fitting with other frequency domain fitting algorithms commonly used for stability analysis, such as the Least Squares algorithm, and after testing it thoroughly, other advantages were found.

Compared to the representation as a ratio of two polynomials (2.8), the partial fraction representation used by Vector Fitting (2.1) is numerically better conditioned for RF and microwave applications.

$$H(s) = \frac{(s - z_1)...(s - z_N)}{(s - p_1)...(s - p_N)} = \frac{a_0 + a_1 s + ... + a_N s^N}{b_0 + b_1 s + ... + b_N s^N} \tag{2.8}$$

In (2.8), p_k are the system poles, z_k are the system zeros and N is the order of the $H(s)$ transfer function.

However, it should be noted that with the Vector Fitting algorithm, the resulting fitted model can be expressed in either the pole-residue form in (2.1) or the state-space form in (2.9):

$$H(s) = \mathcal{C}(sI - \mathcal{G})^{-1}\mathcal{B} + \mathcal{D} \tag{2.9}$$

where the $\mathcal{G}$ and $\mathcal{B}$ matrices contain information regarding the set of identified poles of the $H(s)$ transfer function. Whilst the $\mathcal{C}$ and $\mathcal{D}$ matrices contain information regarding the residues and direct gain, respectively, of the $H(s)$ transfer function.

For frequency responses with high frequency values with large bandwidths and consequently high orders, the Least Squares identification algorithm must compute the $s^i = (j\omega)^i$ terms in (2.8). The fitting is likely to be numerically ill-conditioned whenever the frequency values are excessively large. That is, the Least Squares method is often not capable of ensuring low fitting errors when the frequency responses have multiple resonances and therefore require high orders.

Fortunately, the partial fractions representation employed by Vector Fitting (2.1) avoids the calculation of the high valued powers of $j\omega$ [85] and thus is better conditioned for high frequency values and large bandwidths.

For example, Figure 2.1a is one of the multiple examples that serves to illustrate that the Least Squares algorithm is not capable of correctly identifying frequency responses that require orders higher that 30 with precision. Even with an order $N = 60$, the phase error between the frequency response and the identified transfer function cannot be reduced. The phase error is as high as 50° at low frequencies. Additionally, a considerable amount of stable and unstable mathematical quasi-compensations appear that make the interpretation of the results impossible.

However, the same example identified with Vector Fitting and an order $N = 60$ is fitted with precision (the phase error is below 0.5°). And a single pair of physical unstable complex conjugate poles quasi-compensated by zeros at 130 MHz are correctly detected.

The mentioned numerical problems of the Least Squares method are avoided in [66],[70] on account of the divide and conquer strategy.

The divide and conquer strategy consists of dividing large-band frequency responses into smaller more attainable frequency sub-bands. Moreover, to avoid numerically ill-conditioned identifications, each frequency band is also normalized before fitting it in [66],[70]. However, since the identified poles consist of the superposition of the poles identified for the multiple frequency sub-bands, the resulting pole-zero diagram and transfer function do not constitute a model of the circuit. Nonetheless, the stability analysis carried out from the transfer function identified with the divide and conquer strategy is accurate, even if the fitted poles do not constitute a model of the circuit.

On the contrary, a clear advantage of the Vector Fitting algorithm is that as no subdivision is required, the resulting pole-zero diagram and transfer function do correspond to a model of the circuit.

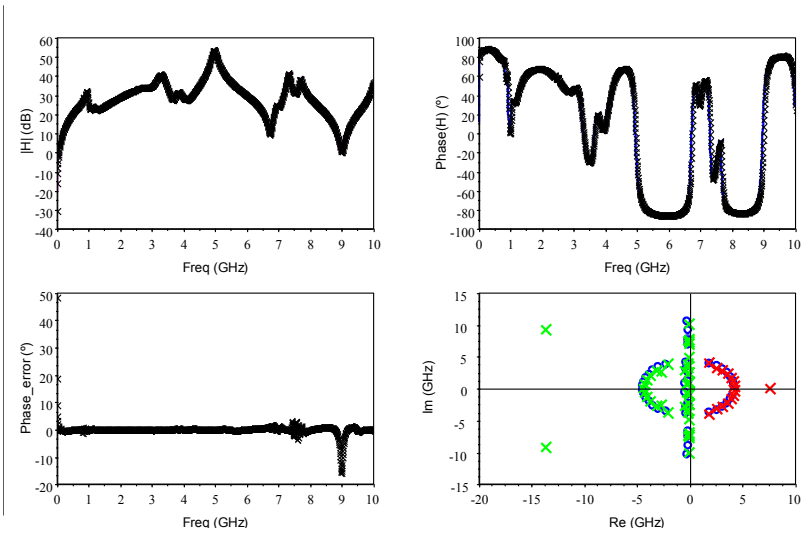

(a)

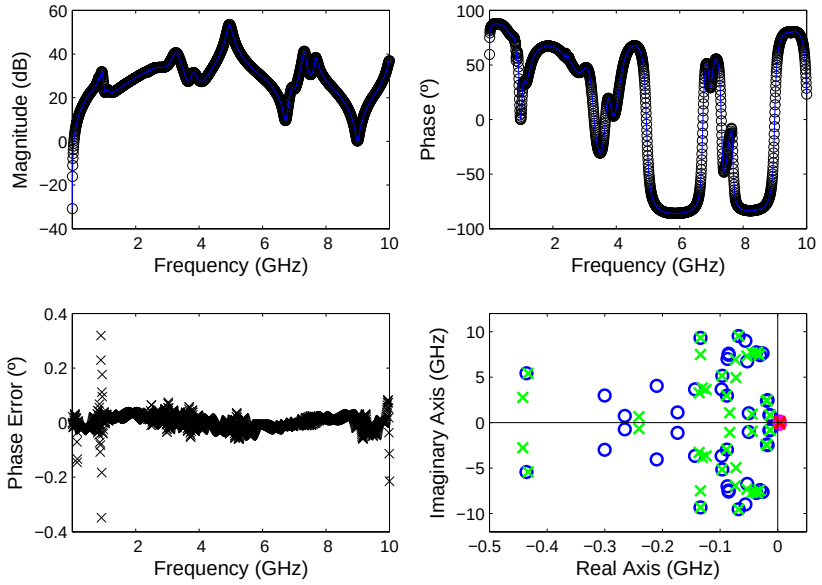

(b)

Figure 2.1: Comparison of the fitting of a large bandwidth frequency response identified with order $N = 60$ and (a) the Least Squares algorithm. (b) the Vector Fitting algorithm.

2.3 MIMO Pole-Zero Identification Tool

On a SISO pole-zero stability analysis the detection of an instability depends on the observability of the unstable dynamics from the selected observation port. For that reason, frequency responses obtained at different circuit nodes are usually analyzed [55].

By definition, all the input-output transfer functions of a linear (or linearized) system share the same denominator [33]. However in the context of stability analysis, until now, multiple frequency responses of a same system were identified as sequences of independent SISO analyses, and consequently, the identified poles for each frequency response were often similar but not quite identical. These differences may be negligible for the poles that are closest to the Y-axis but rather significant for the poles with large real parts or for poles that are quasi-compensated by zeros.

Hence, the most consistent approach for MIMO pole-zero analysis is forcing the same denominator for all the identified transfer functions.

Compared to the multiple independent SISO identification approach, the MIMO identification approach has the advantage of avoiding the discrepancies between the poles identified for each transfer function of a same system, as illustrated in Figure 2.2.

The MIMO frequency responses can be the impedances presented at small-signal current sources injected sequentially at different nodes, or the admittances presented at small-signal voltage sources injected sequentially at different circuit branches (or a combination of impedance and admittance frequency responses). Alternatively, other closed-loop linear responses (voltage-voltage or current-current) are also valid. When analyzing the stability of a large-signal steady state, any of the harmonic components of the parametric transfer function representing the Periodic Linear Time-Variant system (PLTV) can also be part of the same set [54],[90].

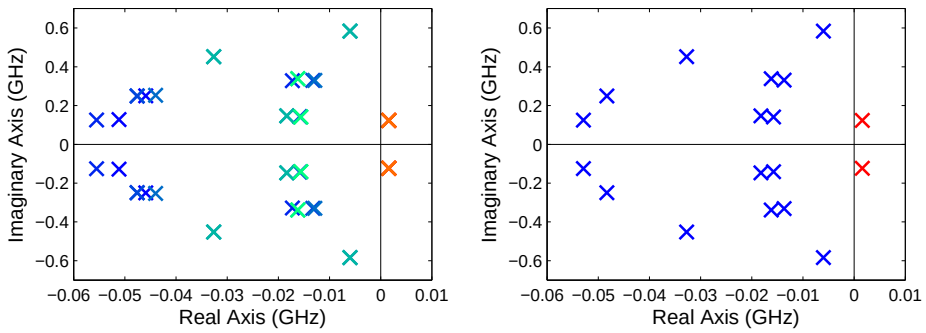

(a) (b)

Figure 2.2: Comparison of the poles corresponding to different frequency responses of a same system identified as (a) a sequence of independent SISO analyses. (b) a MIMO analysis establishing the same denominator. We observe that the differences between the poles identified as independent SISO identifications and MIMO identifications are generally smaller for the poles that are closest to the Y-axis.

From a sensitivity point of view, we propose a systematic MIMO pole-zero stability analysis approach that reduces the uncertainty of selecting the observation port for SISO pole-zero stability analyses. The systematic MIMO pole-zero stability analysis consists of selecting the gate (or base) and drain (or collector) nodes or branches of at least one of the transistors of each stage. Therefore, the systematic MIMO approach maximizes the chances of detecting the inner loop responsible for the critical resonance.

For a systematic MIMO pole-zero stability analysis, we depart from a set of frequency responses obtained at different observation ports of at least one transistor of each stage of the multistage amplifier.

Introducing voltage sources for MIMO analyses is more cumbersome since it implies breaking multiple branches in order to insert the voltage source in series. Therefore, inserting current sources as in Figure 2.3 is more generally used for carrying out MIMO pole-zero stability analyses.

As illustrated in Figure 2.3, in order to introduce the small-signal current source sequentially into the M nodes of the circuit, M ideal filters are introduced. The M frequency responses can be obtained from a single parametric simulation that varies a variable defined as *node* from $node = [1, ..., M]$. The variation of the *node* variable determines the functioning of the M ideal filters as follows. Each *filter* i ($i = [1, ..., M]$) presents a very high impedance (ideally an open circuit) to the small-signal current source when $node \neq i$ and a very low impedance (ideally a short circuit) when $node = i$.

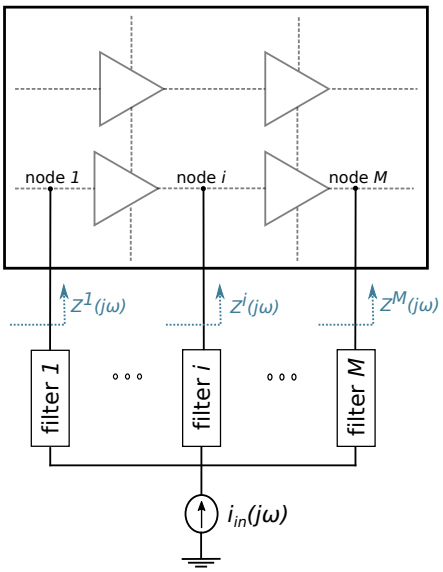

Figure 2.3: Illustration for obtaining MIMO frequency responses with a current probe introduced sequentially at different nodes of the circuit.

In order to carry out MIMO pole-zero identification based stability analyses, fitting the same set of poles to the identified transfer functions, a novel stability analysis tool (*MM_stab*) based on Vector Fitting [85], [89] has been created in *Matlab* [84]. Nevertheless, *MM_stab* is not limited to MIMO analysis, it can also analyze SISO, parametric SISO and parametric MIMO frequency responses.

The developed stability analysis tool can be used following three simple steps, as with STAN. First, the designer must obtain the SISO or MIMO closed-loop frequency responses of the system either via simulation or measurement. Next, by running the *MM_stab* tool for the mentioned frequency responses, the associated transfer functions are identified with Vector Fitting. Finally, from analyzing the obtained pole (or pole-zero) maps the stability or instability of the circuit can be determined.

An extensive study of the Vector Fitting options and parameters has been carried out in order to determine the best suited default values for the stability analysis application. Once the optimum Vector Fitting identification settings were selected, many other features were introduced to the *MM_stab* tool, such as an automatic order selection algorithm, an improved representation of the identified poles and zeros and a residue analysis strategy. Consequently a robust SISO and MIMO stability analysis tool has been designed.

The most important features of the developed tool are presented in the following subsections.

2.3.1 Automatic Identification Algorithm

An automatic order selection algorithm was generalized from [66], for selecting the minimum order required to obtain the fitting goal determined by the user.

The algorithm consists of an iterative procedure with a bottom-up approach that uses the θ_{error} phase error between the input data and the fitted transfer function for the quality assessment of the identification. The order of the identified transfer function is increased until the resulting θ_{error} is below a phase error tolerance value θ_{max} introduced by the user ($\theta_{error} \leq \theta_{max}$), for all the frequencies of the frequency band under analysis.

Firstly, the amount of resonances r on the complete frequency response are counted. This is done by counting the number of data

points for which the sign of the slope of the magnitude curve changes. As an initial approximation, we assume that the lowest order possible for fitting the transfer function is equal to the counted number of slope changes, $N_{initial} = r$.

For noisy responses, choosing the previously determined $N_{initial} = r$ might be excessive and could lead to overmodeling. To prevent this, the automatic order selection algorithm also counts the number of slope changes that are distanced from one another by at least 5 data points, r'. A frequency response is classified as noisy if $r' \leqslant r - 4$, and for these cases the initial order is set to $N_{initial} = r'$.

In MIMO identifications, in order to reduce the run time of the identification of M frequency responses, the initial order is obtained from the frequency response with the most resonances, $N_{initial} = r_{max}$ where $r_{max} = max\,(r_1, ..., r_M)$.

Secondly and once $N_{initial}$ is selected, the initial poles are defined. Following the indications in [85], the selected initial poles consist of complex conjugate poles with weak attenuation and imaginary parts that cover the entire frequency band under analysis.

After having defined the initial poles, the first identification is carried out. If the resulting θ_{error} is below the selected θ_{max} for all the frequencies of the frequency band under analysis, the criteria established for the automatic algorithm has been reached and the identification is stopped. If not, the identification continues as discussed in the following step.

Whilst θ_{error} is higher than the selected θ_{max} phase error tolerance for at least one frequency value under analysis, the order is to be increased by two, $N = N + 2$. Instead of restarting from scratch each time, the automatic algorithm allows the new initial poles to be defined as the final poles of the previous identification and two additional complex conjugate poles on the center of the frequency band.

Finally, in order to avoid infinite loops or excessively long identifications, the maximum identification order is set to $N_{stop} = 10N_{initial}$. In other words, if the phase error tolerance is not met for any even order N between $N_{initial}$ and N_{stop}, the identification is halted, the results for order N_{stop} are displayed and a warning message is produced. In these cases, reducing the frequency range under analysis or increasing the phase tolerance is advised.

A flow diagram that summarizes the created automatic identification algorithm is shown in Figure 2.4.

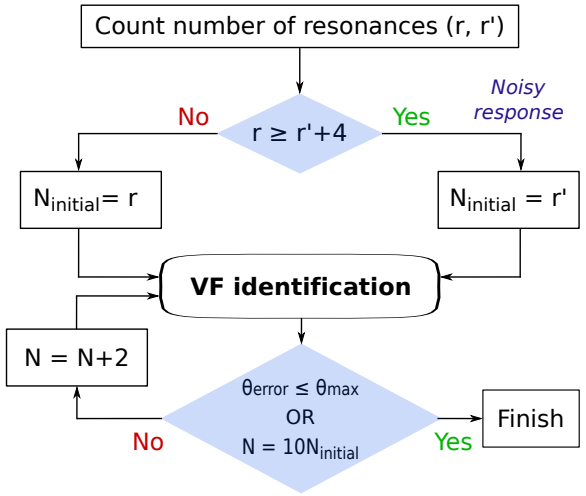

Figure 2.4: Diagram of the automatic order selection algorithm with Vector Fitting.

As a final note, the recommended default value of θ_{max} for a precise identification has been set to $\theta_{max} = 0.5°$ for the MM_stab pole-zero identification tool.

2.3.2 Plotting of Resonant Poles

A novel representation of the identified pole-zero map, or pole map in MIMO identifications, based on the analysis of their damping factor is proposed to minimize the visualization of mathematical poles caused by overmodeling and to improve the interpretation of the identification results.

First off, multiple second-order transfer functions have been defined from complex conjugate poles with different damping factors. As illustrated in the Bode diagram in Figure 2.5, the resonance peak in the frequency domain is greater for the second-order transfer functions with low damping poles, where the damping ratio for a pole ($p_i = a + jb$) is defined as follows:

$$\delta = \frac{-a}{\sqrt{a^2 + b^2}} \tag{2.10}$$

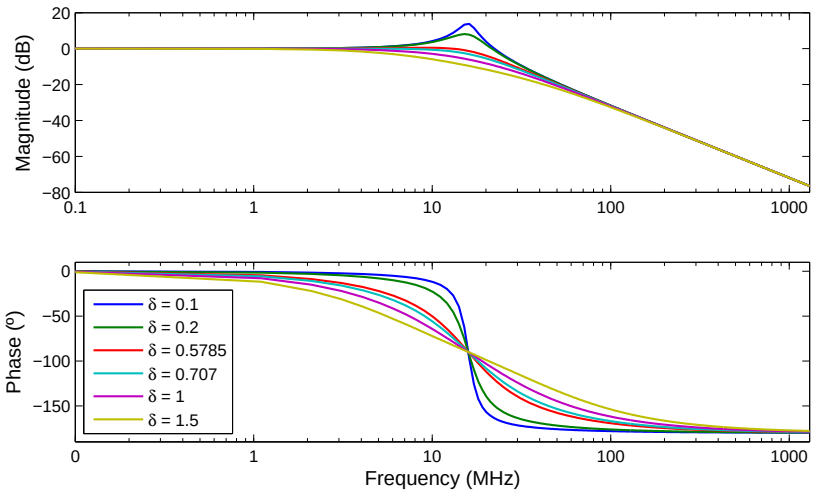

Figure 2.5: Bode plots of second-order transfer functions that illustrate the damping effect on the resonance.

The identified non-resonant poles do not model the critical dynamics and therefore are not indicators of unwanted oscillations. Contrarily, actual physical poles that will become unstable will be highly resonant as a critical parameter of the system under analysis is varied.

Thus, taking into account that the resonance peak in the frequency domain is greater for poles with low damping, by calculating the damping ratio of all the poles, the poles with more influence on the critical dynamics of the system can be determined.

Although damping ratios below 0.707 ensure mathematical resonance peaks, the magnitude peaks for poles with $\delta \approx 0.707$ and large real parts (a) are close to null. Therefore, instead of considering all the identified resonant poles, this novel representation proposes the consideration of resonant poles ($p_i = a + jb$) with magnitude peaks greater than 0.5 dB or equivalently, $\delta < 0.5785$:

$$mag(H)_{\omega=\omega_r} = 20 \log \left(\frac{\omega_n^2}{2ab} \right) > 0.5 \ dB \tag{2.11}$$

where the natural frequency (ω_n) and the resonant frequency (ω_r) of pole $p_i = a + jb$ are defined as follows:

$$\omega_n = \sqrt{a^2 + b^2} \tag{2.12}$$

$$\omega_r = \sqrt{b^2 - a^2} \tag{2.13}$$

Additionally, since the fitting is carried out on a fixed frequency band and the identified transfer function is not limited to it, the poles whose resonance peak is not on the frequency band under analysis should be discarded. That is, only the poles with resonant frequencies ω_r that meet the condition in (2.14) are to be considered, at least for the default visualization mode,

$$\omega_{min} \leqslant \omega_r \leqslant \omega_{max} \tag{2.14}$$

where ω_{min} is the lower limit frequency of the frequency band under analysis and ω_{max} is the upper limit of the frequency band under analysis.

The mentioned two conditions in (2.11) and (2.14) create the area on the s plane shown in Figure 2.6a.

On the other hand, the conventional area used by the STAN tool [62] only considers whether the imaginary part of the identified poles is within the frequency band under analysis (Figure 2.6b).

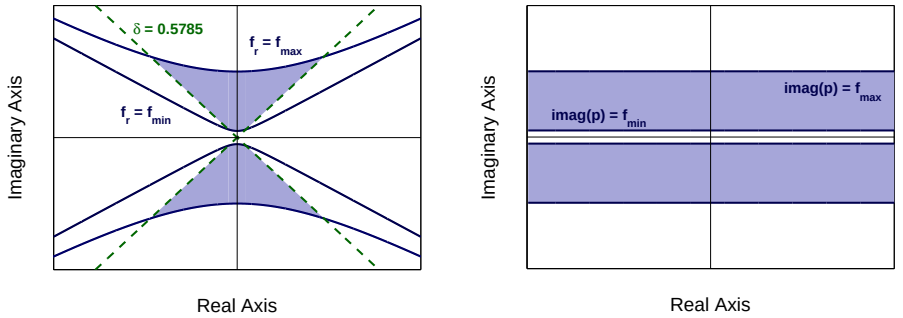

(a) (b)

Figure 2.6: Illustration of (a) the area of resonant poles with magnitude peaks greater than 0.5 dB and resonant frequencies within the frequency band under analysis (b) the conventional area considered by STAN.

In order to visualize the benefits of considering the horn-shaped area, the Bode diagrams of two second-order transfer functions, H_1 and H_2, are analyzed (Figure 2.7).

H_1 consists of a second-order transfer function constructed with a pair of stable non-resonant complex conjugate poles. As is expected,

no resonance peak or phase-jump is appreciated in the blue curves in Figure 2.7. Moreover, the magnitude and phase curves of H_1 resemble those of a real pole.

H_2 consists of a second-order transfer function constructed with a pair of stable resonant complex conjugate poles. Since the resonant frequency of the poles of H_2 is in the frequency band under analysis a magnitude peak can be appreciated in the green curves in Figure 2.7.

The conventional frequency area considered by STAN would discard the resonant poles of H_2 and plot the non-resonant poles of H_1. Instead, if the horn-shaped area is considered, the non-resonant poles will not be plotted and the possibly critical resonant poles will be plotted.

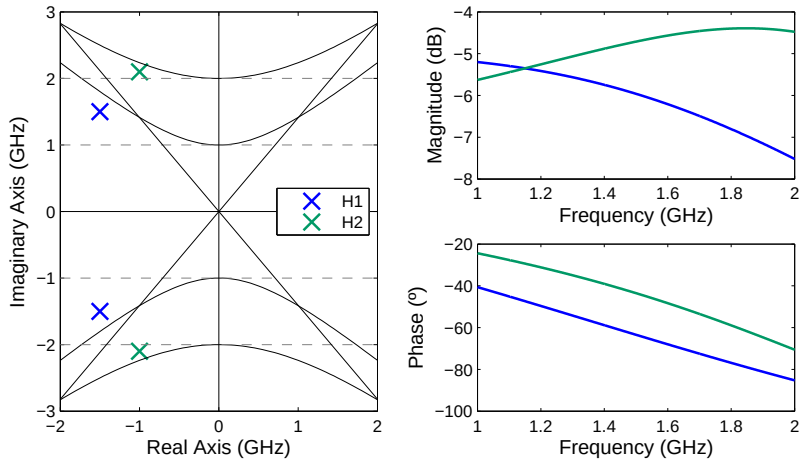

Figure 2.7: Pole-zero map, magnitude and phase plots of two second-order transfer functions, H_1 (blue) and H_2 (green) that serve to illustrate the benefits of the horn-shaped area of resonant poles.

However, it should be noted that both tools also include the option of plotting all of the poles of the fitted transfer function, instead of plotting only the poles on the areas discussed in Figure 2.6.

2.4 Residue Analysis

A technique based on residue analysis of MIMO frequency responses identified with a unique set of poles has been developed to detect the origin of instabilities and to detect mathematical pole-zero quasi-compensations that may appear due to overmodeling.

We depart from a set of M frequency responses $\boldsymbol{H(j\omega)}$ (2.15) that correspond to different input/output representations of a linear (or linearized) system. A MIMO pole-zero identification is carried out to obtain the $\boldsymbol{H(s)}$ transfer functions. It should be noted that, as a result of the MIMO pole-zero identification, all the transfer functions in $\boldsymbol{H(s)}$ share the same set of p_k poles.

$$\boldsymbol{H(s)} = [H^1(s), ..., H^M(s)] \tag{2.15}$$

For the residue analysis, we now focus on a single transfer function $H^i(s)$ of $\boldsymbol{H(s)}$ (2.16), granted that $i = [1, ..., M]$. The representation in (2.16) is a summation of fractions and the residue $r_{i,k}$ provides quantitative information on the contribution of the p_k pole to the transfer function $H^i(s)$.

$$H^i(s) = \sum_{k=1}^{N} \frac{r_{i,k}}{s - p_k} + D_i \tag{2.16}$$

Whilst all the $H^i(s)$ transfer functions in $\boldsymbol{H(s)}$ share the same set of p_k poles, the $r_{i,k}$ residues associated to each p_k pole will vary from one transfer function to another. In particular, the residues obtained at sensitive locations will be large. On the contrary, poles that are quasi-compensated by zeros in a polynomial ratio representation of $H^i(s)$, will have very small residues when $H^i(s)$ is expressed as a summation of partial fractions.

However, a simple comparison of residues in absolute terms is not appropriate. The $H^i(s)$ transfer functions can be impedance and/or admittance transfer functions calculated at different circuit nodes and/or branches. Thus, their absolute value can vary by several orders of magnitude from one $H^i(s)$ to another, and within a same $H^i(s)$ in broadband identifications. These differences in magnitude are also reflected in the value of the residues, making the comparison in absolute terms impractical. For a meaningful comparative analysis, the relative effect that the critical poles have on each $H^i(s)$ must be calculated and quantified.

Common instabilities encountered in microwave amplifiers are associated to unstable pairs of complex conjugated poles that are resonant. Consequently, let us consider a pair of resonant unstable complex conjugate poles p_k, p_k^*. Their contribution to $H^i(s)$ is given by (2.17).

$$H^{i,k}(s) = \frac{r_{i,k}}{s - p_k} + \frac{r_{i,k}^*}{s - p_k^*} \tag{2.17}$$

This contribution has a maximum in magnitude at the resonant frequency ω_r (2.13) that depends on the values of p_k and $r_{i,k}$ (2.18).

$$max\left(\left|H^{i,k}(j\omega)\right|\right) = \left|H^{i,k}(j\omega_r)\right| \tag{2.18}$$

The maximum contribution is then weighted by the contribution of the rest of the summation terms in $H^i(s)$ at ω_r in order to get the normalized factor $\rho_{i,k}$.

$$\rho_{i,k} = \frac{\left|H^{i,k}(j\omega_r)\right|}{\left|H^i(j\omega_r)\right| - \left|H^{i,k}(j\omega_r)\right|} \tag{2.19}$$

This normalized factor quantifies the relative effect of the pair of resonant complex conjugate poles p_k, p_k^* on transfer function $H^i(s)$.

Analyzing the value of $\rho_{i,k}$ corresponding to different $H^i(s)$ transfer functions obtained at multiple circuit locations, one can quantify the locations of the circuit with high observability and controllability for any given pair of complex conjugate poles p_k, p_k^*.

2.4.1 Detection of the Origin of the Critical Dynamics

Stabilization elements or networks included at some amplifier stages may not contribute to improve stability unless they are introduced within the feedback loop responsible for the oscillation. Thus, it is important to determine where in the circuit (in which stage) the oscillation is being generated in order to stabilize it efficiently.

In order to do so, multiple frequency responses $\boldsymbol{H(j\omega)}$ must be obtained at different observation ports of the amplifier and a MIMO pole-zero stability analysis is to be carried out. As mentioned previously, for a systematic MIMO pole-zero stability analysis and to minimize the chances of missing the detection of unstable behaviour, the gate (or base) and drain (or collector) nodes or branches of at least one of the transistors of each stage of the amplifier should be analyzed.

The location of the inner loop responsible of the critical resonance is determined from the $\rho_{i,k}$ factors associated to the critical poles p_k of each transfer function in $\boldsymbol{H(s)}$ (2.15). The highest $\rho_{i,k}$ factor indicates that the observation port at which the $H^i(s)$ transfer function has been obtained is closest to the origin of the critical dynamics.

A specific prototype has been designed in microstrip technology to illustrate the proposed methodology. It is a three stage amplifier based on GaAs FET transistor (FLU17XM) delivering 33 dBm with a gain of 38 dB at 1.2 GHz. A photograph of the fabricated prototype is shown in Figure 2.8.

The amplifier presents two common instabilities, an oscillation at 3.5 GHz when biased at nominal conditions and a low frequency oscillation for input powers greater than $P_{in} > -9$ dBm.

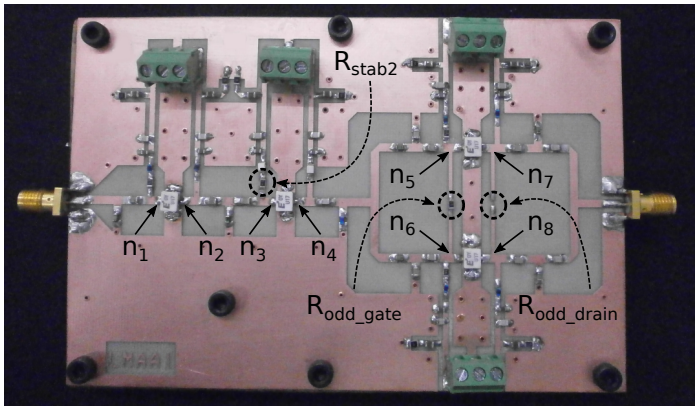

Figure 2.8: Photograph of the three stage L-band amplifier. Eight observation ports $n_1, ..., n_8$ are defined for the small-signal and large-signal MIMO stability assessment. The R_{odd_gate}, R_{odd_drain} resistors used to stabilize the oscillation at 3.5 GHz and the R_{stab2} resistor used to stabilize the large-signal instability are also highlighted.

Firstly, the amplifier showed an oscillation at 3.5 GHz when biased at its nominal condition (Figure 2.9).

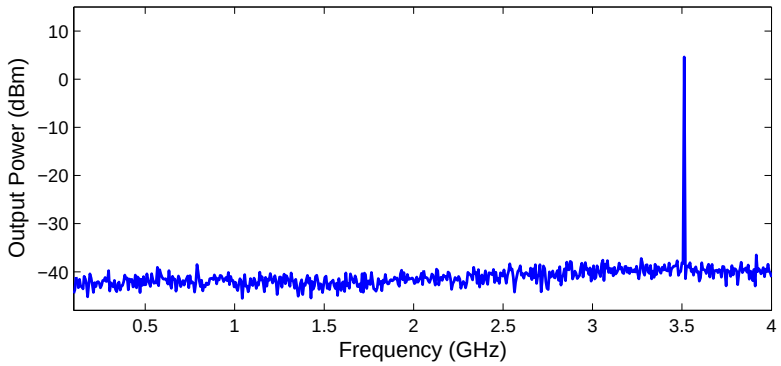

Figure 2.9: Measured output power spectrum showing an oscillation at 3.5 GHz when biased at nominal conditions.

To determine the critical nodes of the amplifier, a single MIMO

pole-zero stability analysis can be carried out. For the MIMO analysis eight observation nodes (labeled n_1 to n_8 in Figure 2.8) are considered, corresponding to gate and drain terminals of the four transistors. The impedances seen by small-signal current sources sequentially connected at the eight nodes, are simulated. Individual excitations of odd and even modes are applied to the third stage due to its power combining structure (Figure 2.10) [91]. For the even mode, two in-phase current sources must be simultaneously applied to nodes n_5 and n_6 (same for nodes n_7 and n_8), as in Figure 2.10a. For the odd mode, two 180° out-of-phase current sources must be simultaneously applied to nodes n_5 and n_6 (same for nodes n_7 and n_8), as in Figure 2.10b.

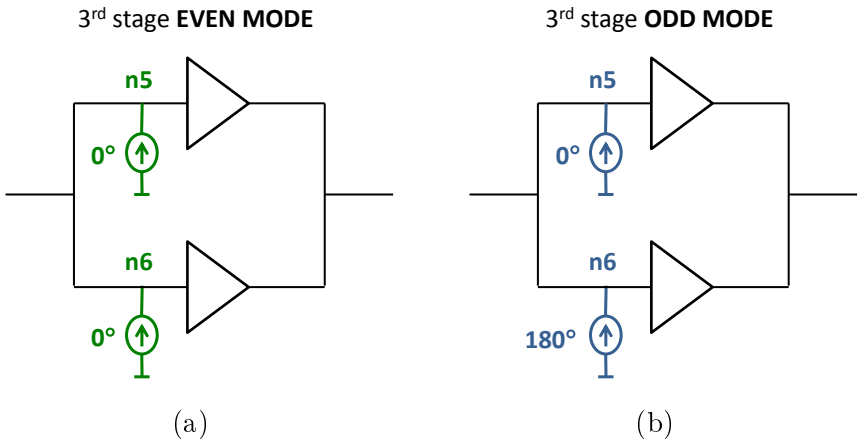

Figure 2.10: Illustration of the introduction of odd and even mode excitations between the gates of the transistors of the third stage of the amplifier in Figure 2.8. (a) Two in-phase current sources must be introduced simultaneously to obtain the even-mode frequency responses. (b) Two out-of-phase current sources must be introduced simultaneously to obtain the odd-mode frequency responses.

As a result, a total of eight frequency responses (Figure 2.11) are identified with the MIMO pole-zero identification tool, fixing a common denominator to the multiple transfer functions. The obtained poles are plotted on the complex plane in Figure 2.12, where a pair of

unstable complex conjugate poles are clearly detected at 3.3 GHz. The detection of the pair of unstable complex conjugate poles at 3.3 GHz is in concordance with the oscillation measured at 3.5 GHz shown in Figure 2.9.

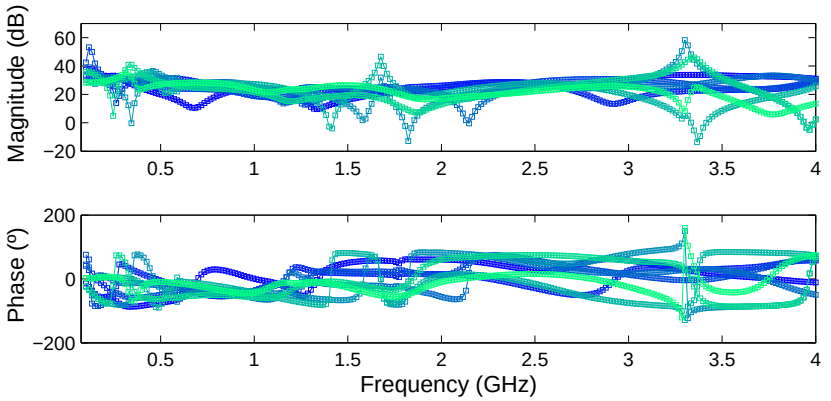

Figure 2.11: Magnitude and phase curves of eight impedance type frequency responses obtained for nominal bias conditions.

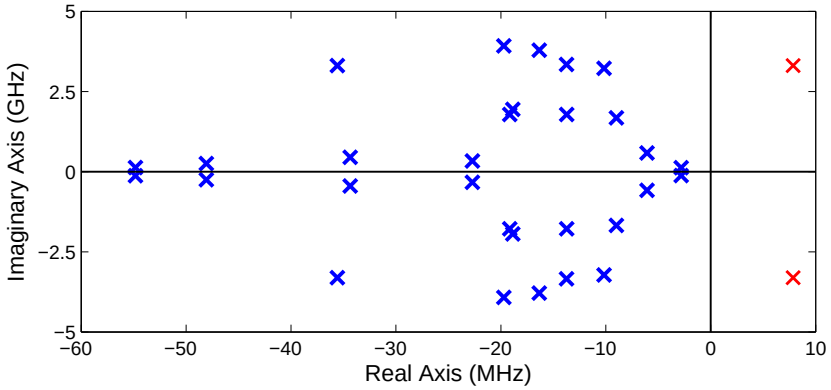

Figure 2.12: Poles of the amplifier biased at nominal conditions.

Next, the residue analysis is applied to determine the origin and nature of the oscillation. Using (2.19), the ρ factor associated to the unstable pair of complex conjugate poles at 3.3 GHz can be computed for the previously defined eight frequency responses (Figure

2.13). From the quantitative results in Figure 2.13 we can clearly deduce that the oscillation takes place in the third stage and that it is an odd mode oscillation because its corresponding ρ factor is larger by several orders of magnitude.

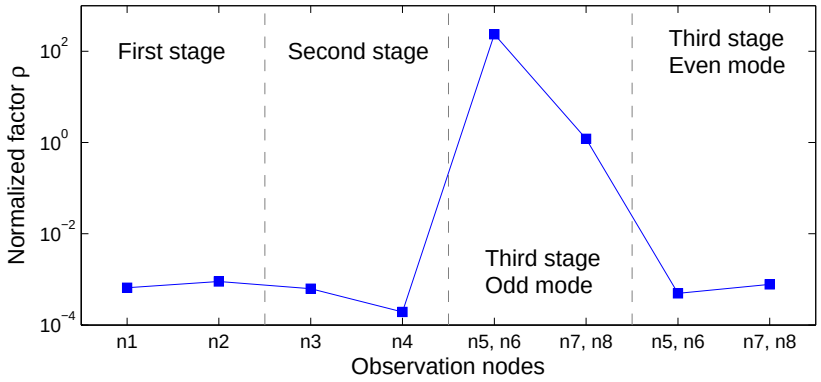

Figure 2.13: The residue analysis of the unstable poles at 3.3 GHz indicates that the instability is an odd-mode oscillation at the third stage.

Odd-mode oscillations can be eliminated with a proper selection of parallel resistors between the gates $\left(R_{odd\_gate}\right)$ and/or between the drains $\left(R_{odd\_drain}\right)$ of the transistors, in the third stage for this amplifier. Note that the value of ρ at the input of the third stage transistors (nodes n_5 and n_6) is appreciably larger than at the output (nodes n_7 and n_8). This indicates that the optimum location for circuit stabilization is between the gates of transistors of the third stage.

Indeed, as can be seen in Figure 2.14 a higher resistor value at the gates of the transistors of the third stage ($R_{odd\_gate} = 18\ k\Omega$) is sufficient to stabilize the circuit. Whilst a considerably lower resistor would have to be introduced between the drains of the amplifier to stabilize it, $R_{odd\_gate} = 1\ k\Omega$.

The simulated results in Figure 2.14 have also been experimentally confirmed since the circuit is stable with $R_{odd\_gate} = 5.1\ k\Omega$ while a

much smaller resistor value of R_{odd_drain} is needed to eliminate the oscillation ($R_{odd\_drain} = 910\ \Omega$). It should be noted that higher R_{odd_gate} and R_{odd_drain} resistor values can be used to stabilize the circuit, however, in practice, smaller values are often selected to guarantee higher stability margins.

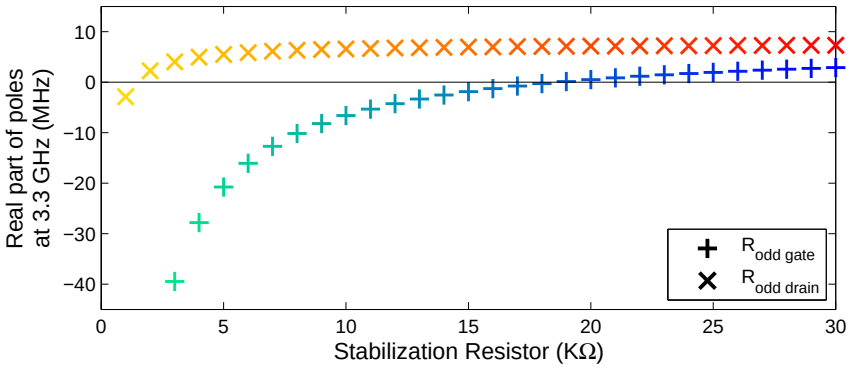

Figure 2.14: Evolution of real part of the critical poles at 3.3 GHz for the variation of a R_{odd_gate} resistor introduced between the gates of the transistors of the third stage (+) and a R_{odd_drain} resistor introduced between the drains of the transistors of the third stage (x).

Finally, a stabilization resistor of $R_{odd\_gate} = 5.1\ k\Omega$ was selected as the optimal stabilization network to eliminate the mentioned oscillation at 3.5 GHz.

Secondly, and once the DC steady state was stabilized, the amplifier presented a second oscillation that was function of the input power P_{in} for an operating frequency of $f_{in} = 1.2\ GHz$. For $P_{in} > -9\ dBm$, an oscillation at about 130 MHz was measured (Figure 2.15).

In order to determine the possible origin of this instability, a large-signal MIMO stability analysis is carried out. This is achieved by applying the input drive P_{in} to the circuit at $f_{in} = 1.2\ GHz$, introducing a small-signal current source sequentially to the previously mentioned eight observation ports and carrying out a mixer-mode harmonic balance simulation.

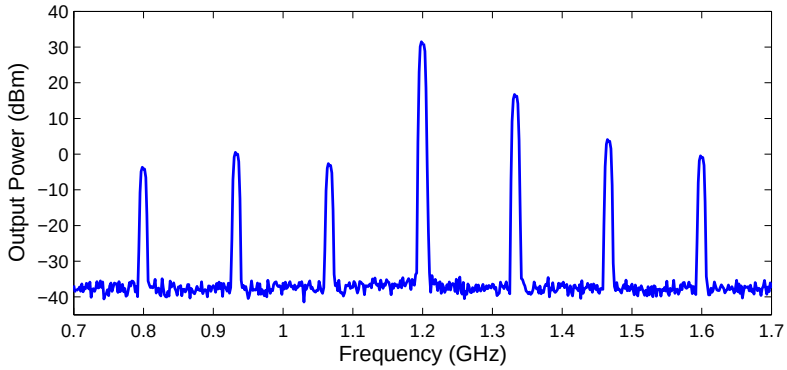

Figure 2.15: Measured output power spectrum showing the mixing terms around $f_{in} = 1.2\ GHz$ for $P_{in} = -5\ dBm$ due to parametric low frequency oscillation.

From identifying the eight frequency responses obtained via the harmonic balance simulation for $P_{in} = -5\ dBm$ (Figure 2.16), a pair of unstable complex conjugate poles at around 123 MHz is detected as shown in Figure 2.17. The detection of the pair of unstable complex conjugate poles at 123 MHz is in concordance with the oscillation measured at 130 MHz shown in Figure 2.15.

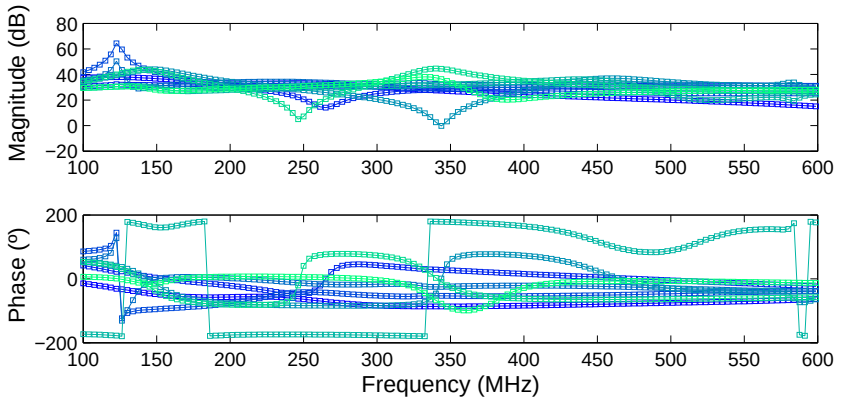

Figure 2.16: Magnitude and phase curves of eight impedance type frequency responses obtained for $P_{in} = -5\ dBm$.

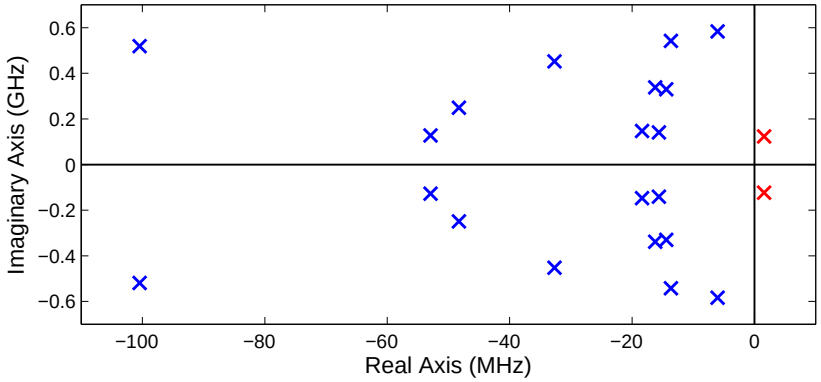

Figure 2.17: Poles of the amplifier for $P_{in} = -5\ dBm$.

In order to determine the input power (P_{in}) values for which the critical poles at 123 MHz becomes unstable, a parametric MIMO pole-zero stability analysis can be carried out varying P_{in}. It is determined that, the pair of complex conjugate poles at 123 MHz becomes unstable for $-7.4\ dBm < P_{in} < -3.6\ dBm$ in simulation, as show in Figure 2.17, where the real part of the identified critical poles is traced in a solid blue line.

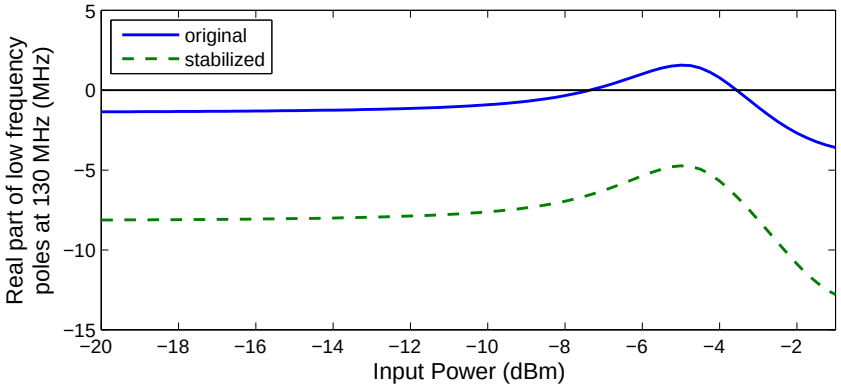

Figure 2.18: Evolution versus P_{in} of the real part of the low frequency (123 MHz) critical poles for the original and stabilized circuits.

Again, the residue analysis is applied to the identified unstable pair of complex conjugate poles at 123 MHz, to determine which stage is responsible for the oscillation measured at 130 MHz. In Figure 2.19 we observe that the ρ factor is larger by orders of magnitude in the second stage. This quantitative result clearly indicates that the oscillation takes place in the second stage. This information can then be used to guide the strategy for the stabilization of the amplifier.

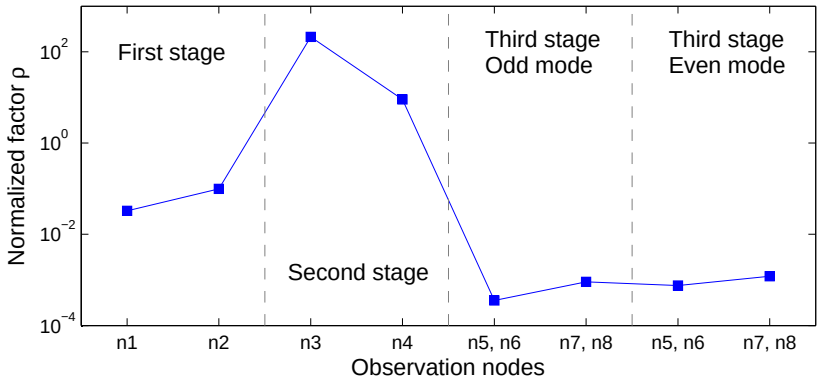

Figure 2.19: The residue analysis of the unstable poles at 130 MHz indicates that the instability is at the second stage.

Given that the frequency of the oscillation is low, it can be eliminated by increasing the value of the R_{stab2} stabilization resistor located in the second stage and highlighted in Figure 2.8 from its original value of 6 Ω to 24 Ω.

The evolution of the real part of the critical poles versus P_{in} for the stabilized amplifier ($R_{stab2} = 24\ \Omega$) is plotted with a dashed green line in Figure 2.18. The real part of the critical poles remains negative for all the tested P_{in} values, which indicates that the inclusion of a stabilization resistor of $R_{stab2} = 24\ \Omega$ correctly stabilizes the circuit. Additionally, and in full consistency with the results in Figure 2.19, stabilization of the amplifier is not possible acting upon bias networks of the first and third stages.

Finally, the stable performance of the amplifier was experimentally confirmed, as can be verified from the measured output spectrum for $P_{in} = -5\ dBm$ with $R_{odd\_gate} = 5.1\ k\Omega$ and $R_{stab2} = 24\ \Omega$ shown in Figure 2.20.

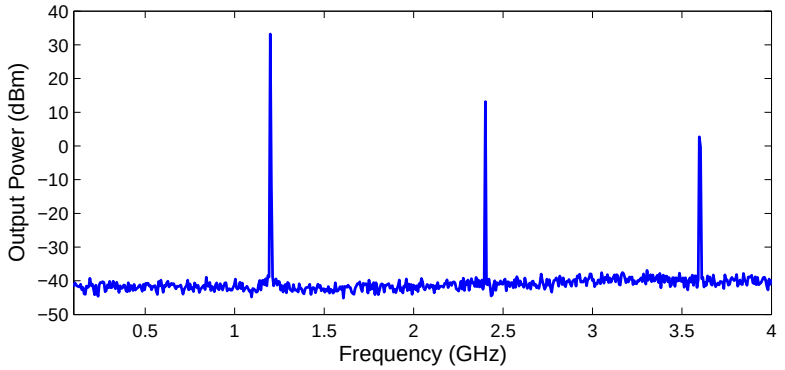

Figure 2.20: Measured output power spectrum showing stable operation for $P_{in} = -5\ dBm$ with $R_{odd\_gate} = 5.1\ k\Omega$ and $R_{stab2} = 24\ \Omega$.

2.4.2 Detection of Overmodeling

The computation of the ρ factor can also be applied to detect the adverse effects of overmodeling in the pole-zero fitting process [66].

If the pole-zero identification is carried out with an excessively strict optimization goal, Vector Fitting could end up fitting the numerical noise existing in the simulated frequency response. This can lead to the onset of pole-zero quasi-cancellations that are mathematical.

These mathematical pole-zero quasi-compensations will have extremely low values of ρ, no matter the circuit location at which the transfer function is obtained. On the contrary, poles representing the actual circuit dynamics will have significantly larger values of ρ for at least some of the nodes or branches of the circuit.

Therefore, we are able to discriminate numerical pole-zero quasi-cancellations by analyzing the values of the ρ factor corresponding to transfer functions obtained at different nodes or branches.

This overmodeling detection approach has been applied to a frequency response corresponding to the linearization of a stable DC solution of a multistage MMIC S-band power amplifier. The mentioned frequency response has been identified with an excessively low phase error tolerance, $\theta_{max} = 0.01°$, and the resulting pole-zero map is shown in Figure 2.21a. As a consequence of selecting an excessively low θ_{max}, a considerable amount of mathematical unstable pole-zero quasi-compensations are identified. This could erroneously lead to deducing that the analyzed DC steady state is unstable.

The efficiency of the approach for cleaning up the pole-zero map is demonstrated in Figure 2.21b. The elimination of poles with $\rho < 0.01$ results in the pole-zero map in Figure 2.21b where no unstable poles are detected. Unlike from Figure 2.21a, the stability of the analyzed DC steady state would be correctly determined from Figure 2.21b.

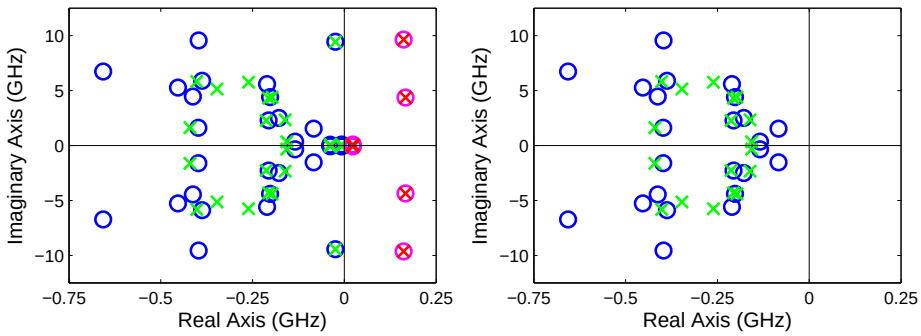

Figure 2.21: (a) The mathematical quasi-cancellations that model the numerical noise in the frequency response could lead to erroneously deducing that the analyzed DC steady state is unstable. (b) The quasi-cancellations that appear due to overmodeling are eliminated through an analysis of the ρ values, showing that the analyzed DC steady state is stable.

The ρ factor has also been introduced in the automatic algorithm described in section 2.3.1 to detect overmodeling and alert the user as described in the diagram in Figure 2.22.

The automatic order selection algorithm warns the user of the possible detection of overmodeling if the ρ factor of all the identified unstable poles is smaller than 0.01. If so, a warning message will appear encouraging the user to increase the phase tolerance introduced in the beginning. If a new and higher tolerance value is introduced, the automatic order selection algorithm will run only once more. Conceivably, the mathematical quasi-compensated poles will not be detected with the relaxed phase error condition.

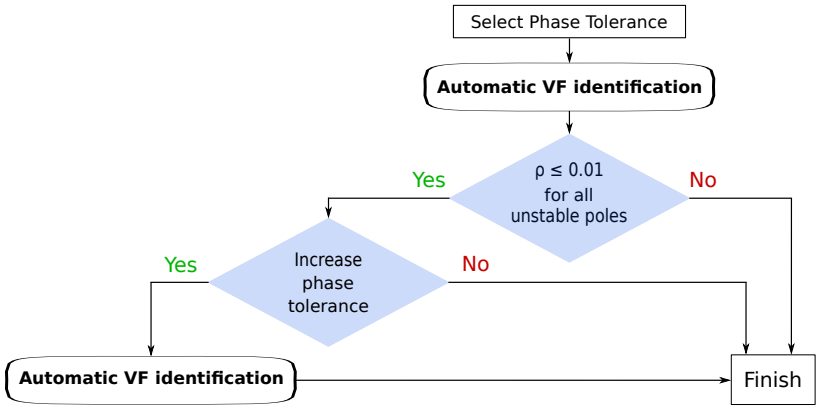

Figure 2.22: Diagram for the inclusion of the ρ factor to the automatic order selection algorithm with Vector Fitting for the detection of overmodeling.

In any case, as a final step, the ρ factor of all the identified unstable poles is calculated and displayed. The unstable poles are classified into two groups depending on their ρ factor.

On the one hand, the unstable poles with $\rho > 1$ are defined as

high sensitivity poles and their detection indicates that the circuit is unstable.

On the other hand, poles with $\rho < 1$ are defined as *low sensitivity* poles. A ρ factor below 1 indicates that the poles may be physical or numerical. If only *low sensitivity* unstable poles are detected, additional analyses must to be performed in order to determine (or not) the physical existence of the poles, such as, analyses at different nodes and branches or parametric analyses varying various parameters of the circuit. Finally, it should be noted that poles with very low sensitivity, $\rho < 0.01$, are very likely to be numerical.

In the case of MIMO identifications, the analyzed and displayed ρ factor for pole p_k will consist of the highest calculated $\rho_{i,k}$ for all the identified $H^i(s)$ transfer functions in $\boldsymbol{H(s)}$ (2.15).

2.5 Conclusions

In this chapter a new methodology and tool for stability analysis of microwave power amplifiers based on MIMO pole-zero identification has been introduced.

It has been demonstrated that identifying multiple frequency responses of the same circuit with the same set of poles gives way to many new strategies to reduce or avoid the main disadvantages of the commonly used SISO pole-zero stability analysis methodology.

The Vector Fitting algorithm has been introduced for the frequency domain identification of MIMO (and SISO) transfer functions mainly due to its capacity to fit multiple frequency responses with the same set of poles. However, it has also been demonstrated that the Vector Fitting identification algorithm is numerically better conditioned for microwave applications than the Least Squares algorithm because it avoids the calculus of the high valued powers of $j\omega$.

Additionally, the MIMO identification with Vector Fitting and, in particular, the representation as a summation of fractions has given way to the creation of a residue analysis strategy capable of detecting the location of the inner loops responsible of the critical or unstable dynamics. This tool can be extremely useful to determine optimal stabilization strategies of multistage amplifiers since, by analyzing the ρ factor, the critical stages of multistage amplifier can be determined. Indeed, the proposed residue analysis strategy has been applied to determine the location of the unstable feedback loops responsible of the instabilities detected in the small-signal and periodic large-signal regimes of the L-band three-stage amplifier prototype designed *ad hoc* for this thesis. This way, thanks to the information obtained with the residue analysis, the optimum stabilization strategies have been designed at the stages responsible of each oscillation.

Finally, new strategies to overcome overmodeling have been introduced to the newly created MIMO stability analysis tool. Firstly, an algorithm to automatically select the order of the fitted transfer function has been generated. Next, a new representation that consists of showing only resonant poles with noticeable magnitude peaks has been generated. Finally, it has been determined that by analyzing the ρ factor the mathematical quasi-compensations can be better detected and discarded.

3 Design of a Doherty Amplifier

3.1 Introduction

The power amplification of amplitude modulated RF signals is associated with the linearity-efficiency compromise [92], [93].

If the amplifier is used at the linear region, its efficiency will be far from the maximum attainable efficiency. Taking into account that for a class A amplifier the maximum efficiency at saturation is 50% and 78.5% for a class B amplifier, even lower efficiencies imply high running costs [94].

However, if the amplifier is used at its most efficient capacity, that is at the nonlinear region, the envelope of the input signal will be distorted and the transmitted information might be lost.

Many solutions were proposed to reduce running costs and improve thermal management, one of which is the efficiency enhancement technique based on active load modulation presented by Doherty in the year 1936 [95]. Other efficiency enhancement solutions include the out-phasing amplifier proposed by Chireix [96] and the envelope elimination and restoration (ERR) technique introduced by Kahn [97].

In this chapter, after a brief introduction of the classical Doherty amplifier functioning and a review of design alternatives to improve

linearity, back-off efficiency and bandwidth of Doherty amplifiers, the design of a X-band Doherty amplifier based on UMS GH25 GaN technology is described.

Special emphasis has been placed on guaranteeing the stability of the designed circuit all throughout the design process. This has been achieved thanks to the Multiple-Input Multiple-Output (MIMO) pole-zero identification stability analysis tool and the residue analysis strategy introduced in Chapter 2.

3.2 The Classical Doherty Configuration

The classical Doherty amplifier consists of two amplifying devices, carrier and peaking amplifiers, connected in parallel (Figure 3.1). By virtue of the output combiner configuration, the load impedance varies depending on the input power level. This technique is also known as active load-pull. Thanks to the active load-pull, higher efficiency values than with classical class B amplifiers can be achieved throughout the 6 dB output back-off (OBO) region (Figure 3.2).

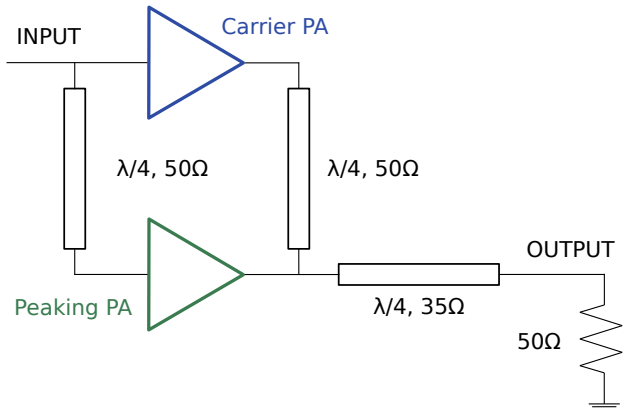

Figure 3.1: Diagram of the classical Doherty amplifier.

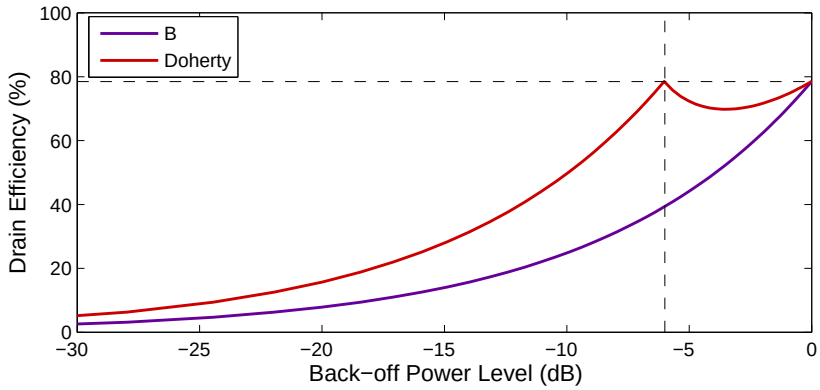

Figure 3.2: Theoretical drain efficiencies for a class B amplifier and a classical Doherty amplifier with class B carrier amplifier and class C peaking amplifier.

The main component required for the active load-pull technique is the impedance inverter $\lambda/4$ transmission line introduced at the output of the carrier amplifier. It must be noted that the effects of the phase inversion introduced by the impedance inverter at the output of the carrier amplifier are canceled via the inclusion of a delay line at the input of the peaking amplifier.

In the following paragraphs the overall functioning of the classical Doherty amplifier and the corresponding current, voltage and impedance curves (Figure 3.3) are briefly described.

At low input power, the peaking or auxiliary amplifier is cut-off and appears as an open circuit. This can be achieved, as discussed in [95], with a class C biasing of the peaking amplifier since the input signal is not sufficient to overcome the negative bias of the class C peaking amplifier. Therefore, for low input power values the carrier or main amplifier functions as a typical class B amplifier with a 100 Ω load, resulting from the two $\lambda/4$ lines connected at its output (Figure 3.1).

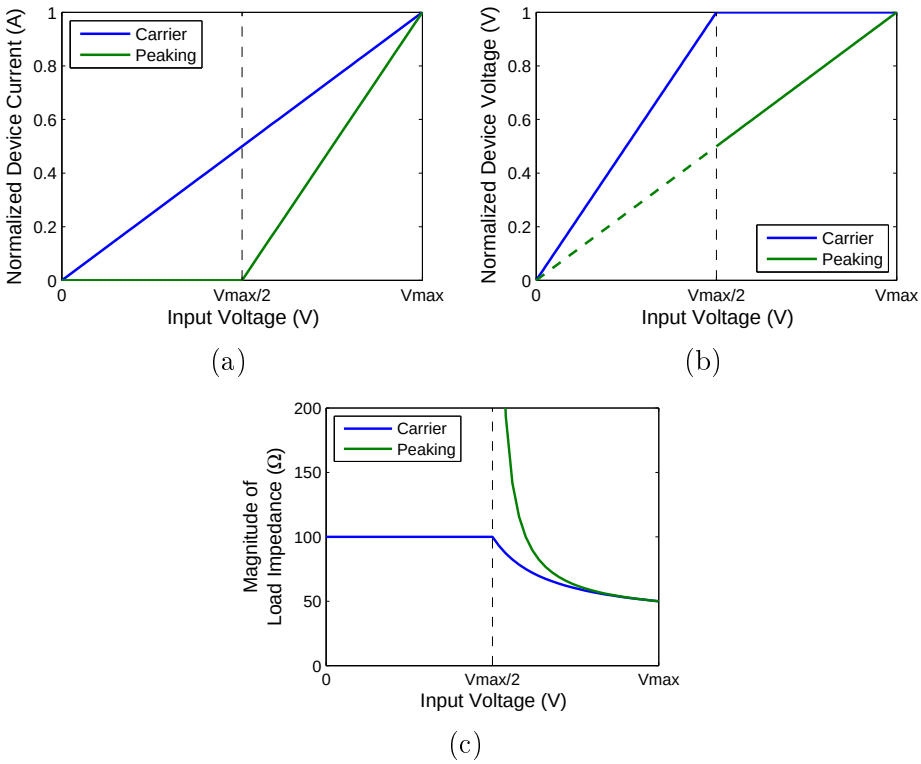

Figure 3.3: (a) Theoretical carrier and peaking currents versus input drive voltage. (b) Theoretical carrier and peaking voltages versus input drive voltage. (c) Theoretical load impedances versus input drive voltage.

Given that a load impedance of 100 Ω is applied to the carrier amplifier instead of the optimal 50 Ω load, the class B carrier amplifier becomes maximally efficient when the input drive is half the maximum input drive amplitude ($V_{max}/2$), or equivalently, at the 6 dB OBO point. The instantaneous efficiency at this point is therefore equal to the maximal efficiency of class B amplifiers, 78.5%.

The peaking amplifier becomes active at the 6 dB output back-off point and starts injecting current into the output common node. As a result of the current injection, two effects can be appreciated: the output power increases and the load seen by the carrier and peaking

amplifiers decreases.

Finally, at saturation, the carrier and peaking output matching networks present 50 Ω to both amplifiers and each amplifier delivers half of the system output.

3.3 Doherty Design Options

The classical Doherty approach assumes two identical devices, with different bias conditions, to work as carrier and peaking amplifiers. However, many alternatives to the classical Doherty configurations have been proposed since 1936, some of which appear summarized in [98],[99].

Biasing of the Peaking Amplifier

In the classical Doherty configuration the carrier or main amplifier is biased in class B whilst the peaking or auxiliary amplifier is biased in class C. This is the simplest method to ensure that the peaking amplifier will be in cut-off for low input powers.

Nonetheless other bias conditions can be considered depending on the power level and efficiency required in the back-off region. The higher the class (D, E, F, G, S), the higher the efficiency will be in the back-off region but at the cost of lower output powers and worse linearity.

Asymmetrical Doherty Configuration

The main drawback of class C peaking amplifiers is that a very deep class C bias is required for the device to remain in cut-off until the 6 dB output back-off point. Furthermore, perhaps the gain of such a deep class C amplifier might not be sufficient for a correct active-load pull [100]. Consequently, linearity and power performances might be degraded.

Commonly the size of the peaking transistor is increased [101]. This way the high peak current of the peaking device is sufficient for a correct active load-pull. This solution is known as the extended Doherty configuration, the only drawback of this configuration is that two different output matching networks must be designed for the carrier and peaking amplifiers, which implies a more demanding design.

Asymmetrical Power Drive

Uneven power drive is a more typical alternative (or complement) to asymmetrical Doherty configuration since it can also lead to the optimal active load-impedance and there is no need of designing two different load charges [101]–[105].

In [106] two Doherty amplifiers designed with the same transistor size are presented, one of them has a symmetrical power drive and the other one has an asymmetrical power drive. A flatter efficiency curve throughout a larger output back-off range is obtained with the asymmetrical power drive.

Additional Offset Lines

Additional offset lines are often inserted in the outputs of the carrier and peaking amplifiers (Figure 3.4) to improve performance at lower input powers and to optimize the load modulation [107]–[109].

With the intent of not affecting the behavior of the Doherty amplifier at saturation, the characteristic impedance of the offset lines is chosen equal to the output load at saturation (50 Ω).

The length of the offset line behind the carrier amplifier is tuned to provide a purely real 100 Ω load at the device drain, a condition not generally satisfied with a simple matching network.

The length of the offset line behind the peaking amplifier is set to ensure that when turned off, the peaking amplifier does not influence

the load seen by the carrier amplifier. That is, to ensure that for small input powers the output of the peaking amplifier presents an open circuit to the carrier amplifier.

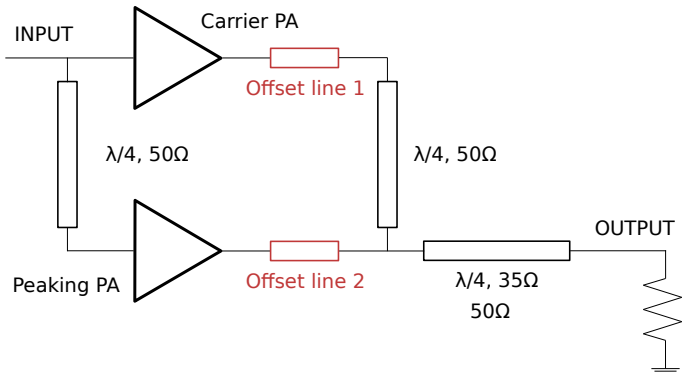

Figure 3.4: Diagram of the classical Doherty amplifier with offset lines included to improve performance.

Multistage Doherty Amplifiers

The objective of adding additional amplifier stages to the classical two-stage Doherty configuration is creating a smoother efficiency characteristic throughout a larger range of output back-off power.

In [110],[111] the efficiencies of multistage Doherty amplifiers constructed with class AB carrier amplifiers and class C peaking amplifiers are discussed (Figure 3.5).

Other alternatives of multistage Doherty amplifiers include the connection in parallel of two Doherty amplifies: two class AB carrier amplifiers and two class C peaking amplifiers [108], or including a power amplifier before each one of the carrier and peaking amplifiers as in [112].

The main drawback of multistage Doherty amplifiers is the added circuit complexity and that the two-tone Third-Order Intermodulation

Distortion (IMD3) cancellations are more sensitive than in traditional two-stage Doherty amplifiers. Management of bias offsets and the design of valid power divider combiner networks are challenging tasks that, in reality, might not ensure the theoretical curves in Figure 3.5.

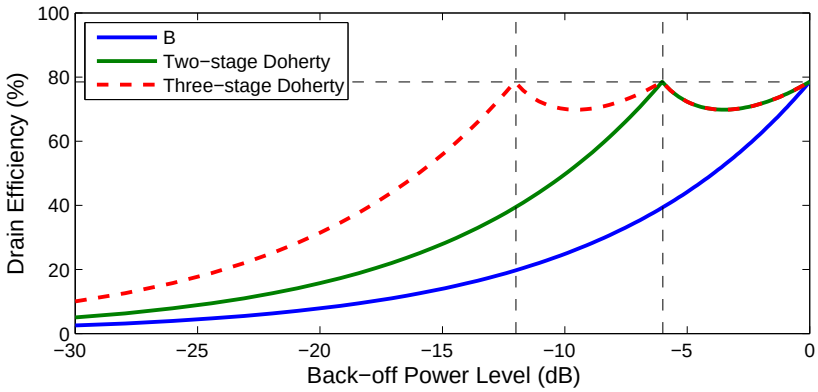

Figure 3.5: Efficiency curves of a class B amplifier, a two-stage Doherty amplifier and a three-stage Doherty amplifier.

Adaptative Bias

Another alternative to improve the efficiency and linearity of the Doherty amplifier is the variation of the peaking amplifiers bias depending on the input drive level.

For small input drive values, the peaking amplifier is biased as in a conventional Doherty amplifier. However, once the input drive reaches the 6 dB output back-off point the bias point of the peaking amplifier is shifted monotonically with the increasing RF drive level until the carrier and peaking amplifiers are biased at the same point (when the drive level reaches its maximum value).

It must be noted that the application of this technique implies a higher degree of complexity since it requires precise envelope detection.

Alternatives for Larger Bandwidths

The main reason behind the bandwidth limitation of Doherty amplifiers are the $\lambda/4$ impedance inverters tuned at the fundamental frequency f_0. Many solutions for increasing the bandwidth of Doherty amplifiers have been proposed [113]–[120].

The simplest solution is substituting the impedance inverting $\lambda/4$ transmission lines by equivalent networks with lumped components (LC tank, two-fold π networks, etc.). Moreover, the size of the final designs can also be reduced with the use of other equivalent circuits for cases where the $\lambda/4$ lines are too long.

In [115] a novel output combining network, constituted of four $\lambda/4$ transmission lines, is presented which allows the implementation of Doherty amplifiers with defined bandwidths without worsening its performance.

Final Design Decisions

Depending on the application requirements, different combinations of the previously mentioned alternatives can be chosen for the Doherty amplifier design.

In the following paragraphs the decisions made when designing the final Doherty amplifier are discussed. It must be noted that one of the main objectives for the design of this Doherty amplifier has been to correctly understand the functioning of the classical Doherty configuration introduced in 1936. Additionally, the design of the Doherty amplifier has been used as an opportunity to test the advantages of the MIMO stability analysis introduced in Chapter 2. Thus, the final design does not differ much from the classical configuration.

Two similar $8x150$ μm transistors of the UMS GH25 GaN technology have been selected as active devices. Employing two similar transistors is also known as the Doherty-Lite configuration [100] which allows a significant improvement in output back-off efficiency whilst

retaining a viable and simple circuit. However, the drain efficiency plot of Doherty-Lite amplifiers does not share the *twin peaks* of the drain efficiency curve of classical Doherty amplifiers.

The lange coupler [121] has been chosen for the symmetrical power division, mainly due to the 90° phase inversion it introduces to the peaking amplifier. This coupler multiplies the coupling between two adjacent microstrip lines by dividing each line longitudinally into two or more sections. Particularly the 6 fingered microstrip lange coupler, initially tuned at 10.95 GHz, has been designed (Figure 3.6). However the length has been later modified to tune the final results of the amplifier.

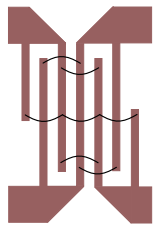

Figure 3.6: Geometry of lange coupler with 6 fingers.

The output combiner network has been designed following the design of the classical Doherty output combiner. That is, with a $\lambda/4$ transmission line and additional offset lines to improve efficiency at the output back-off and optimize the active load-pull. Therefore, no additional measures have been taken into account to achieve a high bandwidth.

To improve linearity without loosing much efficiency, a deep class AB bias has been chosen for the carrier amplifier instead of the classical class B bias.

Finally, a deep class C bias has been selected for the peaking amplifier. However, not as deep as in the classical Doherty amplifier since the peaking amplifier turns on before the 6 dB output back-off point.

Hence, a correct active load pull has been achieved at the central frequency of 10.95 GHz (Figure 3.7).

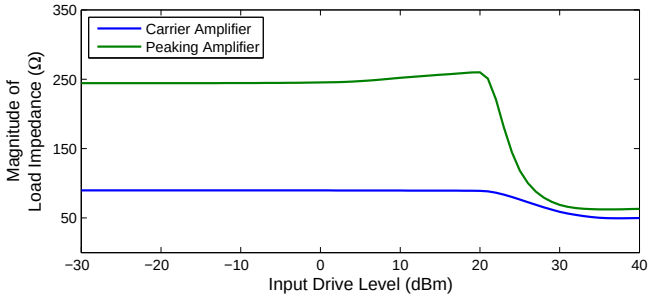

Figure 3.7: Simulated load impedances versus input drive of the final design at the fundamental frequency $f_0 = 10.95\ GHz$.

3.4 MIMO Pole-Zero Stability Analysis

Due to the multistage configuration of the Doherty amplifier, the MIMO pole-zero stability analysis introduced in Chapter 2 can be used to perform a systematic stability analysis of the circuit. In order to do so, four observation ports that consist of the gate and drain nodes of the carried and peaking amplifiers of the Doherty design are defined, as indicated in Figure 3.8.

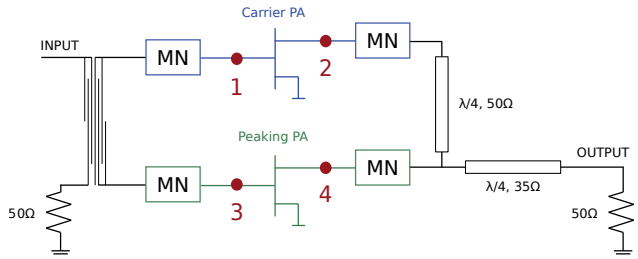

Figure 3.8: Four observation nodes are considered for the MIMO pole-zero stability analysis, corresponding to the gate and drain nodes of the transistors of the carrier and peaking amplifiers.

3.4.1 Small-Signal Analysis

As a first step, an AC simulation is carried out in Advanced Design System (ADS) [59] for the nominal bias conditions of the amplifier, $V_{G\_carrier} = -3.5\ V$, $V_{D\_carrier} = 25\ V$, $V_{G\_peak} = -4.95\ V$ and $V_{D\_peak} = 25\ V$. In order to obtain the closed-loop impedance responses for the systematic MIMO stability analysis, a small-signal current source is sequentially introduced to the previously mentioned four nodes. The simulated four frequency responses are plotted in Figure 3.9.

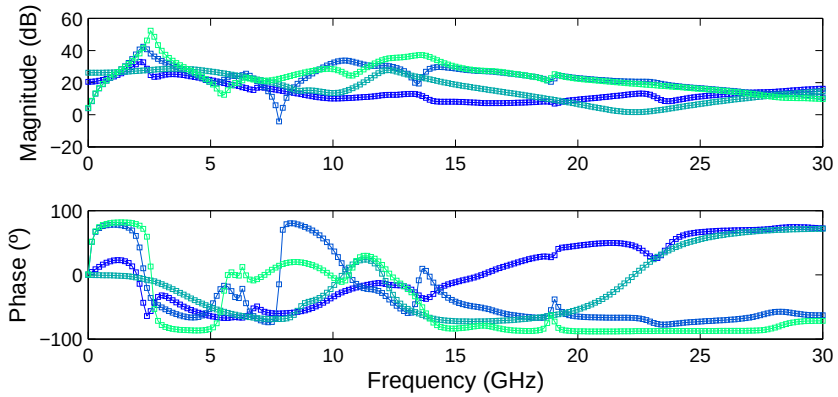

Figure 3.9: Magnitude and phase curves of four impedance type frequency responses obtained for nominal bias conditions.

Next, a small-signal MIMO identification of the frequency responses in Figure 3.9 is carried out and a pair of complex conjugate unstable poles is detected at 2.23 GHz as shown in Figure 3.10a.

Thanks to the created MIMO stability analysis tool that identifies multiple frequency responses with the same denominator, a residue analysis can be carried out to determine the location of the unstable feedback loop and to detect the optimum region for stabilization.

As can be determined from Figure 3.10b, the ρ factors associated to the nodes of the carrier amplifier are several orders of magnitude

higher that those associated to the nodes of the peaking amplifier. That is, the critical nodes for the identified unstable poles are the gate and drain observation ports of the carrier amplifier.

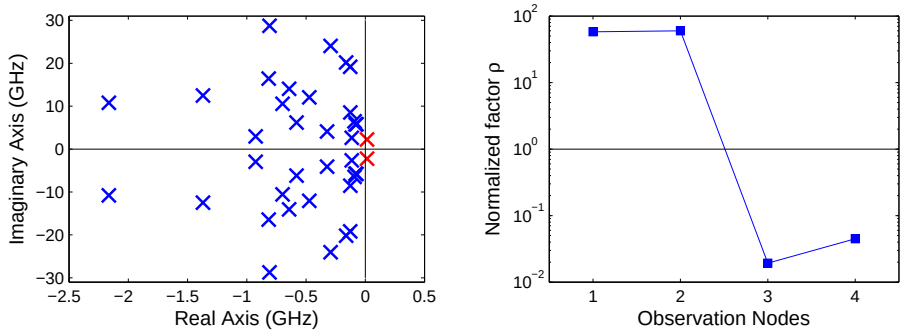

(a) (b)

Figure 3.10: (a) Poles of the amplifier biased at nominal conditions. (b) Residue analysis of unstable poles at 2.23 GHz indicating that the instability is at the carrier amplifier.

As a result, the bias paths of the carrier amplifier are selected for stabilization. Given that the oscillation is a low frequency oscillation, it can be eliminated by increasing the value of the $R_{stab\_carrier}$ resistor in the gate bias path of the carrier amplifier signaled in Figure 3.11a.

By applying the small-signal stabilization methodology introduced in Section 1.4, the $R_{stab\_carrier}$ resistor value required to stabilize the circuit can be determined. The effects of introducing a resistor in series at the mentioned branch can be predicted from introducing a small-signal voltage source in series at the mentioned branch and applying a root-locus analysis to the identified transfer function (proportional action). Indeed, it is determined that a minimum resistor of $R_{stab\_carrier} = 2\ \Omega$ is required for stabilization (Figure 3.11b).

An additional parametric analysis varying the value of $R_{stab\_carrier}$ has also been carried out in *ADS*, and as can be seen Figure 3.11b, the results obtained with the two methodologies correlate completely.

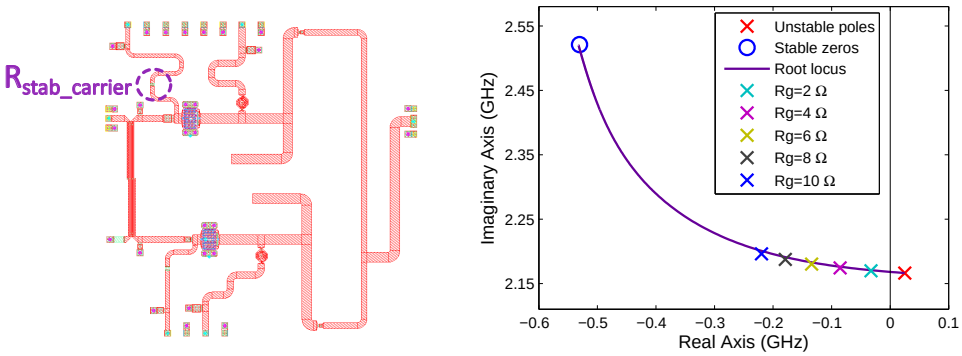

(a) (b)

Figure 3.11: (a) Layout of the final design signaling the gate resistor of the carrier amplifier. (b) Root loci for a voltage source introduced at the gate bias of the carrier amplifier. The unstable poles leave the right-hand side of the s plane for $R_{stab\_carrier} = 2\ \Omega$. Superimposed is the pole evolution resulting from a parametric stability analysis varying a stabilization resistor at the gate of the carrier amplifier (crosses).

Finally, to guarantee a higher stability margin, a resistor value of $R_{stab\_carrier} = 10\ \Omega$ has been chosen to stabilize the circuit. Lastly, it must be noted that the inclusion of this stabilization resistor does not affect the performance of the amplifier.

Once the instability present for nominal bias conditions has been stabilized, the small-signal stability of the amplifier versus variations of the bias conditions is analyzed.

No instability is detected for variations of the drain bias (from $0\ V$ to $25\ V$) or the gate bias (from $-6\ V$ to $0\ V$) of the carrier amplifier. However, an instability is detected when varying the gate bias of the peaking amplifier V_{G_peak} from $-3\ V$ to $-1\ V$ as shown in Figure 3.12.

In order to determine the origin of the identified unstable poles, a MIMO pole-zero analysis is carried out for a gate voltage bias of $V_{G\_peak} = -1\ V$. A pair of unstable complex conjugate poles are detected at $2.4\ GHz$ as shown in Figure 3.13a.

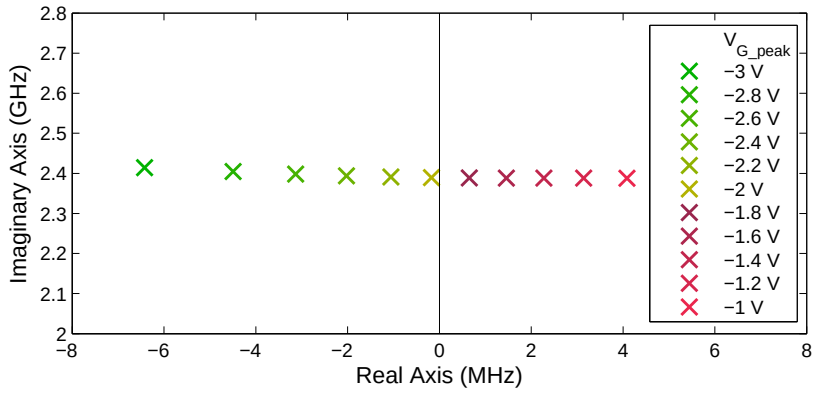

Figure 3.12: Poles resulting from a parametric stability analysis varying the gate voltage of the peaking amplifier V_{G_peak} from $-3\ V$ to $-1\ V$.

By carrying out the residue analysis introduced in Section 2.4 for the unstable poles identified at 2.4 GHz with the MIMO identification tool, the critical nodes can be determined.

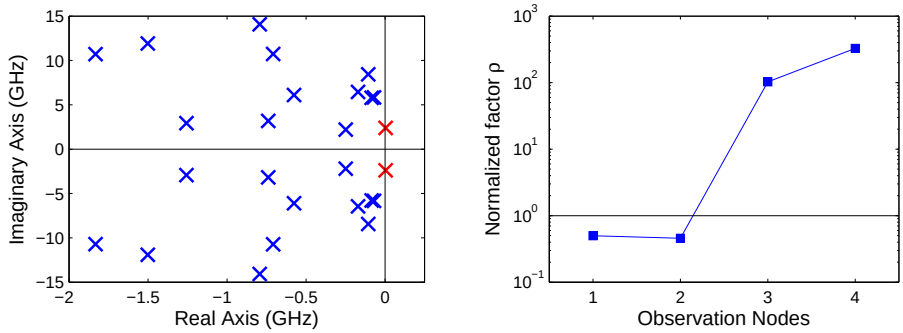

(a) (b)

Figure 3.13: (a) Poles of the amplifier biased at nominal conditions for the carrier amplifier and $V_{G\_peak} = -1\ V$. (b) Residue analysis of unstable poles at 2.4 GHz indicating that the instability is at the peaking amplifier.

As shown in Figure 3.13b, the ρ factors associated to the input and output nodes of the carrier amplifier are several orders of magnitude

lower than those associated to the nodes of the peaking amplifier. Therefore, from the analysis of the ρ factors it is concluded that the unstable feedback loop is at the peaking amplifier.

Due to the low frequency of the oscillation, the R_{stab_peak} resistor on the gate bias path of the peaking amplifier is selected for stabilization (Figure 3.14a).

Applying a root-locus analysis at the mentioned branch, it is determined that a stabilization resistor of $R_{stab\_peak} = 2\ \Omega$ is sufficient to stabilize the circuit, as shown in Figure 3.14b.

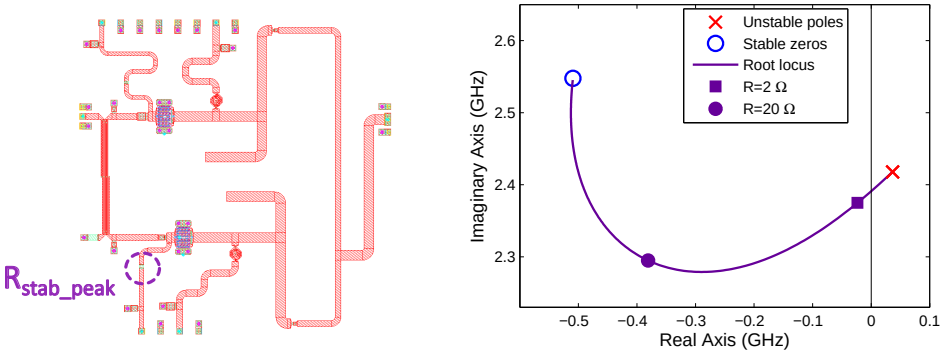

(a) (b)

Figure 3.14: (a) Layout of the final design signaling the gate resistor of the peaking amplifier. (b) Root loci for a voltage source introduced at the gate bias of the carrier amplifier. A stabilization resistor of $R_{stab} = 2\ \Omega$ is sufficient to stabilize the circuit. Superimposed is the pole resulting from introducing a 20 Ω at the gate of the peaking amplifier (dot).

However, a $R_{stab\_peak} = 20\ \Omega$ resistor has finally been selected to stabilize the circuit. Once more, it must be noted that the inclusion of this stabilization resistor does not affect the performance of the amplifier.

3.4.2 Large-Signal Analysis

After a thorough small-signal stability analysis, multiple large-signal stability analysis tests have been performed to guarantee the stability of the amplifier under large-signal excitations. The amplifier is stable for all the conducted tests, varying parameters such as input frequency, input power and bias.

Alarmingly, a pair of very resonant complex conjugate stable poles are also detected at the input frequency of $f_0 = 10.95\ GHz$, mainly for high input power values (Figure 3.15). Given that the detection of poles at f_0 often leads to the apparition of oscillations that can even destroy the amplifier [122], a thorough analysis around the fundamental frequency has been carried out. The obtained results and conclusions are summarized in the next section.

The most resonant poles resulting for a parametric MIMO stability analysis varying the input power are plotted in Figure 3.15. In addition to the mentioned very resonant poles at f_0, a couple of critical complex conjugate poles close to the Y axis are identified at 2.6 GHz and 6.3 GHz. However, the critical poles move towards the left-hand side of the s plane for increasing values of the input power.

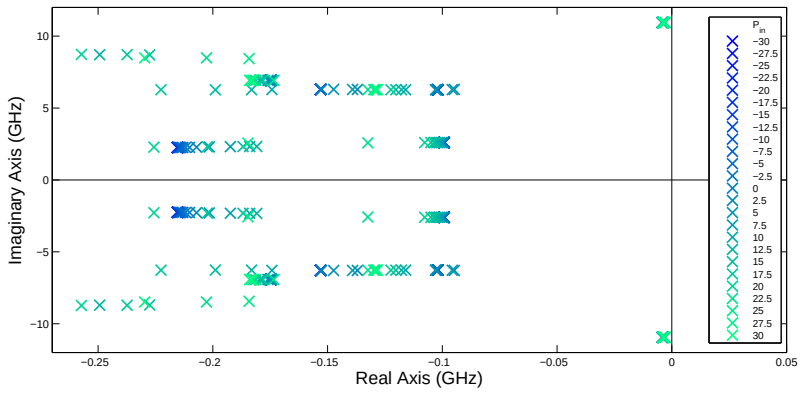

Figure 3.15: Poles resulting from a parametric stability analysis varying the gate voltage of the peaking amplifier.

Additional Monte Carlo analyses have also been carried out for input powers $P_{in} = 0\ dBm$ and $P_{in} = 29.8\ dBm$ varying the values of the components of the UMS library within their tolerance margins and no unstable poles are identified (Figure 3.16).

Firstly, a Monte Carlo analysis for input power $P_{in} = 0\ dBm$ has been carried out, because the most critical poles are closest to the Y axis for this input power value. As can be seen in Figure 3.16a no unstable poles are detected for the large-signal Single-Input Single-Output (SISO) Monte Carlo analysis carried out with 100 iterations.

Next, an equivalent Monte Carlo analysis is carried out for $P_{in} = 29.8\ dBm$, input power value for which the amplifier is saturated. Similarly, and as shown in Figure 3.16b, no unstable poles are detected. However, it should be noted that even if they are always stable, the set of very critical poles at f_0 are also detected in the second Monte Carlo analysis.

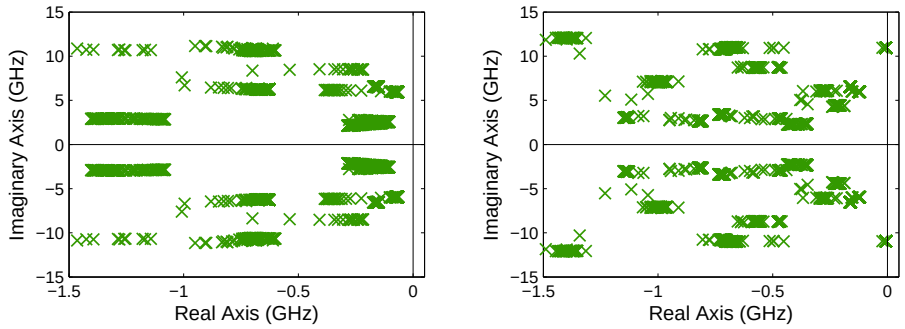

(a) (b)

Figure 3.16: Poles resulting from the large-signal Monte Carlo analysis with 100 iterations for input power (a) $P_{in} = 0\ dBm$. (b) $P_{in} = 29.8\ dBm$.

Thus, setting aside the critical poles at f_0 that are discussed at length in the following section 3.5, the stability of the final design has been ensured.

3.5 Resonant Poles at the Fundamental Frequency

As mentioned previously, mainly for high input power values, a pair of very resonant stable poles, quasi-compensated by zeros, have been detected at the input frequency of $f_0 = 10.95\ GHz$ (Figure 3.17a).

Due to their proximity to the Y axis and the possibility of them crossing to the unstable region of the s plane for variations of a parameter of the amplifier (for example, bias conditions or aging of the electronic components), these poles are considered, in principle, as critical poles. Consequently, a thorough analysis has been carried out to determine their origin.

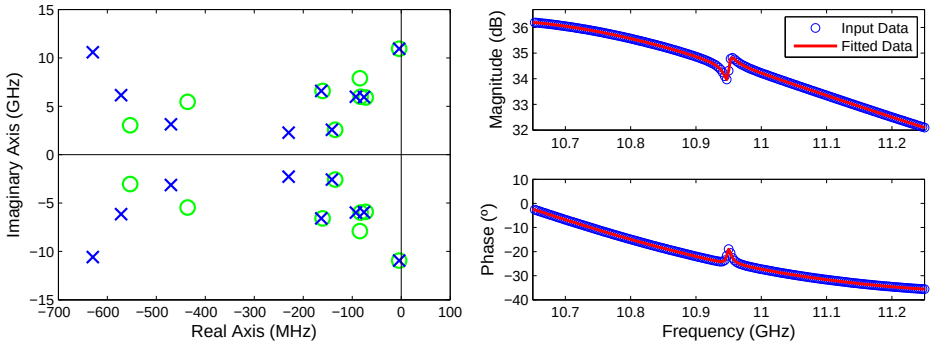

(a) (b)

Figure 3.17: Stability analysis of the amplifier for $P_{in} = 20\ dBm$, $f_0 = 10.95\ GHz$ and nominal bias conditions. (a) Pole-zero diagram where a critical stable pole-zero quasi-compensation is detected at $f_0 = 10.95\ GHz$. (b) Magnitude and phase curves where a small magnitude peak and phase jump is appreciated at $f_0 = 10.95\ GHz$.

A clear but small resonance peak is visible at the magnitude and phase curves obtained around $f_0 = 10.95\ GHz$ for the frequency response obtained by introducing a small-signal probe at the output of the carrier amplifier (Figure 3.17b). However, similar resonant peaks

are obtained for high input powers at different nodes of the amplifier. Therefore, it is concluded that the poles identified at f_0 are physical poles and not the results of overmodeling.

In order to identify the critical nodes or branches of the poles at f_0, a MIMO pole-zero stability analysis is carried out. Eight frequency responses are obtained by introducing small-signal current and voltage sources sequentially at the input and output observation ports of both transistors.

The poles at f_0 appear quasi-compensated by zeros for all the analyzed observation ports, or equivalently, all the calculated ρ factors for the poles at f_0 are below 1 as shown in Figure 3.18. Other additional observation ports have also been analyzed but similarly as for the previously identified frequency responses, none of them detect the poles at f_0 with high observability and controllability, i.e. with a high value of the ρ factor.

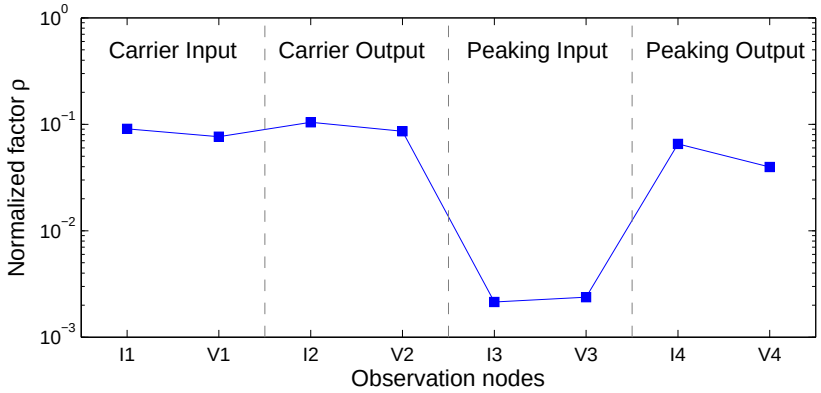

Figure 3.18: The residue analysis of stable poles at f_0 indicates that the poles are not detected clearly ($\rho > 1$) at any of the analyzed nodes.

To discard that the matching networks are the cause of the apparition of the poles at f_0, a simple cell consisting of a single transistor, ideal DC block capacitances, ideal DC feed inductances and 50 Ω source and load impedances is analyzed (Figure 3.19a).

The same stable quasi-compensated poles are detected at f_0 from the frequency response obtained by introducing a small-signal current source at the output node of the transistor of the simple cell and varying the input power P_{in} from 5 dBm to 15 dBm (Figure 3.19b). Therefore, it is concluded that the poles at f_0 are a result of the model of the transistor and not particular to the Doherty amplifier design.

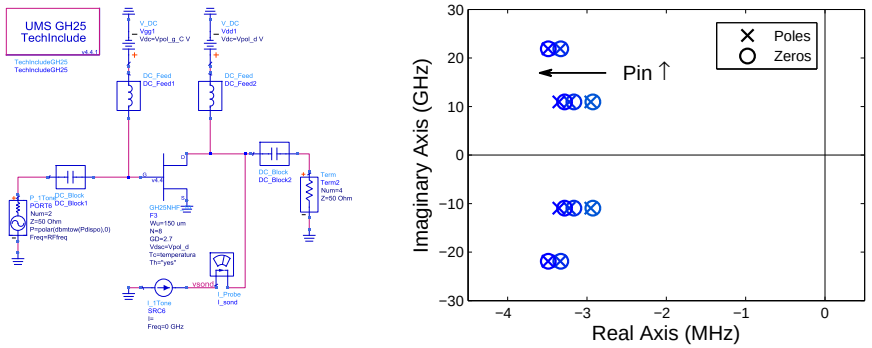

(a) (b)

Figure 3.19: Schematic of the simple cell with a single UMS GH25 $8x150\ \mu m$ transistor and ideal components. (b) Pole-zero diagram of the large-signal parametric analysis varying the input power P_{in} from 5 dBm to 15 dBm.

It should be noted that the imaginary part of the quasi-compensated poles and zeros is always equal to the input frequency f_0, whichever its value and the observation port under analysis. Additionally, a set of very quasi-compensated poles are also detected at $2f_0$ (Figure 3.19b). These two results, and the fact that the very resonant poles at f_0 and $2f_0$ appear for increasing values of P_{in}, would be coherent with the poles at f_0 being the Floquet repetitions of a stable real pole.

Indeed, a real pole and a real zero with small real parts are identified in an AC analysis of the previously mentioned ideal cell (Figure 3.20). Additionally, the real poles and zeros that are identified in an harmonic-balance analysis for $P_{in} = -15\ dBm$ to $P_{in} = 15\ dBm$ are

also plotted in different shades of blue in Figure 3.20. As indicated in Figure 3.20, the critical real poles depart from the pole obtained in the AC analysis and move leftwards for increasing values of P_{in}. Still, all the real poles in Figure 3.20 have very small real parts. Consequently, Floquet exponents associated to these real poles will appear around f_0 and very close to the imaginary axis when a large-signal input drive is applied (Figure 3.19b).

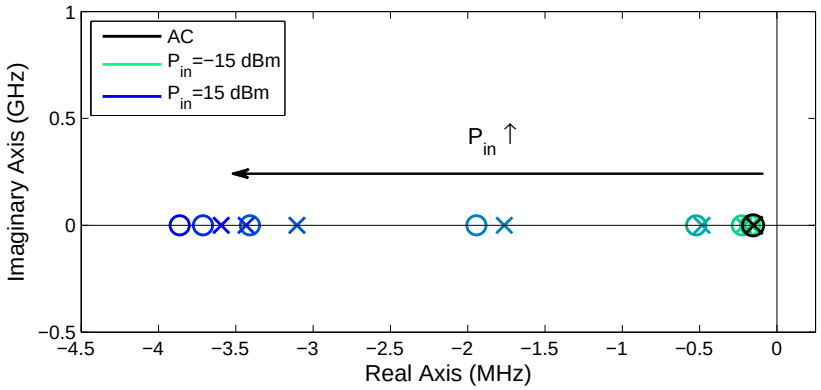

Figure 3.20: Identified real poles and zeros resulting from the small-signal analysis (black) and real poles and zeros resulting from a periodic large-signal analysis varying the input power P_{in} from -15 dBm to 15 dBm.

Note that, by default, the *MM_stab* tool does not plot the real poles in the pole-zero map because they are not resonant. However, in this case, the option for plotting all the poles (resonant and non-resonant) has been chosen to visualize the real poles.

The origin of these real poles has to be linked to the RC networks used to model the thermal behavior or the trapping effects of the transistor. Since access to the model of the UMS library is restricted, there is no way of knowing the particular values and topology of these low frequency networks. However, the thermal origin of these poles can be confirmed by activating and deactivating the thermal model of the transistor. When varying the temperature with the thermal

model of the transistor enabled, the real part of the critical poles varies (Figure 3.21a). But when the thermal model is deactivated, and the temperature is varied as before, the real poles do not move (Figure 3.21b). Consequently, one could conclude that these real poles do indeed model the thermal performance of the transistor.

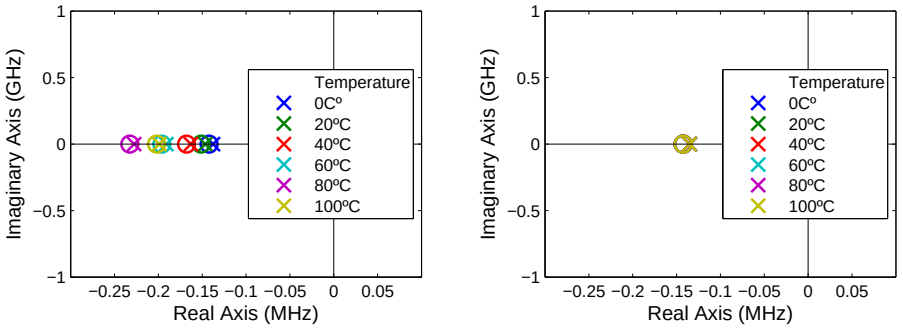

Figure 3.21: Identified real poles resulting from varying the temperature specification of the transistor with the thermal model (a) enabled, (b) disabled.

In conclusion, any design that includes transistor models with thermal modules modeled with RC networks (low dynamics) will have real poles with small real parts and thus their Floquet exponents might appear at f_0 and its harmonics for high input powers.

3.6 Final Design Characteristics

Finally, a stable Doherty amplifier at the fundamental frequency of $f_0 = 10.95\ GHz$ and with a bandwidth of $BW = 500\ MHz$ has been obtained. The dimensions ($4.90\ x\ 4.95mm$) of the final layout are shown in Figure 3.22.

The output power at saturation of the designed Doherty amplifier

at the central frequency $f_0 = 10.95\ GHz$ is of 37.5 dBm (Figure 3.23a) with a gain of 8 dB (Figure 3.23b).

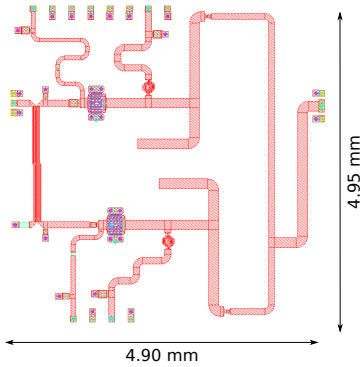

Figure 3.22: Layout of the final design

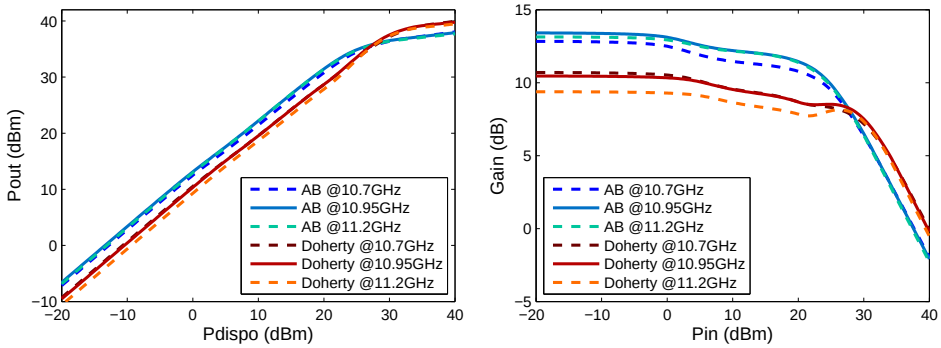

(a) (b)

Figure 3.23: (a) P_{in}-P_{out} curves for a single AB cell amplifier and the Doherty amplifier at 10.7 GHz, 10.95 GHz and 11.2 GHz. (b) Gain curves for a single AB cell amplifier and the Doherty amplifier at 10.7 GHz, 10.95 GHz and 11.2 GHz.

Concerning the gain of the amplifier, between the 6 dB output back-off point and saturation, the variation between the gain at frequencies 10.7 GHz, 10.95 GHz and 11.2 GHz rests smaller than

0.5 dB. However, a higher difference exists at the linear region where the gain at 10.7 GHz is 10.7 dB whilst at 11.2 GHz it takes the value of 9.4 dB.

This being said, from Figure 3.23 we can conclude that the gain of the Doherty amplifier is lower than the gain of a single class AB cell. However, a higher saturation power is obtained with the Doherty amplifier.

High efficiency values have been obtained as can be verified in Figure 3.24.

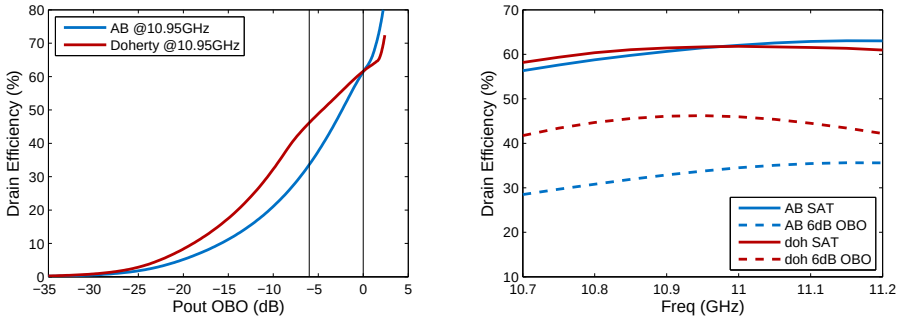

(a) (b)

Figure 3.24: (a) Drain efficiency versus input power at $f_0 = 10.95\ GHz$. (b) Drain efficiency versus input frequency at the 6 dB output back-off point and at saturation.

In saturation, the drain efficiency of the Doherty amplifier for the input frequency of 10.95 GHz is 61.7%, which as expected is practically equal to the efficiency at saturation of a single class AB cell with a 50 Ω load.

The major improvement, with respect to the drain efficiency of the single class AB cell, is obtained at the 6 dB output back-off point and a bit beyond. At the 6 dB output back-off point the drain efficiency of the Doherty design at 10.95 GHz is 46.2%, whilst the drain efficiency

of the class AB cell for the same input frequency is 12.4 percentage points smaller.

It should be noted that the efficiency gain, with respect to the class AB amplifier, at the 6 dB output back-off point can be appreciated for all the frequencies in the 500 MHz bandwidth (Figure 3.24b). The drain efficiency improvement with respect to the class AB cell at 11.2 GHz is considerably lower than at the central frequency (6.6 percentage points higher) and it is a bit higher at 10.7 GHz (13.3 percentage points higher).

A summary of the experimental characteristics of state of the art X-band Doherty amplifiers are given in Table 3.1.

Table 3.1: Summary of experimental X-band PA performance.

Ref.	**Freq (GHz)**	$P_{out}(W)$	**Gain (dB)**	$\mu_{SAT}(\%)$	$\mu_{OBO}(\%)$
[104]	10	4	9.2	57	48
[123]	17	0.3	8	44	30
[124]	21-24	5	17	43	26
[125]	23-25	1.2	12.5	38	20
[126]	14.6	4	7	40	28

It must be noted that, in comparison with the state of the art experimental results, a higher output power with considerably more efficiency has been obtained in simulation for the final design. However, the size of our final design is generally larger and the gain in saturation is some points smaller. This could be overturned with the inclusion of another amplification stage with high gain at the input of the Doherty amplifier but at the cost of reducing the efficiency of the complete design.

3.7 Conclusions

In this chapter the design process of a stable Doherty amplifier has been described.

To begin with, the theory behind the classical Doherty amplifier has been defined, and the multiple possible alternative design configurations have been briefly introduced.

Given that the main objective of the design consisted of understanding the functioning of the classical Doherty power amplifier and applying the MIMO stability analysis methodology and tool introduced in Chapter 2, the final design configuration chosen does not differ much from the classical Doherty.

Many challenges regarding stability have been found in the small-signal and large-signal MIMO stability analysis tests carried out.

Firstly, two low-frequency small-signal instabilities have been correctly identified and their critical nodes have been determined using the residue analysis and ρ factor introduced in Chapter 2. Once the critical nodes have been determined, the instabilities have been stabilized by introducing stabilization resistors at the gate bias paths of both the carrier and peaking amplifiers.

Despite not having found any large-signal instabilities when varying the input power, the input frequency, the bias conditions and in Monte Carlo analyses, a pair of very resonant poles at the fundamental frequency f_0 have been constantly identified. Commonly, designs with poles that are very close to the Y axis (very resonant poles) are said to have low stability margins and thus a thorough analysis should be carried to reduce the chances of them possibly crossing for variations of a parameter of the circuit.

After extensive tests, the origin of the poles at f_0 has been determined. Commonly the transistor models include low-frequency networks to model the performance of the transistor versus temperature.

Consequently, all the transistor models that model the temperature functioning with low-frequency networks, that is with real poles with small real parts, may present their Floquet exponents at the fundamental frequency and its harmonics for increasing values of input power.

Therefore, as demonstrated in this chapter, in order to determine whether the pair of very resonant poles at f_0 appear due to the temperature modeling of the transistor, the designer can carry out the following steps. First, he or she should determine if the very resonant poles at f_0 are detected clearly (not quasi-compensated by zeros) at any of the observation ports of the circuit. If not, the problem should be simplified and only the transistor should be analyzed. Lastly, the designer should focus on detecting the possible real poles that model the temperature and are the origin of the Floquet exponents that appear at f_0.

Finally, and once the stability of the final design is guaranteed, the efficiency, output power and gain characteristics of the final design have been stated. At saturation and for an input frequency of $f_0 = 10.95\ GHz$ an output power of 37.4 dBm with a gain of 8 dB and a drain efficiency of $\mu_{SAT} = 61.7\ \%$ have been simulated. Additionally, and as expected for a Doherty amplifier, high efficiency have also been obtained at the 6 dB OBO point $\mu_{6dB\_OBO} = 46.2\ \%$.

4 Circuit Stabilization for Large-Signal Operation

4.1 Introduction

Due to the inherent nonlinear behaviour, RF power amplifiers have a tendency to generate spurious signals of autonomous nature that show up with variations of the input drive signal, such as, the power level or the frequency. Once the oscillation is detected, the designer must implement effective stabilization solutions that result in the smallest possible impact on the performances of the circuit.

Finding the appropriate values and locations for stabilization for multistage power amplifiers is, in general, an unsystematic trial and error procedure. Consequently, this process often involves the execution of a considerable number of parametric mixer-mode harmonic balance simulations that can be particularly time-consuming.

The systematic small-signal stabilization methodology for multi-transistor circuits introduced in [61] can be applied to determine the location and value of the stabilization networks required to stabilize a microwave amplifier with an instability at the DC or small-signal regime. The evolution of the closed-loop poles versus variations of the stabilization parameter can be predicted by applying standard techniques of linear control theory to a Single-Input Single-Output (SISO) closed-loop transfer function obtained at a given observation port of the circuit, without the need of further simulations.

However, the approach in [61] is not applicable for instabilities detected in the periodic large-signal regime that are function of the periodic input drive signal. As discussed in Chapter 1, stability analyses that are carried out in the presence of a periodic input drive signal require the linearization of the periodic steady state. And the Periodic Linear Time-Varying (PLTV) system resulting from the linearization cannot be represented by a single SISO transfer function.

The Harmonic Transfer Function (*HTF*) matrix, introduced by Wereley in [127], is capable of relating the multiple frequencies of an input signal to the multiple frequencies of the output signal of a PLTV system [128], [129]. Thanks to the matrix structure of the *HTF* matrix, it can be used to define a large-signal stabilization methodology capable of calculating the evolution of the poles of a closed-loop PLTV system.

It should be noted that, a necessary condition to apply the stabilization approach in [61] is that the variations of the control parameter do not affect the dc steady state (fixed by the bias conditions). In general, ensuring this condition for the large-signal regime is more difficult. However, there are a number of conditions for which stabilization parameters have little or no effect on the large-signal steady state under analysis.

In this chapter a generalization of [61] to the periodic large-signal regime, based on the *HTF* matrix, is proposed. With the proposed technique, the evolution of a set of critical poles for variations of a stabilization parameter can be predicted without the need of performing further time consuming nonlinear simulations.

The Multiple-Input Multiple-Output (MIMO) pole-zero identification methodology and tool introduced in Chapter 2 is indispensable to generalize [61] to the periodic large-signal regime, since a tool capable of identifying multiple frequency responses with the same set of poles is required to construct the *HTF* matrix.

As a final note, large-signal harmonic balance simulations can be quite time-consuming, especially when the harmonic balance algorithm faces difficulties to reach the convergence conditions or even runs into converge errors that abort the simulation completely. One might also run into convergence issues, depending on the convergence options set for the harmonic balance simulation and the nonlinear characteristics of the system under analysis. Therefore, any alternative that speeds-up the stabilization analysis is advantageous. Under some circumstances, the methodology proposed in this chapter can be faster than the common alternative of carrying out parametric mixer-mode harmonic balance simulations in the Advanced Design System (ADS) circuit simulation software [59], whilst guarantying the same degree of precision.

4.2 Harmonic Transfer Function

As discussed in Chapter 1, when an exponential signal is introduced to a PLTV system, an infinite number of intermodulation products will appear at the output signal. Consequently, a single SISO transfer function is unable to capture the signal transfers from the different sidebands of the output and input signals [130].

In [127] a matrix transfer function for mapping the signal transfers for PLTV systems, called the Harmonic Transfer Function (HTF), is introduced. This approach considers the signal content in each sideband as a separate and independent input. Thus, a Single-Input Single-Output (SISO) PLTV system can be modeled as a MIMO Linear Time Invariant (LTI) system.

Let us consider a nonlinear system described by the following state-space equation:

$$\dot{\overline{x}} = f(\overline{x}) \tag{4.1}$$

The $\overline{x}$ variable in (4.1) is the state vector and f is a continuous and infinitely derivable function.

Let us denote $\overline{x}_o(t)$ a periodic solution of (4.1), with period $T = 1/f_0$, and $\overline{\xi}(t)$ a small-signal perturbation around $\overline{x}_o(t)$. The linearization of the system dynamics around the periodic solution is given by the PLTV system in (4.2) where $\mathbb{G}(t) = Jf(\overline{x}_o(t))$ is the Jacobian matrix evaluated along the periodic solution $\overline{x}_o(t)$.

$$\dot{\overline{\xi}} = \mathbb{G}(t)\overline{\xi}(t) \tag{4.2}$$

To obtain an input/output representation of the linearized system, an input vector $\overline{u}(t)$ is introduced in (4.2) and the system output $\overline{y}(t)$ is defined as a linear combination of the state variables (4.3).

$$\begin{aligned} \dot{\overline{\xi}} &= \mathbb{G}(t)\overline{\xi}(t) + \mathbb{B}(t)\overline{u}(t) \\ \overline{y}(t) &= \mathbb{C}(t)\overline{\xi}(t) + \mathbb{D}(t)\overline{u}(t) \end{aligned} \tag{4.3}$$

Note that $\mathbb{G}(t)$, $\mathbb{B}(t)$, $\mathbb{C}(t)$ and $\mathbb{D}(t)$ are periodic with the same period T as the periodic solution $\overline{x}_o(t)$.

As discussed in Chapter 1, the test input signal $\overline{u}(t)$ introduced to the linearized system consists of the complex exponential signal in (4.4).

$$\overline{u}(t) = \overline{U}_0 e^{st} \tag{4.4}$$

However, a PLTV system relates the input signal in (4.4) to the many intermodulation products at $s + jk\omega_0$ of the output signal. That is, the output signal of a PLTV system is an Exponentially Modulated Periodic (EMP) signal that can be expanded as a Fourier series of a

periodic signal with a fundamental frequency of f_0, modulated by a complex exponential signal [129]:

$$\overline{y}(t) = e^{st} \sum_{k \in Z} \overline{Y}_k e^{jk\omega_0 t} = \sum_{k \in Z} \overline{Y}_k e^{s_k t} \tag{4.5}$$

where $t \geqslant 0$, $s_k = s + jk\omega_o$, and $s \in C$.

Consequently, and in order to correctly formulate the matrix formalism, the input signal should also be defined as an EMP signal (4.6) [127].

$$\overline{u}(t) = \sum_{k \in Z} \overline{U}_k e^{s_k t} \tag{4.6}$$

And if the $\overline{u}(t)$ input signal is an EMP signal, the state space vector $\overline{\xi}(t)$ is also an EMP signal (4.7).

$$\overline{\xi}(t) = \sum_{k \in Z} \overline{\xi}_k e^{s_k t} \tag{4.7}$$

Since the input and output signals are EMP signals, a linear transfer function matrix can be defined to relate the input (4.6) and output (4.5) signals, which is known as the Harmonic Transfer Function (HTF).

In order to define the HTF matrix, the $\mathbb{G}(t)$, $\mathbb{B}(t)$, $\mathbb{C}(t)$, $\mathbb{D}(t)$ matrices in (4.3) must be expanded as Fourier series:

$$\begin{aligned} \mathbb{G}(t) &= \sum_{k \in Z} G_k e^{jk\omega_0 t} \qquad \mathbb{B}(t) = \sum_{k \in Z} B_k e^{jk\omega_0 t} \\ \mathbb{C}(t) &= \sum_{k \in Z} C_k e^{jk\omega_0 t} \qquad \mathbb{D}(t) = \sum_{k \in Z} D_k e^{jk\omega_0 t} \end{aligned} \tag{4.8}$$

Expanding (4.3) in terms of the previously defined Fourier series in (4.5), (4.6), (4.7) and (4.8), the following system of equations is obtained:

$$\begin{aligned}\sum_k s_k\overline{\xi}_k e^{s_k t} &= \sum_k \left(\sum_m G_{k-m}\overline{\xi}_m + \sum_m B_{k-m}\overline{U}_m\right) e^{s_k t} \\ \sum_k \overline{Y}_k e^{s_k t} &= \sum_k \left(\sum_m C_{k-m}\overline{\xi}_m + \sum_m D_{k-m}\overline{U}_m\right) e^{s_k t}\end{aligned} \tag{4.9}$$

The principle of harmonic balance implies that these equations must be fulfilled for each frequency, s_k. Therefore, equation (4.9) can be rewritten compactly by matching the Fourier coefficients:

$$\begin{aligned}s\overline{\boldsymbol{\xi}} &= (\widehat{G} - \mathcal{N})\overline{\boldsymbol{\xi}} + \widehat{B}\overline{U} \\ \overline{Y} &= \widehat{C}\overline{\boldsymbol{\xi}} + \widehat{D}\overline{U}\end{aligned} \tag{4.10}$$

where the $\overline{\boldsymbol{\xi}}$, $\overline{U}$ and $\overline{Y}$ variables in equation (4.10) are infinite vectors consisting of Fourier coefficients, the $\widehat{G}$, $\widehat{B}$, $\widehat{C}$ and $\widehat{D}$ matrices are Toeplitz matrices of the Fourier coefficients (4.11) and $\mathcal{N}$ is the diagonal matrix defined in (4.12).

$$\widehat{G} = \begin{bmatrix} \ddots & \vdots & \vdots & \vdots & \iddots \\ \dots & G_0 & G_{-1} & G_{-2} & \dots \\ \dots & G_1 & G_0 & G_{-1} & \dots \\ \dots & G_2 & G_1 & G_0 & \dots \\ \iddots & \vdots & \vdots & \vdots & \ddots \end{bmatrix} \tag{4.11}$$

$$\mathcal{N} = blkdiag\left\{jk\omega_0 I\right\} \tag{4.12}$$

The *HTF* matrix is defined as the matrix that relates the $\overline{U}$ sidebands of the input signal and the $\overline{Y}$ sidebands of the output signal of the PLTV system in (4.10):

$$\begin{pmatrix} \cdots \\ \overline{Y}_{-1} \\ \overline{Y}_0 \\ \overline{Y}_1 \\ \cdots \end{pmatrix} = HTF(s) \begin{pmatrix} \cdots \\ 0 \\ \overline{U}_0 \\ 0 \\ \cdots \end{pmatrix} \tag{4.13}$$

and can be derived from (4.10) as follows:

$$HTF\,(s) = \widehat{C}(sI - (\widehat{G} - \mathcal{N}))^{-1}\widehat{B} + \widehat{D} \tag{4.14}$$

Given that each element of the *HTF* matrix models the relation between a particular sideband of the input signal and a particular sideband of the output signal, the *HTF* matrix is an infinite matrix with the structure in (4.15):

$$HTF(s) = \begin{pmatrix} \ddots & \vdots & \vdots & \vdots & \iddots \\ \cdots & H_0\,(s - j\omega_0) & H_{-1}\,(s) & H_{-2}\,(s + j\omega_0) & \cdots \\ \cdots & H_1\,(s - j\omega_0) & H_0\,(s) & H_{-1}\,(s + j\omega_0) & \cdots \\ \cdots & H_2\,(s - j\omega_0) & H_1\,(s) & H_0\,(s + j\omega_0) & \cdots \\ \iddots & \vdots & \vdots & \vdots & \ddots \end{pmatrix} \tag{4.15}$$

The poles of the *HTF* matrix determine the stability of the PLTV system and can be obtained from solving (4.16).

$$det(sI - (\widehat{G} - \mathcal{N})) = 0 \tag{4.16}$$

It must be noted that, as mentioned in [127], the *HTF* matrix is an infinitely dimensional matrix, but in practice, not all infinite elements are considered. Often, the matrix is truncated and only a selection of $2NH + 1$ significant sidebands are considered: the $-NH$ negative sidebands, the zero element and the NH positive sidebands. The implication is that if sufficient sidebands are considered when constructing the *HTF* matrix, the effects of the truncation can be discarded.

As demonstrated in this section, the *HTF* matrix is a general formulation that serves to relate the infinite sidebands of an input/output representation of a PLTV system. It has widely proven its applicability for studying periodic systems of all types such as, rotors of helicopters [131]–[133], xerographic printers [134], wind turbines [135]–[137] and inverted locomotives [138], [139].

It should be noted that the *HTF* matrix is equivalent to the conversion matrix, which is typically used in microwave circuit analysis. The conversion matrix is used to linearize the nonlinear elements of a circuit around a periodic large-signal steady state [4], [77].

4.3 Feedback of the Harmonic Transfer Function

For stabilization of DC or small-signal instabilities, standard linear control theory techniques can be easily applied to a SISO transfer function that relates a small-signal input signal $\overline{U}(s)$ at f_s to the small-signal output signal $\overline{Y}(s)$ also at f_s (Figure 4.1a) [61]. This way, from a single transfer function one can determine whether the inclusion of a negative feedback to the system provides a stable closed-loop system.

However, direct root-locus tracing is not applicable for predicting the effects of the stabilization networks for instabilities at the periodic large-signal regime due to the PLTV nature of the system resulting from the linearization of the periodic large-signal regime.

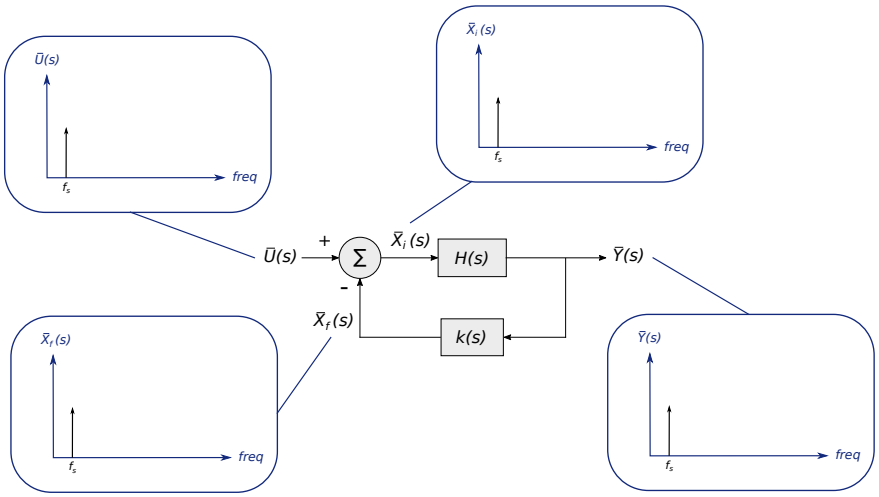

(a)

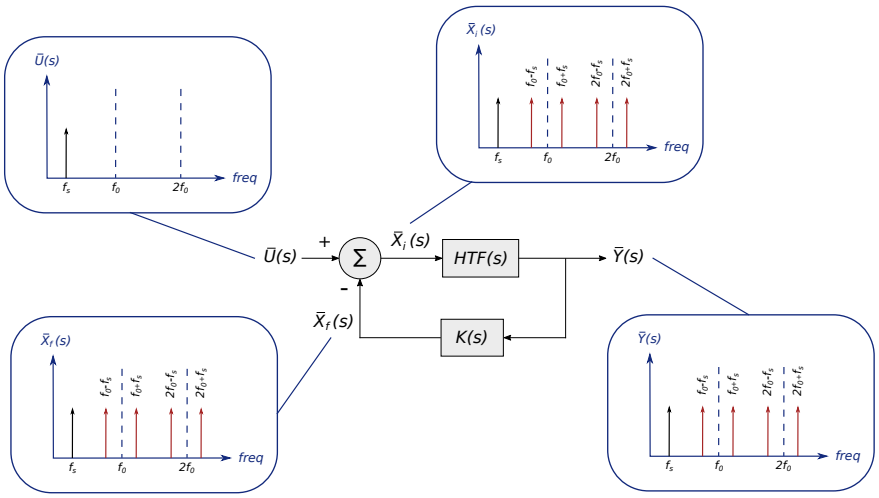

(b)

Figure 4.1: Block diagram of (a) a closed-loop control system of a LTI system. (b) a closed-loop control system of a PLTV system.

A valid alternative to the root-locus analysis for the periodic large-signal regime consists of analyzing the poles of the closed-loop system in Figure 4.1b, for different stabilization networks. This way, the pole evolution of the closed-loop system versus variations of a stabilization parameter can be predicted.

As shown in Figure 4.1b, the MIMO nature of the calculus must be respected when applying a negative feedback $K(s)$ to the open-loop system defined by the HTF matrix. That is, the multiple sidebands must be taken into account when calculating the closed-loop system.

The feedback transfer function matrix $K(s)$ can be defined, in general, as to affect each frequency sideband differently.

$$K(s) = \begin{bmatrix} \ddots & \vdots & \vdots & \vdots & \iddots \\ \dots & k_0(s-j\omega_0) & k_{-1}(s) & k_{-2}(s+j\omega_0) & \dots \\ \dots & k_1(s-j\omega_0) & k_0(s) & k_{-1}(s+j\omega_0) & \dots \\ \dots & k_2(s-j\omega_0) & k_1(s) & k_0(s+j\omega_0) & \dots \\ \iddots & \vdots & \vdots & \vdots & \ddots \end{bmatrix} \tag{4.17}$$

For the large-signal regime, the closed-loop system in Figure 4.1b can be represented by the $HTF_{cl}(s)$ closed-loop transfer function matrix that relates the small-signal input signal $\overline{U}(s)$ and the output signal $\overline{Y}(s)$ as follows:

$$HTF_{cl}(s) = \frac{\overline{Y}(s)}{\overline{U}(s)} = \left[I + HTF(s)K(s)\right]^{-1} HTF(s) \tag{4.18}$$

It should be noted that in order to apply the feedback analysis, one must ensure that the inclusion of a stabilization network in the presence of the input drive signal does not alter the periodic large-signal steady state [61]. In general, this is more difficult to ensure for the large-signal regime than for the DC regime.

Nonetheless, there are a number of cases for which the variations of the stabilization parameter have little or no effect on the large-signal steady state under study. One case corresponds to the inter-branch resistors introduced to stabilize odd-mode instabilities in amplifiers with power-combined topologies (Figure 4.2a). A second case concerns the low-frequency instabilities associated to a gain expansion versus input power that are often stabilized introducing stabilization resistors in series with capacitances in the bias paths (Figure 4.2b).

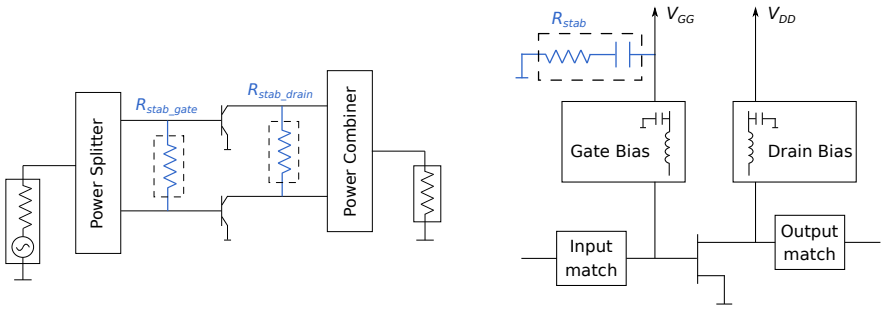

(a) (b)

Figure 4.2: Illustration of (a) inter-branch resistors introduced to stabilize odd-mode instabilities in multistage amplifiers with power combining structures. (b) a stabilization resistor introduced in series with a capacitance in the bias path to eliminate low frequency oscillations.

In order to stabilize the previously mentioned two cases, a stabilization resistor is connected in parallel or series at a given node or branch of the circuit. In both cases, the applied proportional feedback transfer function $K(s)$ is therefore a constant and diagonal matrix:

$$K(s) = \begin{bmatrix} \ddots & \vdots & \vdots & \vdots & \iddots \\ \dots & k & 0 & 0 & \dots \\ \dots & 0 & k & 0 & \dots \\ \dots & 0 & 0 & k & \dots \\ \iddots & \vdots & \vdots & \vdots & \ddots \end{bmatrix} \tag{4.19}$$

4.3.1 Parallel Connection of a Stabilization Resistor

Let us first analyze the case of the parallel connection of a stabilization resistor R_{stab} at node n (Figure 4.3a). As mentioned previously, by applying standard linear control theory techniques to the $HTF^n(s)$ matrix obtained at node n, the evolution of the poles of the closed-loop system $HTF^n_{cl}(s)$ versus variations of the stabilization resistor R_{stab} can be obtained.

The $HTF^n(s)$ matrix consists of a matrix of transfer functions that relates the small-signal current input $\overline{u} = i_{in}(s)$ at f_s and all the sidebands of the voltage output $\overline{y} = v^n(s)$ indicated in Figure 4.3b, as discussed in section 4.2.

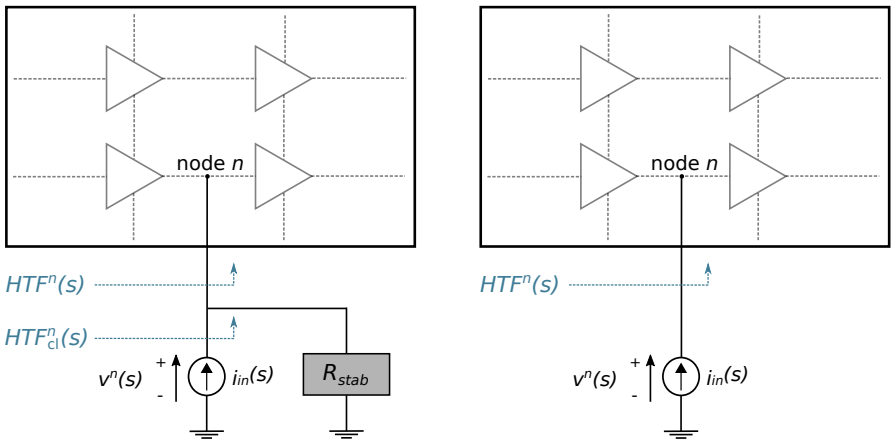

(a) (b)

Figure 4.3: (a) Parallel connection of a stabilization resistor R_{stab} within an impedance stability analysis. (b) The $HTF^n(s)$ matrix obtained at node n relates the current input signal $i_{in}(s)$ and all the sidebands of the $v^n(s)$ voltage output signal.

Similar as for the DC or small-signal stabilization techniques discussed in Chapter 1, if the stabilization resistance R_{stab} is introduced

in parallel, the k constant gain in (4.19) will be $k = 1/R_{stab}$:

$$K(s) = \begin{bmatrix} \ddots & \vdots & \vdots & \vdots & \iddots \\ \dots & 1/R_{stab} & 0 & 0 & \dots \\ \dots & 0 & 1/R_{stab} & 0 & \dots \\ \dots & 0 & 0 & 1/R_{stab} & \dots \\ \iddots & \vdots & \vdots & \vdots & \ddots \end{bmatrix} \tag{4.20}$$

The block diagram of the resulting $HTF^n_{cl}(s)$ closed-loop system for the parallel introduction of a stabilization resistor R_{stab} is shown in Figure 4.4. The evolution of the closed-loop poles for variations of the R_{stab} resistor connected in parallel can be determined by calculating the closed-loop system in (4.18) for the particular case in Figure 4.4.

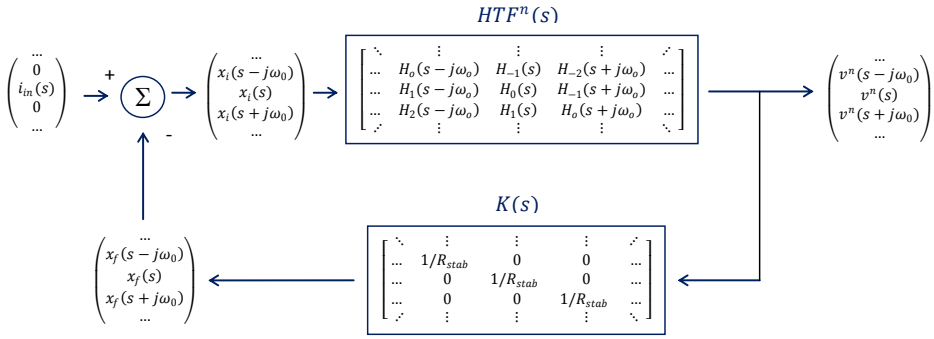

Figure 4.4: Block diagram of the a closed-loop control system resulting from the parallel connection of a stabilization resistor R_{stab}.

4.3.2 Series Connection of a Stabilization Resistor

Let us now analyze the case of the series connection of a stabilization resistor R_{stab} at branch b (Figure 4.5a). Once again, by applying standard linear control theory techniques to the $HTF^b(s)$ matrix obtained

at branch b, the pole evolution of the closed-loop system $HTF^b_{cl}(s)$ versus variations of the stabilization resistor R_{stab} can be obtained.

The $HTF^b(s)$ matrix consists of a matrix of transfer functions that relates the small-signal voltage input $\overline{u} = v_{in}(s)$ at f_s and all the sidebands of the current output $\overline{y} = i^b(s)$ indicated in Figure 4.5b, as discussed in section 4.2.

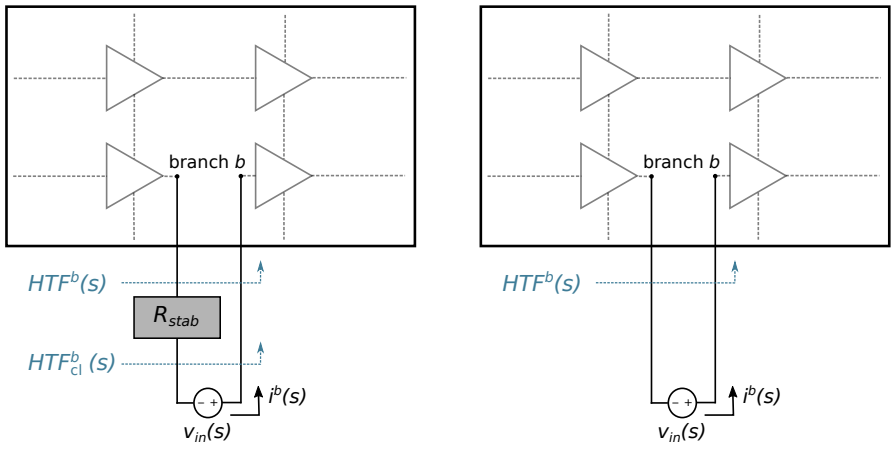

Figure 4.5: (a) Series connection of a stabilization resistor R_{stab} within and admittance stability analysis. (b) The $HTF^b(s)$ matrix obtained at branch b relates the voltage input signal $v_{in}(s)$ and all the sidebands of the $i^b(s)$ current output signal.

Similar as for the DC or small-signal stabilization techniques discussed in Chapter 1, if the stabilization resistance R_{stab} is introduced in series, the k constant gain in (4.19) will be $k = R_{stab}$:

$$K(s) = \begin{bmatrix} \ddots & \vdots & \vdots & \vdots & \iddots \\ \dots & R_{stab} & 0 & 0 & \dots \\ \dots & 0 & R_{stab} & 0 & \dots \\ \dots & 0 & 0 & R_{stab} & \dots \\ \iddots & \vdots & \vdots & \vdots & \ddots \end{bmatrix} \tag{4.21}$$

The block diagram of the resulting $HTF_{cl}^{b}(s)$ closed-loop system for the series introduction of a stabilization resistor R_{stab} is shown in Figure 4.6. The evolution of the closed-loop poles for variations of the R_{stab} resistor connected in series can be determined by calculating the closed-loop system in (4.18) for the particular case in Figure 4.6.

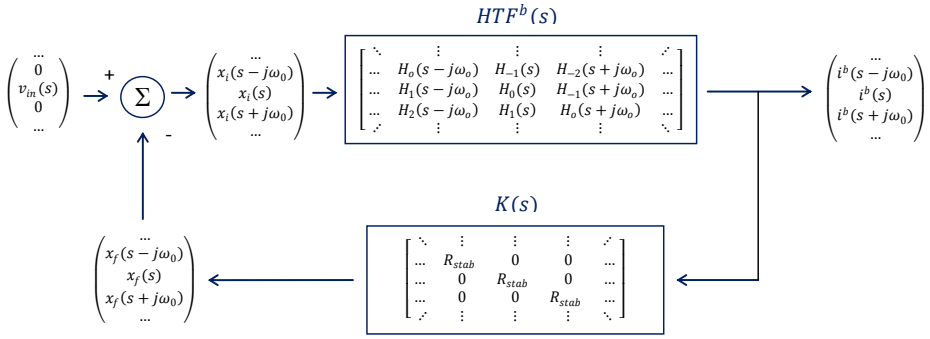

Figure 4.6: Block diagram of the a closed-loop system resulting from the series connection of a stabilization resistor R_{stab}.

4.4 Analytical Example

In order to illustrate the potential to predict the stabilization of a periodic large-signal steady state by calculating the closed-loop system from the analytical *HTF* matrix, the nonlinear resonator circuit introduced in *"Check the Stability: Stability Analysis Methods for Microwave Circuits"* by Almudena Suarez [5] and shown in Figure 4.7 has been analyzed.

The nonlinear resonator circuit in Figure 4.7 consists of a series connection of an input voltage source, a resistor, an inductor and a nonlinear capacitance. When increasing the input voltage e_{in} with a fundamental frequency of $f_0 = 3\ GHz$, the resonant circuit exhibits an instability of frequency division by two, $f_0/2$ (Figure 4.8).

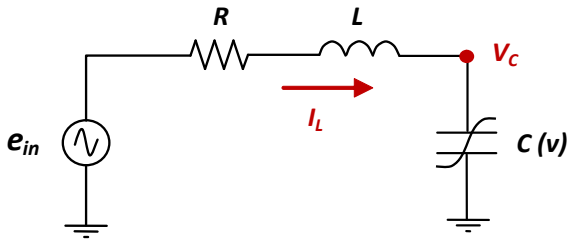

Figure 4.7: Nonlinear resonator circuit with a nonlinear capacitance modeled as $C(v) = a + bv$, with $a = 1\ pF$ and $b = 0.3\ pF/V$, and the element values are $R = 5\ \Omega$, $L = 10\ nH$ [5].

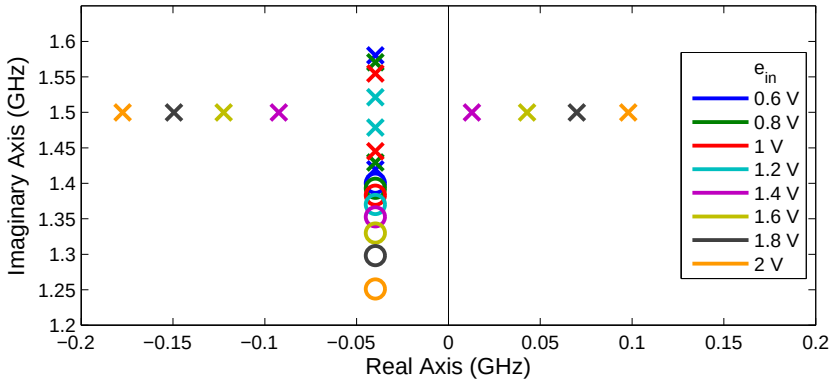

Figure 4.8: Pole-zero map resulting from a parametric pole-zero stability analysis varying the input voltage e_{in} from 0.6 V to 2 V for the nonlinear resonator circuit in Figure 4.7.

As shown in Figure 4.8, a critical stable pole at around 1.6 GHz is identified for small values of e_{in}. However, the critical poles cross to the right-hand side of the s plane at $f_0/2$ for increasing input voltages, $e_{in} \geqslant 1.4\ V$. Particularly, for $e_{in} = 1.4\ V$, a pair of complex conjugate unstable poles at $f_0/2$ are obtained, $p_{1,2} = 2\pi e^9(0.013 \pm j1.5)$.

The circuit in Figure 4.7 can be defined by the equations in (4.22) and (4.23), which are obtained from a Kirchhoff analysis of the circuit:

$$\frac{di_L}{dt} = \frac{e_{in}(t)}{L} - \frac{R}{L} i_L - \frac{v_C}{L} \tag{4.22}$$

$$\frac{dv_C}{dt} = f(v_C, i_L) = \frac{i_L}{(a + 2bv_C)} \tag{4.23}$$

where i_L is the current through the inductor, v_C is the voltage across the capacitor, the capacitance is modeled as $C(v) = a + bv$, with $a = 1\ pF$ and $b = 0.3\ pF/V$, and the element values are $R = 5\ \Omega$, $L = 10\ nH$.

In order to determine the steady state representation of the linearized system from equations (4.22) and (4.23), we select $x(t) = [\ i_L(t) \quad v_C(t)\ ]^T$ as the state vector. For a given input voltage $e_{in}(t)$, we define a periodic large-signal solution $x_0(t)$ and a small perturbation around the periodic solution $\xi(t)$ as in (4.24)

$$x(t) = x_0(t) + \xi(t)$$

$$\begin{bmatrix} i_L(t) \\ \\ v_C(t) \end{bmatrix} = \begin{bmatrix} i_{L\_ps}(t) \\ \\ v_{C\_ps}(t) \end{bmatrix} + \begin{bmatrix} \Delta i_L(t) \\ \\ \Delta v_C(t) \end{bmatrix} \tag{4.24}$$

The linearization of equations (4.22) and (4.23) around the periodic solution $x_0(t) = [\ i_{L\_ps}(t) \quad v_{C\_ps}(t)\ ]^T$ is given by the following PLTV system:

$$\begin{bmatrix} \dfrac{d\Delta i_L(t)}{dt} \\ \\ \dfrac{d\Delta v_C(t)}{dt} \end{bmatrix} = \mathbb{G}(t) \begin{bmatrix} \Delta i_L(t) \\ \\ \Delta v_C(t) \end{bmatrix} \tag{4.25}$$

where $\mathbb{G}(t)$ is the Jacobian matrix evaluated around the periodic solution $x_0(t)$.

$$\mathbb{G}(t) = Jf(\overline{x}_0(t)) = \begin{bmatrix} -\frac{R}{L} & -\frac{1}{L} \\ \left.\frac{\partial f}{\partial i_L}\right|_{\substack{v_{C\_ps} \\ i_{L\_ps}}} & \left.\frac{\partial f}{\partial v_C}\right|_{\substack{v_{C\_ps} \\ i_{L\_ps}}} \end{bmatrix} \tag{4.26}$$

As mentioned previously, the principle of harmonic balance implies that the relations in (4.25) must be fulfilled for all the harmonics of the fundamental frequency f_0. Consequently, and to simplify the calculus, the following steps have been carried out in the frequency domain.

Firstly, the N_k and Z_k Fourier coefficients of the derivatives of the nonlinear $f(v_C, i_L)$ function in (4.23) have been determined with respect to the steady state V_k and I_k Fourier coefficients of v_C and i_L.

$$\left.\frac{\partial f}{\partial i_L}\right|_{\substack{v_{C\_ps} \\ i_{L\_ps}}} = \frac{1}{a + 2b\sum V_k e^{jk\omega_0}} = \sum N_k e^{jk\omega_0} \tag{4.27}$$

$$\left.\frac{\partial f}{\partial v_C}\right|_{\substack{v_{C\_ps} \\ i_{L\_ps}}} = -\frac{2b\sum I_k e^{jk\omega_0}}{(a + 2b\sum V_k e^{jk\omega_0})^2} = \sum Z_k e^{jk\omega_0} \tag{4.28}$$

Given that the V_k and I_k values can be obtained from an harmonic balance analysis carried out in *ADS* [59], the N_k and Z_k parameters can be calculated by solving the two systems of equations in (4.27) and (4.28) for the kf_0 frequencies ($\forall k \in Z$).

Once the N_k and Z_k Fourier coefficients are calculated, the G_k matrix can be defined for each harmonic of the fundamental frequency as follows:

$$G_k = \begin{bmatrix} -\frac{R}{L} & -\frac{1}{L} \\ N_k & Z_k \end{bmatrix} \qquad \forall k \in Z \tag{4.29}$$

In order to predict the value of the stabilization resistor, connected in series, required to stabilize the circuit as described previously in subsection 4.3.2, a small-signal voltage probe is introduced in series to the circuit at branch b (Figure 4.9). For constructing the HTF matrix, we select $u(t) = v_{in}(t)$ as the input signal and $y(t) = i^b(t)$, that is in fact equal to $i_L(t)$, as the output signal.

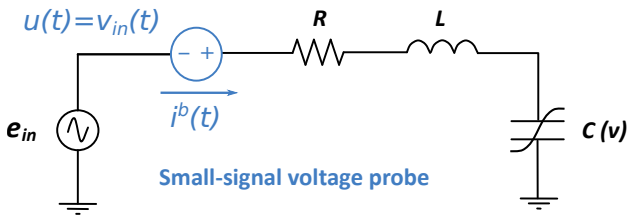

Figure 4.9: Introduction of a small-signal voltage source in series between the e_{in} voltage source and the R resistor.

The state-space representation resulting from the introduction of a small-signal input $u(t)$ to the PLTV system in (4.25) is calculated as follows:

$$\begin{bmatrix} \frac{d\Delta i_L(t)}{dt} \\ \frac{d\Delta v_C(t)}{dt} \end{bmatrix} = \mathbb{G}(t) \begin{bmatrix} \Delta i_L(t) \\ \Delta v_C(t) \end{bmatrix} + \mathbb{B}u(t) \tag{4.30}$$

$$\begin{bmatrix} y(t) \\ 0 \end{bmatrix} = \mathbb{C} \begin{bmatrix} \Delta i_L(t) \\ \Delta v_C(t) \end{bmatrix} + \mathbb{D}u(t)$$

where the $\mathbb{G}(t)$, $\mathbb{B}$, $\mathbb{C}$ and $\mathbb{D}$ matrices can be defined by their G_k, B_k, C_k and D_k Fourier coefficients as in equations (4.29), (4.31), (4.32) and (4.33).

$$B_k = \begin{cases} \begin{bmatrix} 1/L & 0 \end{bmatrix}^T & k = 0 \\ \begin{bmatrix} 0 & 0 \end{bmatrix}^T & k \neq 0 \end{cases} \tag{4.31}$$

$$C_k = \begin{cases} \begin{bmatrix} 1 & 0 \end{bmatrix} & k = 0 \\ \begin{bmatrix} 0 & 0 \end{bmatrix} & k \neq 0 \end{cases} \tag{4.32}$$

$$D_k = \begin{bmatrix} 0 & 0 \end{bmatrix}^T \qquad \forall k \tag{4.33}$$

All the information required to construct the analytical *HTF* matrix has been defined in equations (4.29), (4.31), (4.32) and (4.33). Therefore, by calculating the corresponding Toeplitz matrices $\widehat{G}$, $\widehat{B}$, $\widehat{C}$ and $\widehat{D}$, the analytical *HTF* matrix (4.14) can be constructed.

Once the analytical *HTF* matrix is determined, one can predict the evolution of the closed-loop poles for variations of the R_{stab} resistor connected in series, by calculating the closed-loop system (4.18) for different values of R_{stab}.

However, before calculating the closed-loop system, the size of the *HTF* matrix must be determined. As hinted in Section 4.2, the *HTF* matrix is an infinite size matrix but it must be truncated in order to operate with it. For this example, precise results are obtained with an analytical *HTF* matrix of size $[9 \times 9]$, that is, considering four Fourier coefficients ($NH = 4$).

By applying a proportional feedback gain to the previously determined analytical *HTF* matrix, as discussed in subsection 4.3.2, one

can determine the necessary value of a R_{stab} resistor, connected in series with the small-signal voltage source in Figure 4.9, required to stabilize the circuit.

The poles of the closed-loop system, calculated from the analytical HTF matrix for $R_{stab} = 0.5\ \Omega - 8\ \Omega$, are plotted in Figure 4.10 with crosses (x). From Figure 4.10, it is determined that a stabilization resistor of $R_{stab} = 5\ \Omega$ is sufficient to stabilize the circuit.

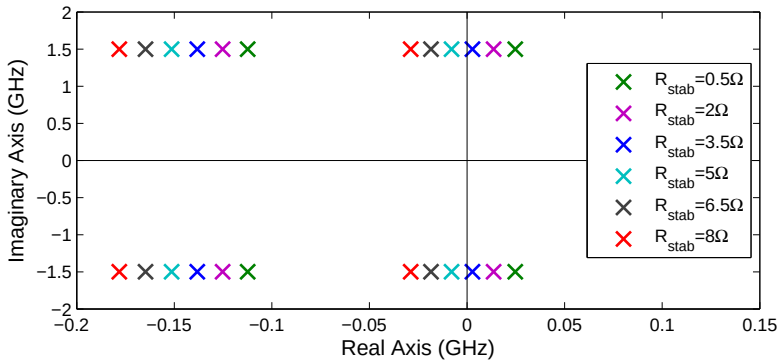

Figure 4.10: Poles resulting from the large-signal HTF matrix feedback stabilization with a series resistor stabilization network (x) for $e_{in} = 1.5\ V$.

It should be noted that this analysis will be valid provided that the variations of the R_{stab} resistor do not vary the large-signal steady state under analysis, which is not the case for this example.

In order to corroborate the accuracy of the proposed periodic large-signal stabilization methodology, a parametric mixer-mode harmonic balance analysis has been carrier out in ADS [59], varying the R_{stab} resistor in Figure 4.11. To ensure that the periodic large-signal steady state does not change when varying R_{stab}, an additional ideal filter has been included in parallel with the R_{stab} stabilization resistor as shown in Figure 4.11. The ideal filter ensures that the periodic large-signal steady state does not change when varying R_{stab}, by presenting a short circuit at the fundamental frequency f_0 and all of its harmonics, and an open circuit at the rest of the frequencies.

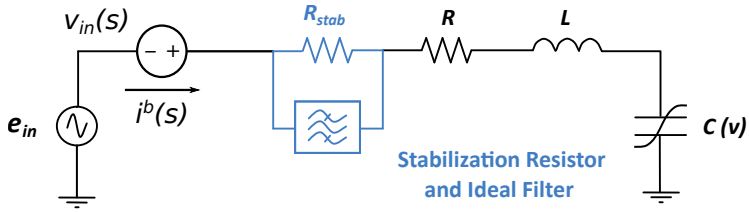

Figure 4.11: Series connection of a stabilization network consisting of a stabilization resistor and an ideal filter. The ideal filter ensures that the periodic large-signal steady state does not change when varying R_{stab}.

The obtained admittance frequency responses have been analyzed with the *MM_ stab* pole-zero stability tool introduced in Chapter 2. As can be verified in Figure 4.12, the poles obtained with the two methods appear completely superimposed. Given that the data points corresponding to the poles of the closed-loop *HTF* matrix (x) and the fitted poles with to the conventional pole-zero identification of parametric frequency responses (+) coincide completely, the combination of both symbols results in an asterisk (∗) symbol.

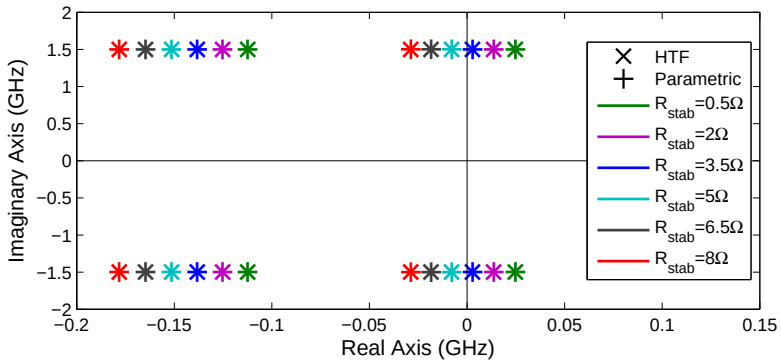

Figure 4.12: Pole diagram containing the poles of the closed-loop system from the feedback analysis of the *HTF* matrix for variations of the R_{stab} resistor (x) and the poles resulting from a conventional parametric stability analysis varying the R_{stab} resistor (+) for $e_{in} = 1.5\ V$.

4.5 Calculation of Non-Analytical Harmonic Transfer Function from Frequency Domain Identifications

In the previous sections an approach for calculating the analytical *HTF* matrix has been introduced, which is based on expanding the periodic matrices of the state-space system into Fourier series. But obviously, calculating the analytical *HTF* matrix is not a realistic option for real circuits [140],[141].

In this section a novel approach, particular for microwave applications, is described. The proposed approach is based on constructing the *HTF* matrix from the results of the frequency domain identification of impedance or admittance frequency responses, obtained by introducing small-signal perturbations to the system linearized around the periodic large-signal steady state.

As a starting point, we propose the utilization of the large-signal frequency responses simulated in *ADS*, and mentioned in Chapter 1, for the construction of a non-analytical *HTF* matrix. In the case of the introduction of a small-signal current probe in parallel at a node i, the obtained impedance frequency responses are of the type in (4.34). Alternatively, a similar analysis can be carried out with a voltage source introduced in series.

$$H_0^i(j\omega_s) = Z_0^i(j\omega_s) = \frac{v^i(\omega_s)}{i_{in}(\omega_s)}$$

$$H_k^i(j\omega_s) = Z_k^i(j\omega_s) = \frac{v^i(k\omega_0 + \omega_s)}{i_{in}(\omega_s)} \tag{4.34}$$

$$H_{-k}^i(j\omega_s) = Z_{-k}^i(j\omega_s) = \left[\frac{v^i(k\omega_0 - \omega_s)}{i_{in}(\omega_s)}\right]^*$$

The $H^i_k(j\omega_s)$ and $H^i_{-k}(j\omega_s)$ frequency responses in (4.34) for $k \neq 0$ are non-Hermitian (4.35). That is, the circuit dynamics around f_0 and its harmonics do not fulfill any symmetry conditions.

$$\begin{aligned} H^i_k(j\omega_s) &\neq H^i_k(-j\omega_s)^* \\ H^i_{-k}(j\omega_s) &\neq H^i_{-k}(-j\omega_s)^* \end{aligned} \tag{4.35}$$

However, the Vector Fitting tool, and consequently the *MM_stab* identification tool, assumes that the frequency responses to be identified are Hermitian. That is, Vector Fittings identifies real coefficients for the identified transfer functions expressed as a ratio of two polynomials.

Consequently, the $H^i_k(s)$ and $H^i_{-k}(s)$ transfer functions obtained with Vector Fitting from the frequency domain identification of the $H^i_k(j\omega_s)$ and $H^i_{-k}(j\omega_s)$ frequency responses in (4.34) will be Hermitian. Given that the transfer functions required to construct the *HTF* matrix are non-Hermitian, the identified $H^i_k(s)$ and $H^i_{-k}(s)$ transfer functions cannot be used to construct the *HTF* matrix.

In any case, a new strategy that avoids the previously mentioned issue has been designed to construct the *HTF* matrix from the simulated $H^i_k(j\omega_s)$ and $H^i_{-k}(j\omega_s)$ frequency responses in (4.34). The proposed strategy consists of the following four steps:

- First, an Hermitian vector $\boldsymbol{\widetilde{H}^i(j\omega_s)}$ of frequency responses is derived from the impedance or admittance frequency responses simulated in *ADS*.

- Secondly, a MIMO transfer function identification of the $\boldsymbol{\widetilde{H}^i(j\omega_s)}$ vector of Hermitian frequency responses is carried out with the *MM_stab* tool introduced in Chapter 2, to obtain $\boldsymbol{\widetilde{H}^i(s)}$.

- Next, given that the transfer functions required to construct the *HTF* matrix are the non-Hermitian transfer functions in $\boldsymbol{H^i(s)}$, the transformation to Hermitian frequency responses carried out in the first step must be reversed. This is done by rearranging the state-space matrices resulting from the MIMO identification.
- Finally, the *HTF* matrix is constructed by shifting the elements of $\boldsymbol{H^i(s)}$, which are the non-Hermitian transfer functions determined in the previous step, as described in equation (4.15).

The four steps of the proposed strategy are described at length in the following paragraphs.

Firstly, a vector of Hermitian frequency responses must be derived from the frequency responses simulated in *ADS* (4.34). In order to do so, one must first take into account that the circuit dynamics is symmetric in module and anti-symmetric in phase around the 0 frequency. That is, the H_k^i and the H_{-k}^i frequency responses for $k \neq 0$ fulfill the following condition:

$$H_k^i(-j\omega_s) = H_{-k}^i(j\omega_s)^* \tag{4.36}$$

By transforming the $H_k^i(j\omega_s)$ and $H_{-k}^i(j\omega_s)$ frequency responses for $k \neq 0$ as follows:

$$\begin{aligned} \widetilde{H}_k^i(j\omega_s) &= \frac{1}{2}(H_k^i(j\omega_s) + H_{-k}^i(j\omega_s)) \\ \widetilde{H}_{-k}^i(j\omega_s) &= \frac{j}{2}(H_k^i(j\omega_s) - H_{-k}^i(j\omega_s)) \end{aligned} \tag{4.37}$$

a new set of $\widetilde{H}_k(j\omega_s)$ and $\widetilde{H}_{-k}(j\omega_s)$ frequency responses for $k \neq 0$ is defined. Given (4.36), it is determined that $\widetilde{H}_k(j\omega_s)$ and $\widetilde{H}_{-k}(j\omega_s)$ frequency responses for $k \neq 0$ are Hermitian:

$$\begin{aligned} \widetilde{H}_k^i(j\omega_s) &= \widetilde{H}_k^i(-j\omega_s)^* \\ \widetilde{H}_{-k}^i(j\omega_s) &= \widetilde{H}_{-k}^i(-j\omega_s)^* \end{aligned} \tag{4.38}$$

It should be noted that since the Hermitian $\widetilde{H}_k(j\omega_s)$ and $\widetilde{H}_{-k}(j\omega_s)$ frequency responses are obtained through a linear combination of the non-Hermitian $H_k(j\omega_s)$ and $H_{-k}(j\omega_s)$ frequency responses, the Hermitian and non-Hermitian frequency responses share the same set of poles.

As a second step, the Hermitian $\widetilde{H}_k^i(j\omega_s)$ and $\widetilde{H}_{-k}^i(j\omega_s)$ frequency responses are reorganized as in (4.39) and a MIMO pole-zero identification is carried out with the *MM_stab* tool introduced in Chapter 2.

$$\widetilde{\boldsymbol{H}}^{\boldsymbol{i}}(\boldsymbol{j\omega_s}) = [\widetilde{H}_{-NH}^i(j\omega_s) \;\; ... \;\; H_0^i(j\omega_s) \;\; ... \;\; \widetilde{H}_{NH}^i(j\omega_s)]^T \tag{4.39}$$

As in the case of the analytical *HTF* matrix, the non-analytical *HTF* matrix must also be truncated. The NH variable in (4.39) makes reference to the number of harmonics considered when constructing the *HTF* matrix. Consequently, the dimensions of the *HTF* matrix will be $[2NH+1 \times 2NH+1]$. Some practical considerations for selecting a suitable number of $2NH+1$ frequency responses have been introduced in the following subsection 4.5.1.

The MIMO identification of the $\widetilde{\boldsymbol{H}}^{\boldsymbol{i}}(\boldsymbol{j\omega_s})$ vector of Hermitian frequency responses, expressed in the state-space representation (4.41), results in the vector of fitted Hermitian transfer functions in (4.40).

$$\widetilde{\boldsymbol{H}}^{\boldsymbol{i}}(\boldsymbol{s}) = [\widetilde{H}_{-NH}^i(s) \;\; ... \;\; \widetilde{H}_0^i(s) \;\; ... \;\; \widetilde{H}_{NH}^i(s)]^T \tag{4.40}$$

$$\widetilde{\boldsymbol{H}}^{\boldsymbol{i}}(\boldsymbol{s}) = \widetilde{\mathcal{C}}(sI - \widetilde{\mathcal{G}})^{-1}\widetilde{\mathcal{B}} + \widetilde{\mathcal{D}} \tag{4.41}$$

where the $\widetilde{\mathcal{G}}$ and $\widetilde{\mathcal{B}}$ matrices contain information regarding the common set of poles identified for the $\widetilde{\boldsymbol{H}}^{\boldsymbol{i}}(\boldsymbol{s})$ vector of Hermitian transfer functions. Whilst the $\widetilde{\mathcal{C}}$ and $\widetilde{\mathcal{D}}$ matrices contain information regarding the residues and direct gain, respectively, of the $\widetilde{\boldsymbol{H}}^{\boldsymbol{i}}(\boldsymbol{s})$ vector of Hermitian transfer functions.

As a third step to construct the *HTF* matrix, the $\boldsymbol{H}^{\boldsymbol{i}}(\boldsymbol{s})$ vector of transfer functions (4.42) that represent the $\boldsymbol{H}^{\boldsymbol{i}}(\boldsymbol{j\omega_s})$ vector of original non-Hermitian frequency responses must be determined from the results of the MIMO identification in (4.41):

$$\boldsymbol{H}^{\boldsymbol{i}}(\boldsymbol{s}) = \mathcal{C}(sI - \mathcal{G})^{-1}\mathcal{B} + \mathcal{D} \tag{4.42}$$

where,

$$\mathcal{G} = \widetilde{\mathcal{G}} \qquad\qquad \mathcal{B} = \widetilde{\mathcal{B}} \tag{4.43}$$

given that the Hermitian and non-Hermitian transfer functions share the same set of poles.

Regarding the computation of the $\mathcal{C}$ and $\mathcal{D}$ matrices, the transformation to Hermitian frequency responses in (4.38) is reverted as follows:

$$\begin{cases} \mathcal{C}_0 = \widetilde{\mathcal{C}}_0 \\ \mathcal{C}_k = \widetilde{\mathcal{C}}_k - j\widetilde{\mathcal{C}}_{-k} \quad k \neq 0 \\ \mathcal{C}_{-k} = \widetilde{\mathcal{C}}_k + j\widetilde{\mathcal{C}}_{-k} \quad k \neq 0 \end{cases} \tag{4.44}$$

$$\begin{cases} \mathcal{D}_0 = \widetilde{\mathcal{D}}_0 \\ \mathcal{D}_k = \widetilde{\mathcal{D}}_k - j\widetilde{\mathcal{D}}_{-k} \qquad k \neq 0 \\ \mathcal{D}_{-k} = \widetilde{\mathcal{D}}_k + j\widetilde{\mathcal{D}}_{-k} \quad k \neq 0 \end{cases} \tag{4.45}$$

Once the $\mathcal{C}$, $\mathcal{G}$, $\mathcal{B}$ and $\mathcal{D}$ unknowns of the $\boldsymbol{H^i(s)}$ vector of non-Hermitian transfer have been determined, the final steps to construct the *HTF* matrix must be carried out.

First, the Toeplitz matrices of the $\mathcal{C}$ and $\mathcal{D}$ are to be calculated as in (4.46) and (4.47).

$$\widehat{\mathcal{C}} = \begin{bmatrix} \ddots & \vdots & \vdots & \vdots & \iddots \\ \dots & \mathcal{C}_0 & \mathcal{C}_{-1} & \mathcal{C}_{-2} & \dots \\ \dots & \mathcal{C}_1 & \mathcal{C}_0 & \mathcal{C}_{-1} & \dots \\ \dots & \mathcal{C}_2 & \mathcal{C}_1 & \mathcal{C}_0 & \dots \\ \iddots & \vdots & \vdots & \vdots & \ddots \end{bmatrix} \tag{4.46}$$

$$\widehat{\mathcal{D}} = \begin{bmatrix} \ddots & \vdots & \vdots & \vdots & \iddots \\ \dots & \mathcal{D}_0 & \mathcal{D}_{-1} & \mathcal{D}_{-2} & \dots \\ \dots & \mathcal{D}_1 & \mathcal{D}_0 & \mathcal{D}_{-1} & \dots \\ \dots & \mathcal{D}_2 & \mathcal{D}_1 & \mathcal{D}_0 & \dots \\ \iddots & \vdots & \vdots & \vdots & \ddots \end{bmatrix} \tag{4.47}$$

Finally, taking into account the $\widehat{\mathcal{C}}$, $\mathcal{G}$, $\mathcal{B}$ and $\widehat{\mathcal{D}}$ matrices obtained from processing the results of the MIMO identification to equation (4.14), the *HTF* matrix can be calculated as follows:

$$HTF(s) = \widehat{\mathcal{C}}(sI - (\mathcal{G} - N))^{-1}\mathcal{B} + \widehat{\mathcal{D}} \tag{4.48}$$

4.5.1 Practical Considerations

A software routine has been coded in *Matlab* [84] to construct the non-analytical *HTF* matrix from the set of $2NH+1$ frequency responses simulated in *ADS*. The software routine constructs the *HTF* matrix by calculating the Hermitian frequency responses, carrying out their MIMO transfer function identification and readjusting the results of the identification automatically.

The main practical considerations that have been successfully tackled when creating the routine are summarized in this subsection.

Dimensions of the *HTF* matrix

As mentioned previously, the *HTF* matrix is an infinite dimension matrix in theory. But, in practice, only a set of NH harmonics must be taken into account for a precise feedback analysis.

From an extensive empirical analysis, it has been determined that the size of the *HTF* matrix required for a precise stabilization estimation can be determined from comparing the magnitude of the H_0^i, H_k^i and H_{-k}^i frequency responses simulated in *ADS*. As a consequence, an empirical strategy to select NH for the non-analytical *HTF* matrix has been determined.

For increasing values of k ($k = 1, 2, ...$) the magnitude of the H_k and H_{-k} frequency responses must be compared with the magnitude of the H_0 frequency response, on a frequency band of $[0,\ kf_0]$. If the conditions in (4.49) and (4.50) are fulfilled for either H_k or H_{-k}, both frequency responses must be taken into account when constructing the *HTF* matrix.

$$|H_k| > |H_0| \quad or \quad |H_{-k}| > |H_0| \tag{4.49}$$

$$H_{ref} = \frac{max(|H_0|) + min(|H_0|)}{2} - 10$$
$$max(|H_k|) > H_{ref} \quad or \quad max(|H_{-k}|) > H_{ref} \tag{4.50}$$

The condition in (4.49) states that the magnitude of either the H_k or H_{-k} frequency responses has to be higher than the magnitude of H_0 for at least one frequency point.

Whilst the condition (4.50) states that the maximum magnitude of either the H_k or H_{-k} frequency responses has to be higher than a reference magnitude H_{ref} that consists of a value 10 dB smaller than the mean of the H_0 frequency response.

Finally, the NH value required to construct the HTF matrix is equivalent to the largest k value for which the conditions in (4.49) and (4.50) are met. Although this is an heuristic strategy to select the dimension of the HTF matrix, it serves to have a high level of confidence on the accuracy of the results.

For example, the impedance frequency responses obtained from introducing a small-signal current source in parallel between the gate nodes of an amplifier with two stages connected in parallel are analyzed in Figure 4.13.

From the corresponding magnitude curves of the H_k and H_{-k} frequency responses in Figure 4.13 the size of the HTF matrix chosen would be $NH = 3$ ($[7 \times 7]$) since all he H_1, H_{-1}, H_2, H_{-2} and H_{-3} curves fulfill both of the conditions. But the magnitude of neither the H_4 or the H_{-4} curves, nor the H_k and the H_{-k} curves for $k \geq 5$, meet the conditions in (4.49) and (4.50).

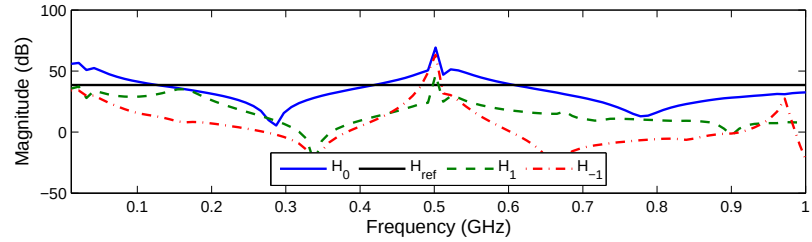

(a)

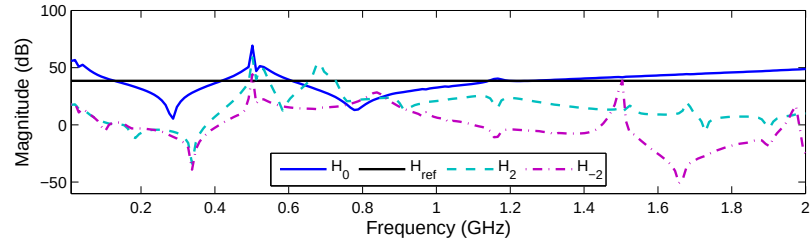

(b)

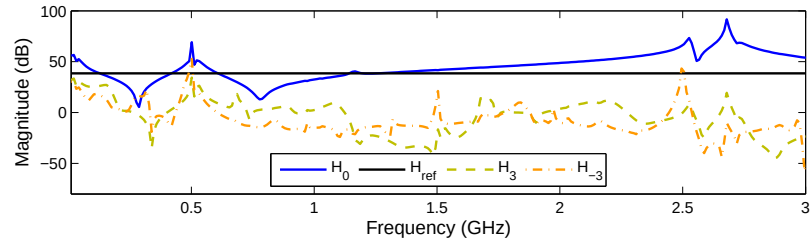

(c)

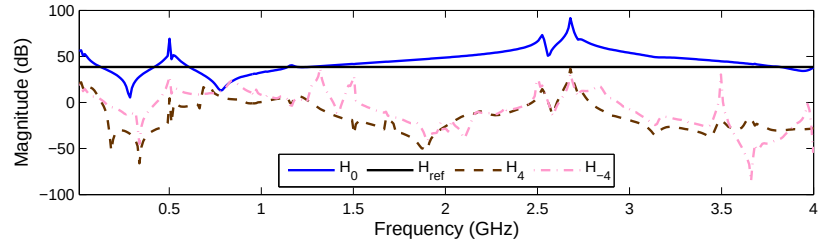

(d)

Figure 4.13: Magnitude of the frequency responses obtained with a small-signal current source introduced in parallel. (a) H_0, H_{ref}, H_1 and H_{-1}. (b) H_0, H_{ref}, H_2 and H_{-2}. (c) H_0, H_{ref}, H_3 and H_{-3}. (d) H_0, H_{ref}, H_4 and H_{-4}.

The evolution of the poles of the closed-loop system for variations of a stabilization resistor R_{stab}, connected in parallel between the gate nodes of the previously mentioned two-stage amplifier, have been calculated from the *HTF* matrices of different sizes. The calculated pole evolutions (x) are compared to the poles identified from a conventional parametric pole-zero identification analysis (+) in Figure 4.14.

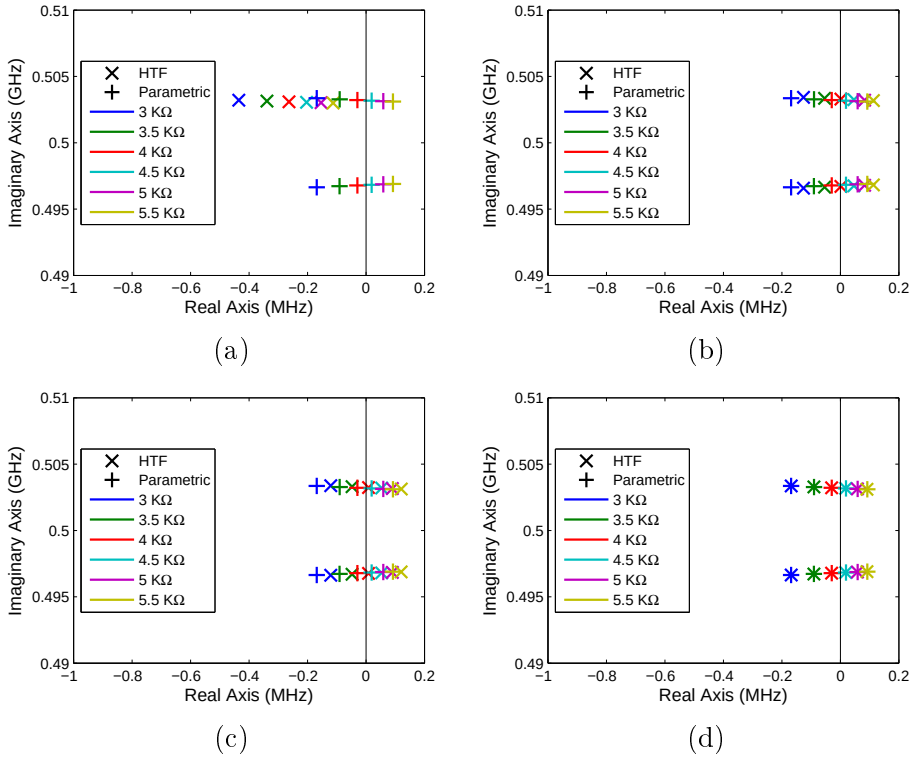

Figure 4.14: Pole-zero map of the closed-loop system derived from the *HTF* matrix for (a) NH=0. (b) NH=1. (c) NH=2. (d) NH=3.

Indeed, the pole evolutions determined from the feedback analysis of the *HTF* matrices of dimensions [1×1] (Figure 4.14a), [3×3] (Figure 4.14b) and [5 × 5] (Figure 4.14c) are not accurate. Whilst increasing the dimensions of the *HTF* matrix from [1 × 1] to [5 × 5] improves the precision of the predicted pole evolution, the poles obtained with the

two different methods (x and +) do not match completely for any of the mentioned dimensions.

However, if the results of the magnitude analysis are considered and the feedback analysis is carried out with a *HTF* matrix of dimension $[7 \times 7]$ ($NH = 3$), an accurate prediction of the pole evolution is achieved. As can be verified in Figure 4.14d, the pole evolution obtained with the feedback analysis and the conventional parametric pole-zero analysis match completely. As in the analytical example, given that the data points of the closed-loop *HTF* analysis (x) and the parametric conventional pole-zero analysis (+) are the same, the combination of both symbols results in an asterisk (*) symbol.

A software routine has also been coded in *Matlab* [84] to determine the size of the *HTF* matrix required for a precise prediction of the stabilization of a circuit using the described approach.

Visualization of the Pole Map

Two possible problems related to the visualization of the pole-zero map might arise when analyzing the poles of the closed-loop system derived from the *HTF* matrix.

Firstly, it must be noted that as a result of the subtraction of the $\mathcal{N}$ matrix in (4.48), that shifts the system poles by $\pm kj\omega_0$, the *HTF* matrix will contain the system poles and its Floquet repetitions at $\pm kj\omega_0$. Consequently, if the order of the MIMO identification is N, the order of the *HTF* matrix will be $N(2NH + 1)$, NH being the number of harmonics considered for constructing the *HTF* matrix.

Although interpreting a pole-zero map with $N(2NH+1)$ poles can be complicated when N and NH take considerable values, the pole-zero map can be simplified straightforwardly thanks to the option of plotting only the resonant poles in a fixed frequency band introduced previously in subsection 2.3.2. By calculating the resonant poles for a

narrow frequency band centered around the frequency of the critical poles, the pole-zero map can be successfully simplified.

Secondly, since the MIMO identification of the large-band frequency responses in (4.39) could have already identified some of the Floquet repetitions, the poles of the HTF matrix may contain duplicated Floquet repetitions.

An additional solution and software routine to eliminate the display of the duplicated Floquet repetitions has been foreseen. In order to apply it, the user must externally define a small reference distance value, so that all the poles that have a zero closer than that small reference distance are considered as pole-zero quasi-compensations. Next, by strategically calculating the euclidean distance between all the poles and the zeros of the closed-loop HTF matrix and comparing them with the reference distance, the pole-zero quasi-compensations can be determined.

Obviously, in order to apply this solution, the zeros as well as the poles of the closed-loop HTF matrix must be calculated. This operation can be quite time-consuming. Given that special emphasis has been applied to optimize the run time of the routine, the detection of pole-zero quasi-compensations is not introduced by default to the stabilization analysis tool that has been designed.

Run Time

The two main operations that can potentially give way to slow run times are the construction of the HTF matrix and the feedback analysis. Many steps have been carried out to speed up the mentioned operations. Some of the applied strategies and the run time results are summarized here.

The computer that has been used to calculate the different run times presented in this document has an Intel $i5-4590$ processor with a processing speed of 3.3 GHz and 8 GB of RAM Memory.

Construction of the HTF Matrix

As mentioned previously, the MIMO identification tool introduced in Chapter 2 has been used to determine the *HTF* matrix from the different frequency responses obtained from mixer-mode harmonic balance analyses carried out in *ADS* [59]. However, the automatic order selection algorithm introduced in subsection 2.3.1 has been slightly modified as follows, in order to speed up the run time.

- First, in the original automatic order selection algorithm, the initial order for the MIMO identification is set equal to the highest number of slope changes of the analyzed frequency responses, $N_{initial} = r$. Since the MIMO frequency responses used to construct the *HTF* matrix require very high orders (N), it has been determined that for this particular application, an improved run time maintaining the identification precision is achieved when the initial order is set to $N_{initial} = (NH - 1)r$.

- Next, in the original automatic order selection algorithm, every time the phase error condition is not met, the Vector Fitting identification is repeated with a new increased order of $N = N + 2$. Given that for this application we can assume that the order will increase considerably, it has been determined that an improved run time maintaining the identification precision is achieved when the new order for the re-identification is set to $N = N + 6$.

- Finally, another step that can improve the speed is to relax the phase error tolerance (θ_{max}) restriction for the MIMO identification from 0.5° to 1°, but at the risk of loosing some precision.

Feedback Analysis

Regarding the computation of the closed-loop *HTF* matrix and its poles, many examples have been analyzed and it has been determined

that the time required for these operations depends on the order of the *HTF* matrix, $N(2NH+1)$.

The relation between the measured run time to determine the feedback closed-loop system and its poles, versus the order of the *HTF* matrix is plotted with green squares in Figure 4.15.

The run time can thus be predicted from equation (4.51), which is the result of a polynomial curve fitting analysis carried out with the *Curve Fitting Toolbox* [142] in *Matlab* [84]. The precision of the fitted function in (4.51) can be verified in Figure 4.15 since the difference between the experimental data (green squares) and the fitted data (black line) is very small.

$$f(x) = 1.24e^{-9}x^3 + 7.29e^{-7}x^2 + 1.84e^{-4}x + 2.28e^{-2} \tag{4.51}$$

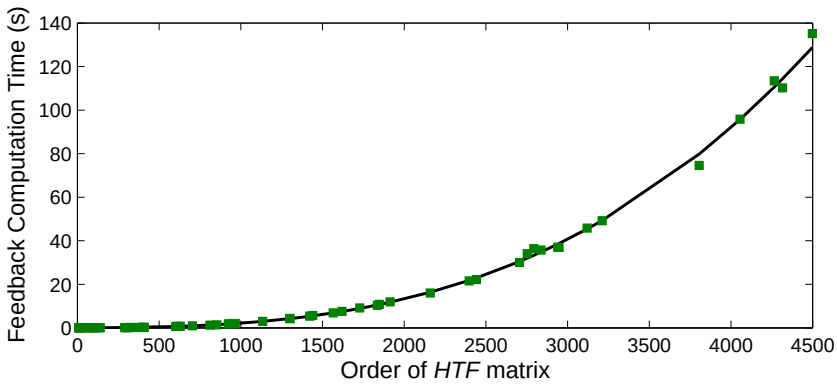

Figure 4.15: Illustration of the measured (green square) and fitted (black line) run time for the feedback analysis versus the $N(2NH+1)$ order of the *HTF* matrix.

The time required for the mixer-mode harmonic balance algorithm in *ADS* to converge varies depending on the circuit and the convergence options. However, given that the N order of the MIMO identification for constructing the *HTF* matrix and the number of harmonics

NH are known before carrying out the feedback analysis, we can predict the time required for the feedback analysis from (4.51).

Consequently, if the $N(2NH+1)$ order of the HTF matrix is not very high, the feedback analysis might be considerably faster than the mixer-mode harmonic balance analysis simulation in ADS, as demonstrated in the following section 4.6.

Nonetheless, the run time of the feedback analysis can also be improved for the cases where $N(2NH+1)$ is too high. For these cases, the most time consuming process is not the computation of the closed-loop system, but the determination of the $N(2NH+1)$ poles of the closed-loop system. In which case, alternative strategies can be used in *Matlab* [84] that instead of calculating all the closed-loop poles, only calculate a given small number (for example, 20) of the poles of the closed-loop system, centered around the frequency of the critical poles. As a result of the mentioned strategy to optimize the run time, only the information regarding the dynamics centered around the critical frequency will be obtained in these cases.

4.6 Application Examples

In this section, the large-signal stabilization method and tool described in the previous section are illustrated with two examples of real circuits.

The first example is the low-frequency large-signal instability at 130 MHz of the three-stage amplifier introduced in Chapter 2 that is stabilized via the introduction of a series resistor in the bias path.

The second example consists of an odd-mode oscillation at $f_0/2$ of a power amplifier prototype designed with two stages connected in parallel that is stabilized via the introduction of a stabilization resistor connected in parallel between the gate nodes of the transistors.

4.6.1 Stabilization of a Low Frequency Oscillation

As mentioned, the first example consists of an instability at 130 MHz that appears on the three-stage amplifier described in Section 2.4.1 (Figure 4.16), when the input power is increased.

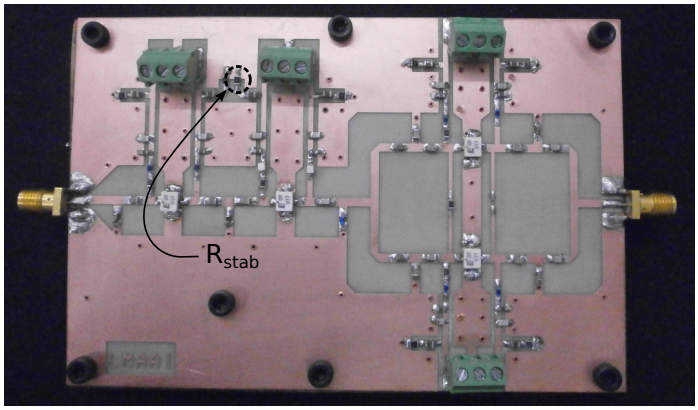

Figure 4.16: Photograph of the fabricated prototype signaling the stabilization resistor R_{stab}.

Due to the high number of components and the use of their real models in simulation, as well as the complexity of the design, it was noted that any parametric mixer-mode harmonic balance analysis of the amplifier was very time consuming. Additionally, and specially for high input power values, the harmonic balance algorithm often aborted due to convergence errors, therefore returning no results of the long parametric simulations.

The R_{stab} resistor that is connected in series with the bias path capacitor in Figure 4.16 is chosen as the stabilization network since its variations do not affect the large-signal steady state.

In order to construct the *HTF* matrix, a small-signal voltage source is introduced in series with the capacitor and from a single mixer-mode harmonic balance simulation, all the admittance frequency responses required to construct the *HTF* matrix are obtained.

As a first step, the magnitudes of the admittance frequency responses at the different sidebands must be analyzed (Figure 4.17). In doing so, the required dimensions of the *HTF* matrix for a precise prediction of the evolution of the closed-loop poles can be determined.

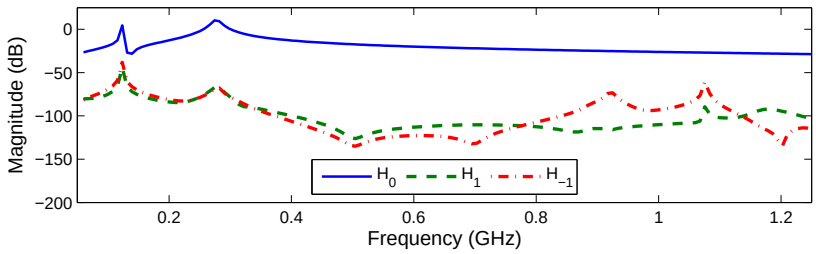

Figure 4.17: Magnitude of the H_0, H_1 and H_{-1} frequency responses obtained with the small-signal voltage source.

From the comparison of the magnitudes of the H_{-1} and H_1 frequency responses with the magnitude of the H_0 frequency response in Figure 4.17, it is determined that an *HTF* matrix of size $[1 \times 1]$ is sufficient to predict the large-signal stabilization of this low-frequency instability.

Therefore, in this case, by tracing the root-locus of just the H_0 frequency response simulated in *ADS* (Figure 4.18) one can predict the evolution of the unstable poles for variations of the stabilization resistor R_{stab} connected in series.

It should be noted that, the fact that only the H_0 frequency response is required to predict the stabilization of this particular instability could have been expected given the low-pass filtering of the bias paths.

Indeed, as can be verified in Figure 4.19, the results obtained with a conventional parametric pole-zero analysis of the H_0 transfer function simulated in *ADS* (+) and the results obtained by applying a proportional feedback of $k = R_{stab}$ to the H_0 transfer function (x)

match completely. As a result of the combination of both symbols, an asterisk symbol (*) is formed for all of the analyzed values of R_{stab}.

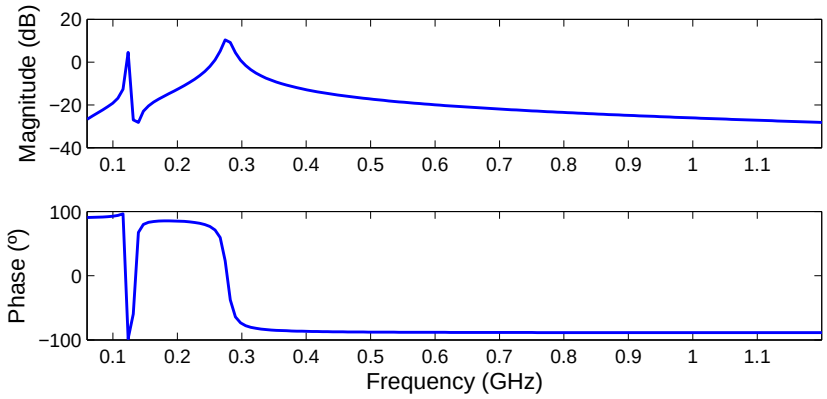

Figure 4.18: Magnitude and phase curves of the H_0 admittance frequency response simulated in *ADS* and required to construct the *HTF* matrix.

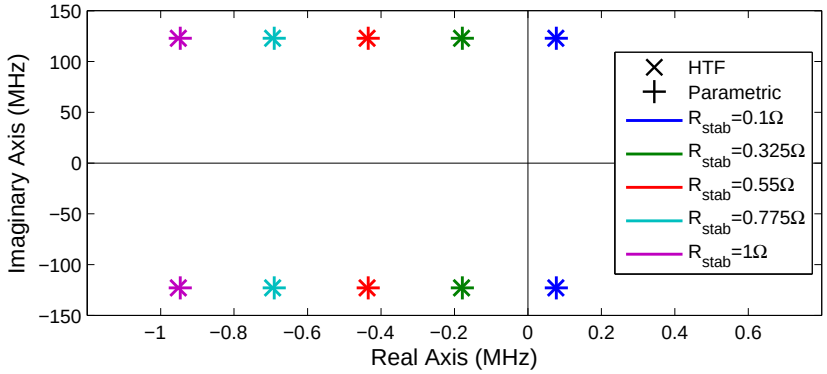

Figure 4.19: Pole diagram containing the poles of the closed-loop system derived from the feedback analysis of the *HTF* matrix for variations of the R_{stab} resistor introduced in series (x) and the poles resulting from a conventional parametric stability analysis varying the R_{stab} resistor (+) for $P_{in} = 1\ dBm$.

As well as the effectiveness of the large-signal stabilization analysis, from Figure 4.19 it is determined that a very small stabilization resistor value $R_{stab} = 0.325\ \Omega$ is sufficient to stabilize the circuit. However, in practice, a higher stabilization resistor value would be selected to guarantee higher stability margins.

As mentioned previously, the mixer-mode harmonic balance analysis is very time consuming for this example. Let us consider a simple narrow-band parametric analysis, obtained by introducing a small-signal voltage source in series with the stabilization resistor in *ADS* for a frequency band of [100 MHz, 200 MHz] and 51 data points. The simulation of the frequency response in *ADS* for a parametric analysis of 10 parameter values is higher than 10 minutes as shown in the data points plotted in blue in Figure 4.20.

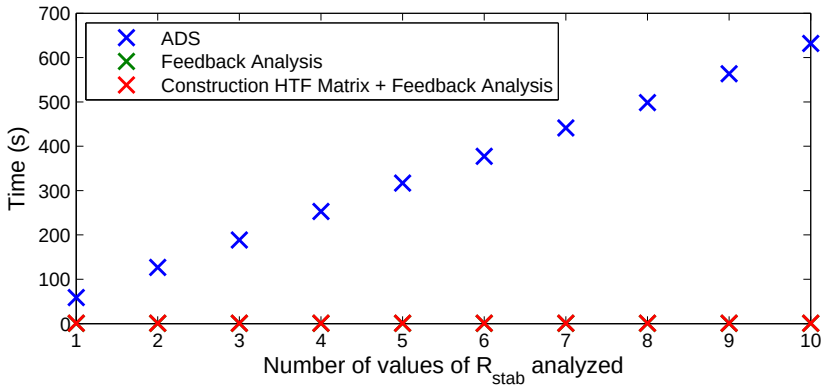

Figure 4.20: Run time versus number of values of the R_{stab} analyzed for the conventional parametric analysis of frequency responses obtained in *ADS* (blue), the feedback analysis (green) and the construction of the *HTF* matrix and feedback analysis (red).

Due to the fact that the *HTF* matrix consists solely on the H_0 transfer function, the prediction of the evolution of the closed-loop poles, or in this case the root-locus analysis, is almost immediate. Indeed, the feedback analysis for 10 values of R_{stab} takes only one 0.5

seconds, as plotted in green in Figure 4.20. Whilst the computation of the *HTF* matrix and the feedback analysis for 10 values of R_{stab} is carried out in only one second, as plotted in red in Figure 4.20. That is, both curves appear superimposed in Figure 4.20, but the run time results plotted in green are slightly faster than the run time results plotted in red.

In particular, in the case shown in Figure 4.19 where a feedback analysis of 5 values of R_{stab} is carried out, the large-signal stabilization method proposed in this chapter is 690 times faster than the conventional strategy of simulating a parametric mixer-mode harmonic balance simulation in *ADS*.

4.6.2 Stabilization of an Odd-mode Oscillation

A specific prototype has been designed in microstrip technology to illustrate the proposed methodology. The prototype contains two GaN HEMPTs (CGH40010) connected in parallel, delivering 41.3 dBm with a gain of 11.8 dB in saturation and for a nominal input frequency of $f_0 = 1\ GHz$. A photograph of the fabricated prototype is shown in Figure 4.21.

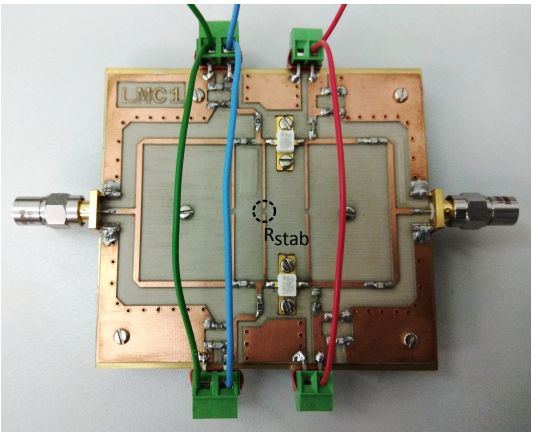

Figure 4.21: Photograph of the fabricated prototype signaling the stabilization resistor R_{stab}.

Whilst the amplifier is stable in DC for the nominal bias conditions, it exhibits an odd-mode instability of frequency division by two ($f_0/2$) when the input power introduced to the amplifier at $f_0 = 1\ GHz$ is higher than $Pin = 1\ dBm$ (Figure 4.22).

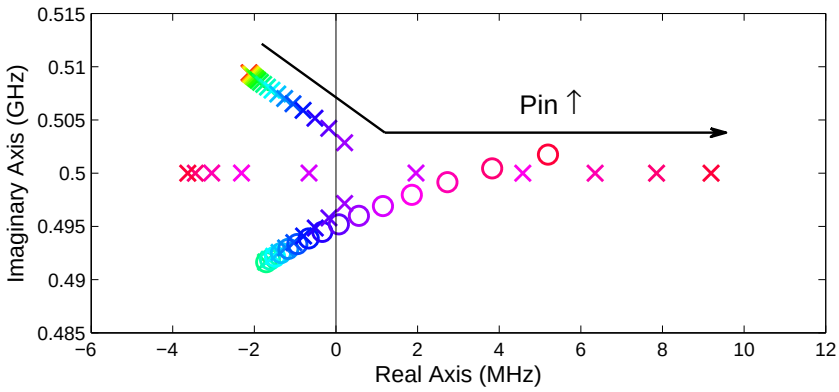

Figure 4.22: Pole-zero map resulting from the frequency domain identification of a parametric frequency response obtained by exciting the odd-mode of the amplifier for $P_{in} = -20\ dBm$ to $5\ dBm$.

A R_{stab} stabilization resistor connected between the gates of the transistors (Figure 4.21) is chosen as the stabilization network, since it is the optimum solution for stabilization of odd-mode oscillations without affecting the even mode large-signal steady state.

To obtain the frequency responses required to construct the non-analytical HTF matrix, a current source is introduced between the transmission lines indicated in Figure 4.21 and the impedance frequency responses required to construct the HTF matrix are obtained.

In order to determine the size of the truncated HTF matrix required for a correct stabilization prediction, the magnitude curves of the H_k and H_{-k} for $k = 1, 2, ...$ frequency responses must be compared with the magnitude curve of the H_0 frequency response (Figure 4.23).

The magnitude of the H_4 and H_{-4} frequency responses is larger than the magnitude of the H_0 frequency response for example at around 0.75 GHz (Figure 4.23a). Additionally, the magnitude of the H_4 and H_{-4} frequency responses is also over the H_{ref} condition for multiple frequency values. Thus, the H_4 and H_{-4} frequency responses must be taken into account when constructing the HTF matrix. However, the H_5 and H_{-5} frequency responses do not the meet the mentioned two magnitude conditions (Figure 4.23b).

Therefore, from the magnitude curves in Figure 4.23, it is determined that an HTF matrix of size $[9 \times 9]$ ($NH = 4$) is sufficient to analyze the large-signal stabilization of this odd-mode instability.

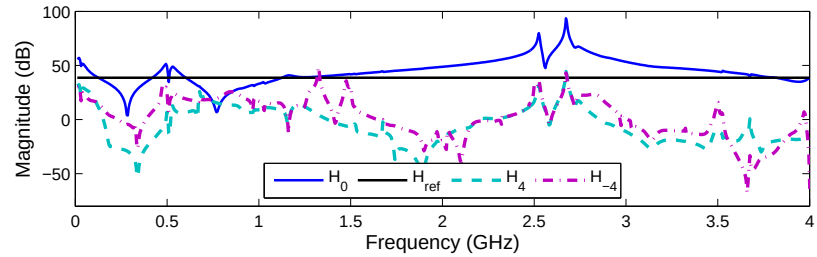

(a)

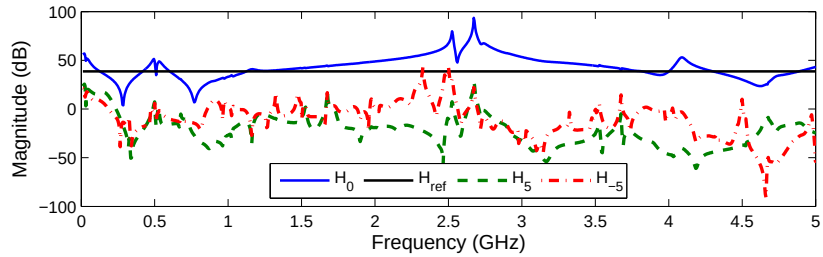

(b)

Figure 4.23: Magnitude of the frequency responses obtained with the small-signal current source (a) H_0, H_{ref}, H_4 and H_{-4}. (b) H_0, H_{ref}, H_5 and H_{-5}.

By calculating the closed-loop system from the HTF matrix constructed from the H_0, H_1, H_{-1}, H_2, H_{-2}, H_3, H_{-3}, H_4 and H_{-4} fre-

quency responses simulated in *ADS* (Figure 4.24), one can predict the evolution of the unstable poles when sweeping the value of R_{stab}.

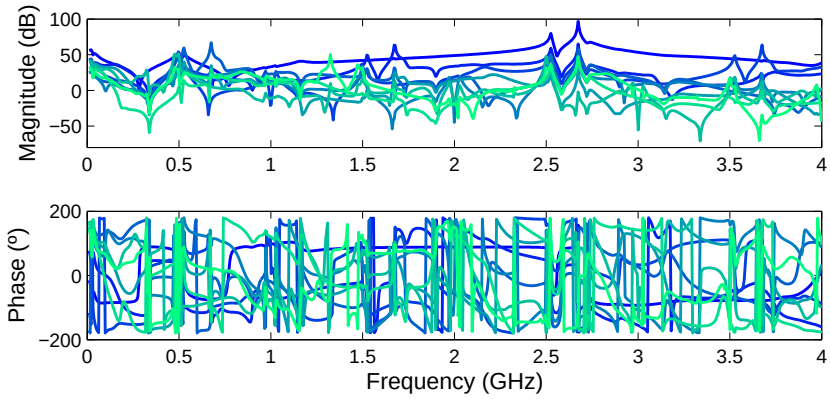

Figure 4.24: Magnitude and phase curves of the H_0, H_1, H_{-1}, H_2, H_{-2}, H_3, H_{-3}, H_4 and H_{-4} impedance frequency responses simulated in *ADS* and required to construct the *HTF* matrix.

Indeed, as can be verified in Figure 4.25, the poles identified with a conventional parametric pole-zero analysis of the H_0 transfer function simulated in *ADS* (+) and the closed-loop poles identified by applying a proportional feedback of $k = 1/R_{stab}$ to the *HTF* matrix of size [9×9] (x) match completely. As a result of the combination of both symbols, an asterisk symbol (*) is formed for all the analyzed values of R_{stab}.

From Figure 4.25 it is determined that a stabilization resistor value $R_{stab} = 300\ \Omega$ is sufficient to stabilize the circuit. However, in practice a smaller stabilization resistor value would be selected to guarantee higher stability margins.

The mixer-mode harmonic balance analyses for this circuit are not as time consuming as is the previous example. For a fair comparison, a simple narrow-band parametric analysis, obtained by introducing a small-signal current source between the gates of the transistors in *ADS* for a frequency band of $[0.4\ GHz,\ 0.5\ GHz]$ and 101 data points is

analyzed. The run time of a conventional analysis in *ADS* is plotted in blue in Figure 4.26.

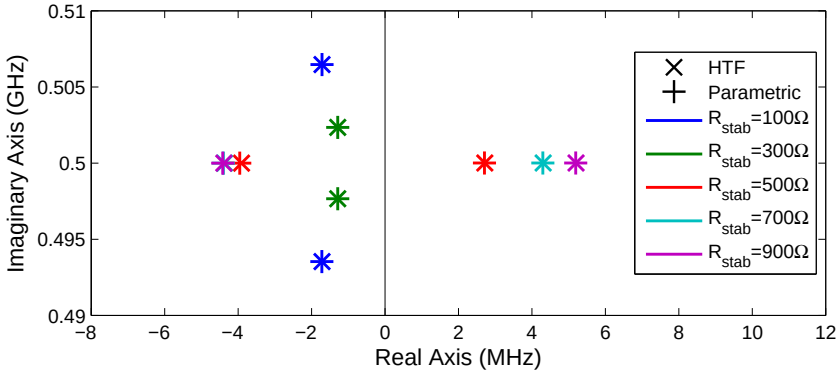

Figure 4.25: Pole diagram containing the poles of the closed-loop system derived from the feedback analysis of the *HTF* matrix for variations of the R_{stab} resistor introduced in parallel (x) and the poles resulting from a conventional parametric stability analysis varying the R_{stab} resistor (+) for $P_{in} = 5\ dBm$.

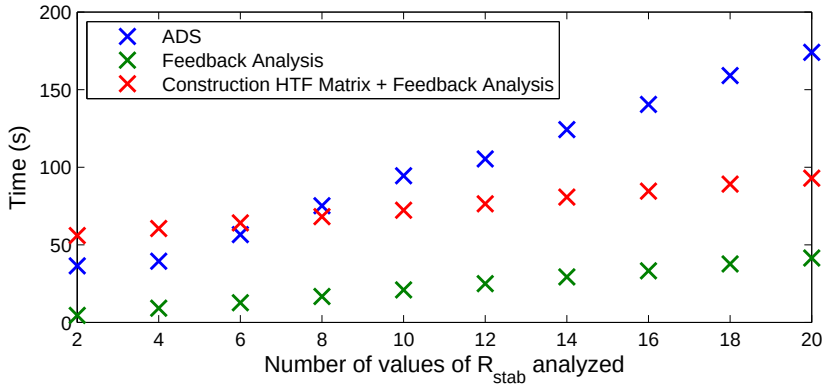

Figure 4.26: Run time versus number of values of the R_{stab} analyzed for the conventional parametric analysis of frequency responses obtained in *ADS* (blue), the feedback analysis (green) and the construction of the *HTF* matrix and the feedback analysis (red).

Due to the fact that the the amount of frequency responses ($NH = 4$) and frequency band analyzed ($[0,\ 4f_0]$) are high, the order of HTF matrix is consequently also high, $N(2NH+1) = 1782$. As a result, the calculation of the closed-loop system and its poles is not as immediate as in the previous example. However, as mentioned previously, this step can be optimized by not calculating all the poles of the closed-loop system but only a smaller set of poles centered around the frequency of the unstable poles.

If the run time to construct the HTF matrix is not taken into account (green curve in Figure 4.26), the large-signal stabilization method and tool proposed in this chapter is 9 times faster than the conventional strategy of simulating a parametric mixer-mode harmonic balance simulation in ADS (blue curve in Figure 4.26).

However, the construction of the HTF matrix is not negligible in this case. That is, if the time required to construct the HTF matrix is also taken into account (red curve in Figure 4.26), it is determined that a considerable time improvement is achieved with the proposed strategy if more that 7 values of R_{stab} are analyzed to determine the stabilization of the odd-mode instability of this amplifier.

4.7 Conclusions

In this chapter a generalization of the systematic small-signal stabilization methodology in [61] to the large-signal regime has been introduced.

Firstly, its validity has been demonstrated by calculating the analytical HTF matrix of a simple resonant circuit and applying a proportional control action to stabilize it.

Once the validity of the technique has been demonstrated, the formulation for the construction of the non-analytical HTF matrix has been introduced. This step is essential since the calculation of

the analytical *HTF* matrix is not realistic for real microwave circuits. An automatic software routine has been created for constructing the non-analytical *HTF* matrix from the impedance or admittance frequency responses simulated in *ADS*. Additionally, a strategy has been formulated to select the size of the *HTF* matrix from analyzing the magnitude curves of the H_k and H_{-k} frequency responses obtained in *ADS*.

Finally, the potential of the large-signal stabilization methodology based on the non-analytical *HTF* matrix has been demonstrated with two examples. As well as the robustness of the technique, the potentially fast execution time has been demonstrated.

Conclusions and Future Work

In this document the general stability analysis techniques for microwave power amplifiers have been briefly presented. Particularly, the stability analysis technique based in Single-Input Single-Output (SISO) pole-zero identification has been reviewed. It has been demonstrated that from identifying SISO closed-loop frequency responses of a microwave circuit and by analyzing the identified poles its small-signal and large-signal stability can be determined. However its two main limitations have also been discussed.

On the one hand, in order to obtain a SISO frequency response a single node or branch of the circuit must be selected. The instability will not be detected if the chosen observation port is isolated from the unstable feedback loop (loss of observability and controllability). On the other hand, the order of the transfer function to be fitted is *a priori* unknown and must be defined externally. Despite the reliability of existing automatic order selection algorithms, mathematical pole-zero quasi-compensations might appear if the selected final order is too high (overmodeling).

Consequently, a novel Multiple-Input Multiple-Output (MIMO) pole-zero stability analysis methodology and tool capable of reducing the mentioned limitations of the SISO pole-zero stability analysis technique has been created and its applicability has been demonstrated. This method consists of carrying out transfer function identifications of multiple small-signal or large-signal frequency responses of a same circuit whilst establishing the same set of poles for all of them.

The incorrect stability conclusions resulting from SISO identifications with lack of observability can be eliminated with the MIMO stability analysis since one can assume that the instability will be detected with high observability in at least one of the selected nodes. To further improve the chances of detecting instabilities, it is advised to select the input and outputs nodes of a transistor for each stage of a multistage amplifier. Additionally and along these lines, a new ρ factor, that represents a normalized residue, has been created for detecting the critical nodes of an amplifier. The creation of this new factor is based mainly on the idea that the residue associated to a pole will be considerably higher at the observation port with high observability.

Additional features have also been introduced to detect or avoid the apparition of mathematical pole-zero quasi-compensations results of overmodeling. An automatic order selection algorithm has been created that selects the order by reducing the phase error of the identification until a phase error tolerance introduced by the user is reached. Next, a novel representation consisting of plotting only the resonant poles has been proposed. Finally, it has been determined that the previously mentioned ρ factor, capable of detecting the critical nodes of a circuit, can also be used to detect overmodeling.

A X-band Doherty amplifier has been designed for a fundamental frequency of $f_0 = 10.95\,GHz$ and a bandwidth of 500 MHz. Additionally, the effectiveness of the MIMO stability analysis has been demonstrated since thanks to the MIMO stability analysis technique two small-signal instabilities have been detected and their critical nodes have been determined from calculating the ρ factor. After guaranteeing the small-signal and large-signal stability of the amplifier for variations of multiple parameters of the amplifier, an output power of $P_{out\_SAT} = 37.4\%dBm$ with a drain efficiency of $\mu_{SAT} = 61.7$ % in saturation have been achieved in simulation.

Finally, a systematic methodology for stabilization of large-signal instabilities of microwave circuits has been formulated. The values of

the stabilization networks required to stabilize an unstable design can be determined by considering the frequency responses at the multiple harmonics of the fundamental frequency, constructing the Harmonic Transfer Function (HTF) and applying classical control theory. It should be noted that the created MIMO stability analysis tool was indispensable to construct the HTF matrix.

In conclusion, a MIMO pole-zero stability analysis tool has been created and its potential has been demonstrated as it has been used to successfully design a stable X-band Doherty amplifier and it also has been used to create a systematic methodology for stabilization of large-signal instabilities in microwave circuits.

In the following paragraphs are some of the ideas that can be tackled in the future to improve the MIMO stability analysis and large-signal stabilization techniques that have been introduced are summarized.

- In [143] the appearance of spurious mathematical poles resulting from the convergence of identifying noisy responses is addressed and a new factor (μ) to identify and remove these spurious poles is defined. An interesting line of work would be to compare the potential of the ρ factor to detect overmodeling with the μ factor described in [143].

- The propagation in voltage must be taken into account when analyzing multiple voltage-voltage frequency responses of multistage power amplifier. For example, even if the instability is generated at a second stage of a multistage amplifier, due to the voltage propagation it might be detected with high precision also in the following stages. Consequently, the residue of the unstable poles might be high at the second stage and also at the later stages. Therefore, a new ρ factor capable of detecting the critical node from voltage-voltage frequency responses should be created.

- When constructing the *HTF* matrix, the MIMO identification of a high number of frequency responses and large frequency bands often implies high identification orders (N). Consequently, most of the times mathematical poles that have no considerable effect on any of the frequency responses are identified. It would be interesting to test if the elimination the poles of the *HTF* matrix with excessively low ρ factors can improve the speed of the feedback calculus and further improve the large-signal stabilization technique.

- In [61], the optimal location for stabilization of small-signal instabilities is determined from analyzing the zeros of the identified transfer function. Future work could consist of analyzing the zeros of the *HTF* matrix and the zeros the transfer functions of the multiple sidebands in order to determine if additional information can be obtained regarding the controllability of large-signal instabilities.

Publications

International Journals

[1] J.M. Collantes, **L. Mori**, A. Anakabe, N. Otegi, N. Ayllon, F. Ramirez, V. Armengaud, G. Soubercaze-Pun, "Recent Advances in Pole-Zero Identification: Unveiling the Critical Dynamics of Microwave Circuits," *IEEE Microw. Mag.*. **PENDING PUBLICATION**

[2] J.M. Gonzalez, N. Otegi, A. Anakabe, **L. Mori**, A. Barcenilla, J.M. Collantes, "In-circuit Characterization of Low-frequency Stability Margins in Power Amplifiers", *IEEE Trans. on Microw. Theory and Techn.*. **PENDING PUBLICATION**

International Conferences

[3] **L. Mori**, A. Anakabe, I. Lizarraga, N. Otegi, J.M. Collantes, V. Armengaud, G. Soubercaze-Pun, "Stability analysis of multistage power amplifiers using Multiple-Input Multiple-Output identification," *IEEE MTT-S Int. Microw. Symp. Dig.*, San Francisco, CA, 2016, pp. 1-4.

- Mentioned in article:

  R. K. Gupta, "Industry Best Papers Recognized at IMS2016, San Francisco [MTT-S Society News]," *IEEE Microw. Mag.*, vol. 17, no. 10, pp. 83-86, Oct. 2016.

[4] S. Dellier, **L. Mori**, J.M. Collantes, A. Anakabe and C. Campbell, “Analysis of odd-mode parametric instabilities at fundamental frequency in an X-band MMIC Power Amplifier," *IEEE Compd. Semicond. Integr. Circuit Symp.*, Austin, TX, USA, 2016, pp. 1-4.

[5] J.M. Collantes, N. Otegi, A. Anakabe, **L. Mori**, A. Barcenilla, J.M. Gonzalez, “Detecting Critical Resonances in Microwave Amplifiers through Noise Simulations," *IEEE MTT-S Latin Amer. Microw. Conf.(LAMC)*, Arequipa, Peru, 2018. **PENDING PUBLICATION**

Bibliography

[1] A. Suárez and R. Quere, *Stability Analysis of Nonlinear Microwave Circuits*. Norwood, MA, USA: Artech House, Inc., 2 ed., 2003.

[2] A. Costantini, G. Vannini, F. Filicori, and A. Santarelli, "Stability Analysis of Multi-Transistor Microwave Power Amplifiers," in *Gall. Arsenide Appl. Symp. Tech. Dig.*, (Paris, France), pp. 342–345, IEEE, Oct. 2000.

[3] A. Collado, F. Ramírez, and A. Suárez, "Analysis and Stabilization Tools for Microwave Amplifiers," in *IEEE MTT-S Int. Microw. Symp. Dig.*, (Fort Worth, TX, USA), pp. 945–948, June 2004.

[4] A. Suárez, *Analysis and Design of Autonomous Microwave Circuits*. Hoboken, NJ, USA: John Wiley & Sons, 1 ed., 2009.

[5] A. Suárez, "Check the Stability: Stability Analysis Methods for Microwave Circuits," *IEEE Microw. Mag.*, vol. 16, no. 5, pp. 69–90, 2015.

[6] M. Soulard, M. Delmond, J. L. Cazaux, Y. Butel, E. Laporte, J. C. Sarkissian, and J. F. Villemazet, "Evolution and Recent Development in MMIC's for Space Application," in *Proc. 2nd Int. Conf. Microw. Millim. Wave Technol. Conf.*, (Beijing, China), pp. 219–222, IEEE, Sept. 2000.

[7] R. G. Freitag, S. H. Lee, and D. M. Krafcsif, "Stability and Improved Circuit Modeling Considerations for High MMIC Amplifiers," in *IEEE Microw. Millimeter-Wave Monolith. Circuits Symp.*, (New York, NY, USA), pp. 125–128, IEEE, May 1988.

[8] A. Anakabe, J. M. Collantes, J. Portilla, J. Jugo, A. Mallet, L. Lapierre, and J. P. Fraysse, "Analysis and Elimination of Parametric Oscillations in Monolithic Power Amplifiers," in *IEEE MTT-S Int. Microw. Symp. Dig.*, (Seattle, WA), pp. 2181–2184, June 2002.

[9] N. Ayllon, J. M. Collantes, A. Anakabe, G. Soubercaze-Pun, S. Forestier, and D. Langrez, "Joint RF and Large-Signal Stability Optimization of MMIC Power Combining Amplifiers," *Int. J. Microw. Wirel. Technol.*, vol. 5, no. 6, pp. 683–688, 2013.

[10] M. B. Steer, C. R. Chang, and G. W. Rhyne, "Computer Aided Analysis of Nonlinear Microwave Circuits Using Frequency Domain Nonlinear Analysis Techniques: The State of the Art," *Int. J. RF Microw. Comput. Eng.*, vol. 1, no. 2, pp. 181–200, 1991.

[11] M. B. Steer, J. W. Bandler, and C. M. Snowden, "Computer Aided Design of RF and Microwave Circuits and Systems," *IEEE Trans. Microw. Theory Tech.*, vol. 50, no. 3, pp. 996–1005, 2002.

[12] V. Rizzoli and A. Neri, "State of the Art and Present Trends in Nonlinear Microwave CAD Techniques," *IEEE Trans. Microw. Theory Tech.*, vol. 36, no. 2, pp. 343–365, 1988.

[13] M. S. Nakhla and J. Vlach, "A Piecewise Harmonic Balance Technique for Determination of Periodic Response of Nonlinear Systems," *IEEE Trans. Circuits Syst.*, vol. 23, no. 2, pp. 85–91, 1976.

[14] R. J. Gilmore and M. B. Steer, "Nonlinear Circuit Analysis Using the Method of Harmonic Balance - A Review of the Art," *Int. J. Microw. Milimeter-Wave Comput. Des.*, vol. 1, no. 1, pp. 22–37, 1991.

[15] S. Sastry, *Nonlinear Systems: Analysis, Stability and Control*. New York, NY, USA: Springer-Verlag, 1 ed., 1999.

[16] J. M. Rollett, "Stability and Power-Gain Invariants of Linear Twoports," *IRE Trans. Circuit Theory*, vol. 9, no. 1, pp. 29–32, 1962.

[17] M. Ohtomo, "Proviso on the Unconditional Stability Criteria for Linear Twoport," *IEEE Trans. Microw. Theory Tech.*, vol. 43, no. 5, pp. 1197–1200, 1995.

[18] R. W. Jackson, "Rollett Proviso in the Stability of Linear Microwave Circuits - A Tutorial," *IEEE Trans. Microw. Theory Tech.*, vol. 54, no. 3, pp. 993–1000, 2006.

[19] D. Woods, "Reappraisal of the Unconditional Stability Criteria for Active 2-Port Networks in Terms of S Parameters," *IEEE Trans. Circuits Syst.*, vol. 23, no. 2, pp. 73–81, 1976.

[20] A. Platzker, W. Struble, and K. T. Hetzler, "Instabilities Diagnosis and the Role of K in Microwave Circuits," in *IEEE MTT-S Int. Microw. Symp. Dig.*, (Atlanta, GA, USA), pp. 1185–1188, IEEE, June 1993.

[21] W. Struble and A. Platzker, "A Rigorous Yet Simple Method for Determiming Stability of Linear N-Port Networks," in *15th Gall. Arsenide Integr. Circuit Symp. Tech. Dig.*, (San Jose, CA, USA), pp. 251–254, IEEE, Oct. 1993.

[22] T. Närhi and M. Valtonen, "Stability Envelope - New Tool for Generalised Stability Analysis," in *IEEE MTT-S Int. Microw. Symp. Dig.*, (Denver, CO, USA), pp. 623–626, IEEE, June 1997.

[23] M. L. Edwards and J. H. Sinsky, "A New Criterion for Linear 2-Port Stability Using a Single Geometrically Derived Parameter," *IEEE Trans. Microw. Theory Tech.*, vol. 40, no. 12, pp. 2303–2311, 1992.

[24] C. Barquinero, A. Suárez, A. Herrera, and J. L. García, "Complete Stability Analysis of Multifunction MMIC Circuits," *IEEE Trans. Microw. Theory Tech.*, vol. 55, no. 10, pp. 2024–2033, 2007.

[25] P. D. L. Abrie, *Design of RF and Microwave Amplifiers and Oscillators*. Norwood, MA, USA: Artech House, Inc., 2 ed., 2009.

[26] R. D. Martinez and R. C. Compton, "A General Approach for S-Parameter Design of Oscillators with 1 and 2-Port Active Devices," *IEEE Trans. Microw. Theory Tech.*, vol. 40, no. 3, pp. 569–574, 1992.

[27] R. W. Jackson, "Criteria for the Onset of Oscillation in Microwave Circuits," *IEEE Trans. Microw. Theory Tech.*, vol. 40, no. 3, pp. 566–569, 1992.

[28] G. Gonzalez, *Foundations of Oscillator Circuit Design*. Boston, MA, USA: Artech House, Inc., 2006.

[29] M. Ohtomo, "Stability Analysis and Numerical Simulation of Multidevice Amplifiers," *IEEE Trans. Microw. Theory Tech.*, vol. 41, no. 617, pp. 983–991, 1993.

[30] S. Colangeli, R. Giofre, W. Ciccognani, and E. Limiti, "A Simple Test to Check the Inherent-Stability Proviso on Field-Effect Transistors," *IEEE Access*, vol. 6, pp. 43079–43087, 2018.

[31] D. M. Pozar, *Microwave Engineering*. Danvers, MA, USA: John Wiley & Sons, 4 ed., 2012.

[32] S. Colangeli, W. Ciccognani, M. Palomba, and E. Limiti, "Verifying Rollett's proviso on active devices under arbitrary passive embeddings," *IEEE Trans. Circuits Syst. II Express Briefs*, vol. 64, no. 8, pp. 932–936, 2017.

[33] S. Skogestad and I. Postlethwaite, *Multivariable Feedback Control: Analysis and Design.* New York, NY, USA: John Wiley & Sons, 1996.

[34] V. Rizzoli and A. Lipparini, "General Stability Analysis of Periodic Steady-State Regimes in Nonlinear Microwave Circuits," *IEEE Trans. Microw. Theory Tech.*, vol. 33, no. 1, pp. 30–37, 1985.

[35] H. Nyquist, "Regeneration Theory," *Bell Syst. Tech. J.*, vol. 11, no. 1, pp. 126–147, 1932.

[36] R. Quéré, E. Ngoya, M. Camiade, M. Hessane, and J. Obregon, "Large Signal Design of Broadband Monolithic Microwave Freauency Dividers and Phase-Locked Oscillators," *IEEE Trans. Microw. Theory Tech.*, vol. 41, no. 11, pp. 1928–1938, 1993.

[37] A. Suárez and J. M. Collantes, "A new Technique for Chaos Prediction in RF Circuit Design Using Harmonic-Balance Commercial Simulators," *IEEE Trans. Circuit Syst. I.*, vol. 46, no. 11, pp. 1413–1415, 1999.

[38] J. M. Collantes and A. Suárez, "Period-Doubling Analysis and Chaos Detection Using Commercial Harmonic Balance Simulators," *IEEE Trans. Microw. Theory Tech.*, vol. 48, no. 4, pp. 574–581, 2000.

[39] A. Suárez, J. Morales, and R. Quéré, "Chaos Prediction in an MMIC Frequency Divider in Millimetric Band," *IEEE Microw. Guid. Wave Lett.*, vol. 8, no. 1, pp. 21–23, 1998.

[40] S. Mons, J. C. Nallatamby, R. Quere, P. Savary, and J. Obregon, "A Unified Approach for the Linear and Nonlinear Stability Analysis of Microwave Circuits Using Commercially Available Tools," *IEEE Trans. Microw. Theory Tech.*, vol. 47, no. 12, pp. 2403–2409, 1999.

[41] P. Bolcato, J. C. Nallatamby, C. Rumolo, R. Larcheveque, M. Prigent, and J. Obregon, "Efficient Algorithm for Steady-State Stability Analysis of Large Analog/RF Circuits," in *IEEE MTT-S Int. Microw. Symp. Dig.*, (Phoenix, AZ, USA), pp. 7–10, May 2001.

[42] G. Leuzzi and F. Di Paolo, "Bifurcation Synthesis by means of Harmonic Balance and Conversion Matrix," in *Proc. Eur. Gall. Arsenide Appl. Symp.*, (Munich, Germany), pp. 521–524, Oct. 2003.

[43] A. Suárez, S. Jeon, and D. B. Rutledge, "Stability Analysis and Stabilization of Power Amplifiers," *IEEE Microw. Mag.*, vol. 7, no. 5, pp. 51–65, 2006.

[44] F. Ramírez, A. Suárez, I. Lizarraga, and J. M. Collantes, "Stability Analysis of Nonlinear Circuits Driven with Modulated Signals," *IEEE Trans. Microw. Theory Tech.*, vol. 58, no. 4, pp. 37–42, 2010.

[45] F. Cappelluti, F. L. Traversa, F. Bonani, S. D. Guerrieri, and G. Ghione, "Large-Signal Stability of Symmetric Multibranch Power Amplifiers Exploiting Floquet Analysis," *IEEE Trans. Microw. Theory Tech.*, vol. 61, no. 4, pp. 1580–1587, 2013.

[46] A. Suárez, F. Ramírez, and S. Sancho, "Stability Analysis of Power Amplifiers Under Mismatching Effects," in *IEEE MTT-S Int. Microw. Symp. Dig.*, (Seatle, WA, USA), pp. 13–15, IEEE, June 2013.

[47] A. Suárez, F. Ramírez, and S. Sancho, "Stability Analysis of Power Amplifiers Under Output Mismatch Effects," *IEEE Trans. Microw. Theory Tech.*, vol. 62, no. 10, pp. 2273–2289, 2014.

[48] A. Suárez, F. Ramírez, and S. Sancho, "Stability Criteria for Power Amplifiers Under Mismatch Effects," in *IEEE MTT-S Int. Microw. Symp.*, (Phoenix, AZ, USA), pp. 2–5, May 2015.

[49] F. Ramírez, S. Sancho, and A. Suárez, "Oscillation Modes in Multiresonant Oscillator Circuits," *IEEE Trans. Microw. Theory Tech.*, vol. 64, no. 12, pp. 4660–4675, 2016.

[50] A. Suárez, F. Ramírez, and S. Sancho, "Prediction of Odd-Mode Instabilities Under Output Mismatch Effects," *Int. J. Microw. Wirel. Technol.*, vol. 9, no. 6, pp. 1305–1315, 2017.

[51] A. Suárez, M. Pontón, S. Sancho, and F. Ramírez, "Analysis of Output Loading Effects in Autonomous Circuits," *IEEE Trans. Microw. Theory Tech.*, vol. 65, no. 9, pp. 3135–3146, 2017.

[52] V. Iglesias, A. Suárez, and J. L. García, "New Technique for the Determination Through Commercial Software of the Stable-Operation Parameter Ranges in Nonlinear Microwave Circuits," *IEEE Microw. Guid. Wave Lett.*, vol. 8, no. 12, pp. 424–426, 1998.

[53] J. Jugo, J. Portilla, A. Anakabe, A. Suárez, and J. M. Collantes, "Closed-Loop Stability Analysis of Microwave Amplifiers," *Electron. Lett.*, vol. 37, no. 4, pp. 226–228, 2001.

[54] J. M. Collantes, I. Lizarraga, A. Anakabe, and J. Jugo, "Stability Verification of Microwave Circuits Through Floquet Multiplier Analysis," in *Proc. IEEE Asia-Pacific Circuits Sytems*, (Taiwan), pp. 997–1000, Apr. 2004.

[55] A. Anakabe, *Detección y Eliminación de Inestabilidades Paramétricas en Amplificadores de Potencia para Radiocomunicaciones.* PhD thesis, University of the Basque Country (UPV/EHU), 2004.

[56] F. Bonani and M. Gilli, "Analysis of Stability and Bifurcations of Limit Cycles in Chua's Circuit Through the Harmonic-Balance Approach," *IEEE Trans. Circuits Syst. I.*, vol. 46, no. 8, pp. 881–890, 1999.

[57] S. Jeon, A. Suárez, and D. B. Rutledge, "Analysis and Elimination of Hysteresis and Noisy Precursors in Power Amplifiers," *IEEE Trans. Microw. Theory Tech.*, vol. 54, no. 3, pp. 1096–1106, 2006.

[58] A. Suárez and F. Ramírez, "Detailed Investigation of Fundamental Instability Mechanisms in Power Amplifiers," in *Proc. Asia Pacific Microw. Conf.*, (Sendai, Japan), pp. 3–5, Nov. 2014.

[59] "https://www.keysight.com/en/pc-1297113/advanced-design-system-ads?cc=ES&lc=eng."

[60] "http://www.awrcorp.com/products/ni-awr-design-environment/microwave-office."

[61] N. Ayllon, J. M. Collantes, A. Anakabe, I. Lizarraga, G. Soubercaze-Pun, and S. Forestier, "Systematic Approach to the Stabilization of Multitransistor Circuits," *IEEE Trans. Microw. Theory Tech.*, vol. 59, no. 8, pp. 2073–2082, 2011.

[62] "https://www.maurymw.com/MW_RF/Stability_Analysis.php."

[63] "https://cnes.fr/fr."

[64] "http://www.amcad-engineering.com/."

[65] A. Anakabe, S. Mons, T. Gasseling, P. Casas, R. Quere, J. M. Collantes, and A. Mallet, "Efficient Nonlinear Stability Analysis of Microwave Circuits Using Commercially Available Tools," in *32nd Eur. Microw. Conf.*, (Milan, Italy), pp. 1–5, IEEE, Sept. 2002.

[66] A. Anakabe, N. Ayllon, J. M. Collantes, A. Mallet, and K. Narendra, "Automatic Pole-Zero Identification for Multivariable Large-Signal Stability Analysis of RF and Microwave Circuits," in *40th Eur. Microw. Conf.*, (Paris, France), pp. 477–480, Sept. 2010.

[67] N. Ayllon, *Développement des Méthodes de Stabilisation pour la Conception des Circuits Hyperfréquences: Application à l'Optimisation d'un Amplificateur de Puissance Spatial*. PhD thesis, University of the Basque Country (UPV/EHU), 2011.

[68] S. Dellier, R. Gourseyrol, J. M. Collantes, A. Anakabe, G. Soubercaze-Pun, and K. Narendra, "Stability Analysis of Microwave Circuits," in *Wirel. Microw. Technol. Conf.*, (Cocoa Beach, FL, USA), pp. 1–5, IEEE, Apr. 2012.

[69] S. Dellier, "Software Simplifies Stability Analysis," *Microwaves RF Mag.*, no. August, pp. 1–5, 2012.

[70] A. Mallet, A. Anakabe, G. Soubercaze-Pun, and J. M. Collantes, "Automation of the Zero-Pole Identification Methods for the Stability Analysis of Microwave Active Circuits," 2011.

[71] J. De Cos, A. Suárez, and F. Ramírez, "Analysis of Oscillation Modes in Free-Running Ring Oscillators," *IEEE Trans. Microw. Theory Tech.*, vol. 60, no. 10, pp. 3137–3150, 2012.

[72] J. M. Collantes, N. Otegi, A. Anakabe, N. Ayllon, A. Mallet, and G. Soubercaze-Pun, "Monte-Carlo Stability Analysis of Microwave Amplifiers," in *IEEE 12th Annu. Wirel. Microw. Technol. Conf.*, (Clearwater Beach, FL, USA), pp. 1–6, IEEE, June 2011.

[73] N. Otegi, A. Anakabe, J. Pelaz, J. M. Collantes, and G. Soubercaze-Pun, "Increasing Low-Frequency Stability Margins in Microwave Amplifiers from Experimental Data," in *IEEE MTT-S Int. Microw. Symp. Dig.*, (Montreal, Canada), pp. 31–33, IEEE, June 2012.

[74] N. Otegi, A. Anakabe, J. Pelaz, J. M. Collantes, and G. Soubercaze-Pun, "Experimental Characterization of Stability Margins in Microwave Amplifiers," *IEEE Trans. Microw. Theory Tech.*, vol. 60, no. 12, pp. 4145–4156, 2012.

[75] J. Pelaz, J. M. Collantes, N. Otegi, A. Anakabe, and G. Collins, "Combined Control of Drain Video Bandwidth and Stability Margins in Power Amplifiers for Envelope Tracking Applications," in *IEEE MTT-S Int. Microw. Symp.*, (Tampa, FL, USA), pp. 1–4, IEEE, June 2014.

[76] J. Pelaz, J. M. Collantes, N. Otegi, A. Anakabe, and G. Collins, "Experimental Control and Design of Low-Frequency Bias Networks for Dynamically Biased Amplifiers," *IEEE Trans. Microw. Theory Tech.*, vol. 63, no. 6, pp. 1923–1936, 2015.

[77] S. A. Maas, *Nonlinear microave and RF circuits*. Norwood, MA, USA: Artech House, Inc., 2003.

[78] A. Anakabe, J. M. Collantes, J. Portilla, S. Mons, and A. Mallet, "Detecting and Avoiding Odd-Mode Parametric Oscillations in Microwave Power Amplifiers," *Int. J. RF Microw. Comput. Eng.*, vol. 15, no. 5, pp. 469–478, 2005.

[79] N. Ayllon, A. Anakabe, J. M. Collantes, G. Soubercaze-Pun, and S. Forestier, "Sensitivity Enhancement in Pole-Zero Identification Based Stability Analysis of Microwave Circuits," in *Integr. Nonlinear Microw. Millimetre-Wave Circuits*, (Malaga, Spain), pp. 75–78, Nov. 2008.

[80] R. Pintelon and J. Schoukens, *System Identification: A Frequency Domain Approach*. New York, NY, USA: Wiley-IEEE Press, 2 ed., 2012.

[81] L. Ljung, *System Identification: Theory of the User*. Englewood Cliffs, NJ, USA: Prentice Hall, Inc., 1987.

[82] W. R. Evans, "Control System Synthesis by Root Locus Method," *Trans. Am. Inst. Electr. Eng.*, vol. 69, no. 1, pp. 66–69, 1950.

[83] B. C. Kuo, *Automatic Control Systems*. New Delhi, India: Prentice Hall, 7 ed., 1995.

[84] "https://es.mathworks.com/products/matlab.html."

[85] B. Gustavsen and A. Semlyen, "Rational Approximation of Frequency Domain Responses by Vector Fitting," *IEEE Trans. Power Deliv.*, vol. 14, no. 3, pp. 1052–1061, 1999.

[86] A. Semlyen and B. Gustavsen, "Vector Fitting by Pole Relocation for the State Equation Approximation of Nonrational Transfer Matrices," *Circuits, Syst. Signal Process.*, vol. 19, no. 6, pp. 549–566, 2000.

[87] B. Gustavsen, "Improving the Pole Relocating Properties of Vector Fitting," *IEEE Trans. Power Deliv.*, vol. 21, no. 3, pp. 1587–1592, 2006.

[88] D. Deschrijver, M. Mrozowski, T. Dhaene, and D. De Zutter, "Macromodeling of Multiport Systems Using a Fast Implementation of the Vector Fitting Method," *IEEE Microw. Wirel. Components Lett.*, vol. 18, no. 6, pp. 383–385, 2008.

[89] "http://www.sintef.no/projectweb/vectfit."

[90] J. Roychowdhury, "Reduced-Order Modelling of Linear Time-Varying Systems," in *Proc. IEEE/ACM Int. Comput. Des. Conf.*, (San Jose, CA, USA), pp. 92–95, Nov. 1998.

[91] A. Anakabe, J. M. Collantes, J. Portilla, S. Mons, A. Mallet, and L. Lapierre, "Analysis of Odd-Mode Parametric Oscillations in HBT Multi-Stage Power Amplifiers," in *Eur. Microw. Week - 11th GaAs Symp.*, (Munich, Germany), pp. 533–536, Oct. 2003.

[92] S. C. Cripps, *RF Power Amplifiers for Wireless Communications*. Norwood, MA, USA: Artech House, Inc., 1999.

[93] P. M. Lavrador, T. R. Cunha, P. M. Cabral, and J. C. Pedro, "The Linearity-Efficiency Compromise," *IEEE Microw. Mag.*, vol. 11, no. 5, pp. 44–58, 2010.

[94] F. H. Raab, P. Asbeck, S. C. Cripps, P. B. Kenington, Z. B. Popovic, N. Pothecary, J. F. Sevic, and N. O. Sokal, "Power Amplifiers and Transmitters for RF and Microwave," *IEEE Trans. Microw. Theory Tech.*, vol. 50, no. 3, pp. 814–826, 2002.

[95] W. H. Doherty, "A New High Efficiency Power Amplifier for Modulated Waves," *Proc. Inst. Radio Eng.*, vol. 24, no. 9, pp. 1163–1182, 1936.

[96] H. Chireix, "High Power Outphasing Modulation," *Proc. Inst. Radio Eng.*, vol. 23, no. 11, pp. 1370–1392, 1935.

[97] L. Kahn, "Single-Sideband Transmission by Envelope Elimination and Restoration," *Proc. IRE*, vol. 40, no. 7, pp. 803–806, 1952.

[98] V. Camarchia, M. Pirola, and R. Quaglia, "The Doherty Power Amplifier: Review of Recent Solutions and Trends," *IEEE Trans. Microw. Theory Tech.*, vol. 63, no. 2, pp. 559–571, 2015.

[99] R. Pengelly, C. Fager, and M. Özen, "Doherty's Legacy: A History of the Doherty Power Amplifier from 1936 to the Present Day," *IEEE Microw. Mag.*, vol. 17, no. 2, pp. 41–58, 2016.

[100] S. C. Cripps, *Advanced Techniques in RF Power Amplifier Design*. Norwood, MA, USA: Artech House, Inc., 2002.

[101] J. Kim, J. Cha, I. Kim, and B. Kim, "Optimum Operation of Asymmetrical-Cells-Based Linear Doherty Power Amplifiers - Uneven Power Drive and Power Matching," *IEEE Trans. Microw. Theory Tech.*, vol. 53, no. 5, pp. 1802–1809, 2005.

[102] J. Lee, J. Kim, J. Kim, K. Cho, and S. P. Stapleton, "A High Power Asymmetric Doherty Amplifier with Improved Linear Dynamic Range," in *IEEE MTT-S Int. Microw. Symp. Dig.*, (San Francisco, CA, USA), pp. 1348–1351, June 2006.

[103] J. Kim, B. Fehri, S. Boumaiza, and J. Wood, "Power Efficiency and Linearity Enhancement Using Optimized Asymmetrical Doherty Power Amplifiers," *IEEE Trans. Microw. Theory Tech.*, vol. 59, no. 2, pp. 425–434, 2011.

[104] M. Coffey, P. Momenroodaki, A. Zai, and Z. Popovic, "A 4.2-W 10-GHz GaN MMIC Doherty Power Amplifier," in *IEEE Compd. Semicond. Integr. Circuit Symp.*, (New Orleans, LA, USA), pp. 1–4, Oct. 2015.

[105] C. H. Kim and B. Park, "Fully-Integrated Two-Stage GaN MMIC Doherty," *IEEE Microw. Wirel. Components Lett.*, vol. 26, no. 11, pp. 918–920, 2016.

[106] C. Steinbeiser, P. Page, T. Landon, and G. Burgin, "Doherty Power Amplifiers using 2nd Generation HVHBT Technology for High Efficiency Basestation Applications," in *IEEE Compd. Semicond. Integr. Circuit Symp.*, (Monterey, CA, USA), pp. 1–4, Oct. 2010.

[107] Y. Yang, J. Cha, B. Shin, and B. Kim, "A Fully Matched N -Way Doherty Amplifier," *IEEE Trans. Microw. Theory Tech.*, vol. 51, no. 3, pp. 986–993, 2003.

[108] K. Cho, J. Kim, and S. P. Stapleton, "A Highly Efficient Doherty Feedforward Linear Power Amplifier for W-CDMA Base-Station Applications," *IEEE Trans. Microw. Theory Tech.*, vol. 53, no. 1, pp. 292–300, 2005.

[109] R. Quaglia, M. Pirola, C. Ramella, and S. Member, "Offset Lines in Doherty Power Amplifiers: Analytical Demonstration and Design," *IEEE Microw. Wirel. Components Lett.*, vol. 23, no. 2, pp. 93–95, 2013.

[110] N. Srirattana, A. Raghavan, D. Heo, P. E. Allen, and J. Laskar, "Analysis and Design of a High-Efficiency Multistage Doherty Power Amplifier for WCDMA," *IEEE Trans. Microw. Theory Tech.*, vol. 53, no. 3, pp. 852–860, 2005.

[111] A. Grebennikov, "A High-Efficiency 100-W Four-Stage Doherty GaN HEMT Power Amplifier Module for WCDMA Systems," in *IEEE MTT-S Int. Microw. Symp.*, (Baltimore, MD, USA), pp. 48–51, 2011.

[112] R. Giofré and P. Colantonio, "A High Efficiency and Low Distortion 6 W GaN MMIC Doherty Amplifier for 7 GHz Radio Links," *IEEE Microw. Wirel. Components Lett.*, vol. 27, no. 1, pp. 70–72, 2017.

[113] H. H. Ladhani, J. K. Jones, and G. Bouisse, "Improvements in the Instantaneous-Bandwidth Capability of RF Power Transistors Using In-Package High-k Capacitors," in *IEEE MTT-S Int. Microw. Symp.*, (Baltimore, MD, USA), pp. 3–6, June 2011.

[114] G. Sun and R. H. Jansen, "Broadband Doherty power amplifier via real frequency technique," *IEEE Trans. Microw. Theory Tech.*, vol. 60, no. 1, pp. 99–111, 2012.

[115] R. Giofré, L. Piazzon, P. Colantonio, and F. Giannini, "A Doherty Architecture with High Feasibility and Defined Bandwidth Behavior," *IEEE Trans. Microw. Theory Tech.*, vol. 61, no. 9, pp. 3308–3317, 2013.

[116] D. Gustafsson, C. M. Andersson, and C. Fager, "A Modified Doherty Power Amplifier with Extended Bandwidth and Reconfigurable Efficiency," *IEEE Trans. Microw. Theory Tech.*, vol. 61, no. 1, pp. 533–542, 2013.

[117] D. Gustafsson, *Extending the Bandwidth of the Doherty Power Amplifier*. PhD thesis, Chalmers University of Technology, 2014.

[118] C. H. Kim, S. Jee, G. Jo, K. Lee, and B. Kim, "A 2.14-GHz GaN MMIC Doherty Power Amplifier for Small-Cell Base Stations," *IEEE Microw. Wirel. Components Lett.*, vol. 24, no. 4, pp. 263–265, 2014.

[119] Y. Park, J. Lee, S. Jee, S. Kim, C. Kim, B. Park, and B. Kim, "GaN HEMT MMIC Doherty Power Amplifier," *IEEE Microw. Wirel. Components Lett.*, vol. 25, no. 3, pp. 187–189, 2015.

[120] W. Shi, S. He, F. You, H. Xie, G. Naah, Q. Liu, and Q. Li, "The Influence of the Output Impedances of Peaking Power Amplifier on Broadband Doherty Amplifiers," *IEEE Trans. Microw. Theory Tech.*, vol. 65, no. 8, pp. 3002–3013, 2017.

[121] J. Lange, "Interdigitated Stripline Quadrature Hybrid," *IEEE Trans. Microw. Theory Tech.*, vol. 17, no. 12, pp. 1150–1151, 1969.

[122] S. Dellier, L. Mori, J. M. Collantes, A. Anakabe, and C. F. Campbell, "Analysis of Odd-Mode Parametric Instabilities at Fundamental Frequency in an X-band MMIC Power Amplifier," in *IEEE Compd. Semicond. Integr. Circuit Symp.*, (Austin, TX, USA), pp. 1–4, Oct. 2016.

[123] C. F. Campbell, "A Fully Integrated Ku-Band Doherty Amplifier MMIC," *IEEE Microw. Guid. Wave Lett.*, vol. 9, no. 3, pp. 114–116, 1999.

[124] C. F. Campbell, K. Tran, M. Y. Kao, and S. Nayak, "A K-Band 5W Doherty Amplifier MMIC Utilizing 0.15μm GaN on SiC HEMT Technology," in *IEEE Compd. Semicond. Integr. Circuit Symp.*, (La Jolla, CA, USA), pp. 1–4, Oct. 2012.

[125] R. Quaglia, V. Camarchia, T. Jiang, M. Pirola, S. Donati Guerrieri, and B. Loran, "K-Band GaAs MMIC Doherty Power Amplifier for Microwave Radio with Optimized Driver," *IEEE Trans. Microw. Theory Tech.*, vol. 62, no. 11, pp. 2518–2525, 2014.

[126] R. Quaglia, V. Camarchia, J. J. Moreno Rubio, M. Pirola, and G. Ghione, "A 4-W Doherty Power Amplifier in GaN MMIC Technology for 15-GHz Applications," *IEEE Microw. Wirel. Components Lett.*, vol. 27, no. 4, pp. 365–367, 2017.

[127] N. M. Wereley and S. R. Hall, "Frequency Response of Linear Time Periodic Systems," in *IEEE Conf. Decis. Control*, (Honolulu, HI, USA), pp. 3650–3655, IEEE, dec 1990.

[128] N. M. Wereley, *Analysis and Control of Linear Periodically Time Varying Systems*. PhD thesis, Massachusetts Institute of Technology, 1991.

[129] N. M. Wereley and S. R. Hall, "Linear Time Periodic Systems: Transfer Function, Poles, Transmission Zeroes and Directional Properties," in *Proc. Am. Control Conf.*, (Boston, MA, USA), pp. 1179–1184, Mar. 1991.

[130] P. Vanassche, G. Gielen, and W. Sansen, *Systematic Modeling and Analysis of Telecom Frontends and Their Building Blocks*. Dordrecth, The Netherlands: Springer, 1 ed., 2005.

[131] S. Hwang, *Frequency Domain System Identification of Helicopter Rotor Dynamics Incorporating Models with Time Periodic Coefficients*. PhD thesis, University of Maryland at College Park, 1997.

[132] A. Siddiqi, *Identification of the Harmonic Transfer Functions of a Helicopter Rotor*. PhD thesis, Massachusetts Institute of Technology, 2001.

[133] J. B. Maurice, R. Farolfi, F. Saupe, F. A. King, and W. Fichter, "Robust Stability Analysis of a Linear Time-Periodic Active Helicopter Rotor," *J. Guid. Control*, vol. 35, no. 5, pp. 1625–1636, 2012.

[134] T. P. Sim, P. Y. Li, and D. Lee, "Functions of a Xerographic Printing Process," *IEEE Trans. Control Syst. Technol.*, vol. 15, no. 2, pp. 349–357, 2007.

[135] R. Riva, S. Cacciola, and C. L. Bottasso, "Periodic Stability Analysis of Wind Turbines Operating in Turbulent Wind Conditions," *Wind Energy Sci.*, vol. 1, no. 2, pp. 177–203, 2016.

[136] U. Vargas and A. Ramirez, "Extended Harmonic Domain Model of a Wind Turbine Generator for Harmonic Transient Analysis," *IEEE Trans. Power Deliv.*, vol. 31, no. 3, pp. 1360–1368, 2016.

[137] E. Guest, K. H. Jensen, and T. W. Rasmussen, "Sequence Domain Harmonic Modeling of Type-IV Wind Turbines," *IEEE Trans. Power Electron.*, vol. 33, no. 6, pp. 4934–4943, 2018.

[138] H. Sandberg and E. Mollerstedt, "Harmonic modeling of the motor side of an inverter locomotive," in *Proc. 2000 IEEE Int. Conf. Control Appl.*, (Anchorage, AK, USA), pp. 918–923, Sept. 2000.

[139] E. Möllerstedt and B. Bernhardsson, "Out of Control Because of Harmonics," *IEEE Control Syst. Mag.*, vol. 20, no. 4, pp. 70–81, 2000.

[140] H. Sandberg, *Model Reduction for Linear Time-Varying Systems*. PhD thesis, Lund Institute of Technology (LTH), 2004.

[141] E. Louarroudi, R. Pintelon, J. Lataire, and G. Vandersteen, "Estimation of nonparametric harmonic transfer functions for linear periodically time-varying systems using periodic excitations," in *IEEE Instrum. Meas. Technol. Conf.*, (Binjiang, China), pp. 699–704, May 2011.

[142] "https://www.mathworks.com/products/curvefitting.html."

[143] S. Grivet-Talocia and M. Bandinu, "Improving the Convergence of Vector Fitting for Equivalent Circuit Extraction From Noisy Frequency Responses," *IEEE Trans. Electromagn. Compat.*, vol. 48, no. 1, pp. 104–120, 2006.

"Everything stinks till it's finished."

DR. SEUSS

"A ship in port is safe, but it is not what ships are for.
Sail out to sea and do new things."

Grace Hopper